EPR Spectroscopy of Antiferromagnetically-Coupled Cr^{3+} Molecular Wheels

A thesis submitted to the University of Manchester for the degree of Doctor of Philosophy in the Faculty of Engineering and Physical Sciences

2011

Rebecca J. Docherty

School of Chemistry

Table of Contents

Final word count: 28,048

Compound List and Abbreviations

Due to the very long formulae of the compounds presented in this thesis, they have been abbreviated to the following numbers.

1. $[Cr_8F_8(O_2C^tBu)_{16}]$

2. $[H_2NMe_2][Cr_7NiF_8(O_2C^tBu)_{16}]$

3. $[H_2NMe_2][Cr_7MnF_8(O_2C^tBu)_{16}]$

4. $[H_2NMe_2][Cr_7ZnF_8(O_2C^tBu)_{16}]$

5. $[^tBuCONHC_6H_{12}NH_2C_6H_{12}NHCO^tBu][Cr_7NiF_8(O_2C^tBu)_{16}]$

6. $[^tBuCONHC_6H_{12}NH_2C_6H_{12}NHCO^tBu][Cr_7MnF_8(O_2C^tBu)_{16}]$

7. $[^tBuCONHC_6H_{12}NH_2C_6H_{12}NHCO^tBu][Cr_7ZnF_8(O_2C^tBu)_{16}]$

8. $[Cs \subset Cr_7NiF_8(O_2C^tBu)_{16}] \cdot 0.5MeCN$

9. $[Cs \subset Cr_7MnF_8(O_2C^tBu)_{16}] \cdot 0.5MeCN$

10. $[Cs \subset Cr_7ZnF_8(O_2C^tBu)_{16}] \cdot 0.5MeCN$

11. $[Cr_7NiF_3(Etglu)(O_2C^tBu)_{15}(phpy)]$

12. $[Cr_7MnF_3(Etglu)(O_2C^tBu)_{15}(phpy)]$

13. $[Cr_7ZnF_3(Etglu)(O_2C^tBu)_{15}(phpy)]$

14. $Cr_7NiF_3(Etglu)(O_2C^tBu)_{15}(H_2O)]$

15. $[\{Cr_7NiF_3(Etglu)(O_2C^tBu)_{15}\}_2(4,4'\text{-bpy})]$

16. $[\{Cr_7NiF_3(Etglu)(O_2C^tBu)_{15}\}_2(pyN=Npy)]$

17. $[\{Cr_7NiF_3(Etglu)(O_2C^tBu)_{15}\}_2](pyCCpy)]$

18. $[\{Cr_7NiF_3(Etglu)(O_2C^tBu)_{15}\}_2](pyCHCHpy)]$

19. $[\{Cr_7NiF_3(Etglu)(O_2C^tBu)_{15}\}_2(pyCH_2CH_2py)]$

20. $[\{Cr_7NiF_3(Etglu)(O_2C^tBu)_{15}\}_2(pyCH(OH)CH(OH)py)]$

21. $[Cr_8F_4(Etglu)(O_2C^tBu)_{15}]$

22. $[Et_2NH_2]_3[Cr_6F_{11}(O_2C^tBu)_{10}]_2$

23. $[Et_2NH_2][Cr_6F_7(O_2C^tBu)_{10}(acac)_2]$

24. $[Et_2NH_2][Cr_6F_7(O_2C^tBu)_{10}(hfa)_2]$

25. $[Et_2NH_2]_3[Cr_6F_{11}(O_2C^tBu)_{10}]\cdot\{C_6H_4\text{-}1,4\text{-}(OH)_2\}_2$

List of Figures

8

10

List of Tables

Abbreviations Used

Acac   Acetylacetone

BVS   Bond Valence Sum

CIF   Crystal Information File

DCM   Dichloromethane

EPR   Electron Paramagnetic Resonance

e.s.d.   Estimated standard deviation (of bond lengths)

Et   Ethyl group [C_2H_5]

Et_2O diethyl ether

Hfa   Hexafluoroacetylacetone

INS   Inelastic Neutron Scattering

IR   Infra-red

Me   Methyl group [CH_3]

MeCN   Acetonitrile

Ph   Phenyl group [C_6H_5]

py   pyridine

RT   Room temperature

SMM   Single Molecule Magnet

SOC   Spin-Orbit Coupling

SQUID	Superconducting Quantum Interference Device
T	Tesla or Temperature
Tof-INS	Time of Flight Inelastic Neutron Scattering
^{t}Bu	Tertiary-butyl
THF	Tetrahydrofuran [C_4H_8O]
USSR	Union of Soviet Socialist Republics
VT	Variable temperature
ZFS	Zero-Field Splitting

Symbols and Constants Used

C   Curie constant

D Axial zero field splitting parameter

E Rhombic zero field splitting parameter

E   Energy

$E^{(0)}$ Zero-field energy

$E^{(1)}$ First-order Zeeman coefficient

$E^{(2)}$ Second-order Zeeman coefficient

g   g-factor or g-value

g_e g-factor for a free electron (= 2.0023)

H   Magnetic field strength

i   Current

k   Boltzmann constant (=1.38044×10^{-16} erg mol^{-1} K^{-1})

M   Molar magnetization

N_A Avogadro constant (= 6.0249×10^{23} mol^{-1})

S   Total spin

T   Temperature (in Kelvin)

z   Charge

χ Molar magnetic susceptibility

μ_B Bohr magneton (= 0.92731×10^{-20} erg gauss^{-1})

θ Weiss constant

Abstract

*A thesis submitted to The **University of Manchester** by **Rebecca J. Docherty** for the degree of **Doctor of Philosophy** on 31st **May 2011***

EPR Spectroscopy of Antiferromagnetically-Coupled Cr^{3+} Molecular Wheels

Currently, there is interest in the development of molecular-scale devices for uses in quantum information processing (QIP). With this application in mind, physical studies on antiferromagnetically coupled molecular wheels [Cr$_7$MF$_3$(Etglu)(O$_2$C^{t}Bu)$_{15}$(phpy)], where M is a divalent metal cation (M = Mn^{2+}, Zn^{2+}, Ni^{2+}) have been pursued. The heterometallic wheels contain an octagon of metal centres, which are bridged by fluoride ions, pivalate groups and a chiral N-ethyl-D-glutamine molecule which is penta-deprotonated and bound to the metal sites through all available O-donors. They are deep purple in colour and they have been named purple-Cr$_7$M. There is antiferromagnetic coupling between adjacent metal centres, J ≈ -8 cm^{-1}, resulting in a non-zero net spin ground state. The spin-Hamiltonian parameters of this family have been determined.

At the heterometal site of purple-Cr$_7$M wheels there is a terminal ligand which can be substituted for a variety of N-donor organic ligands. A series of bidentate N-donor linkers has been used to link Cr$_7$Ni wheels (each wheel S_{eff} = $^1/_2$) to create prototype two-qubit systems. Multi-frequency EPR spectroscopy and SQUID magnetometry has been used to extract the spin-Hamiltonian parameters of this family. It has been shown that the single wheels can be linked together electronically as well as chemically. It has been found that for the unsaturated linkers, there is a weaker interaction between Cr$_7$Ni wheels when longer linkers are used. The strength of interaction is smaller for the saturated linkers than for the unsaturated linkers.

The formation of "green"-Cr$_7$M wheels is different, being templated around a cation. Two new types of wheels have been studied: [^{t}BuCONHC$_6$H$_{12}$NH$_2$C$_6$H$_{12}$NHCO^{t}Bu][Cr$_7$M^{2+}F$_8$(O$_2$C^{t}Bu)$_{16}$] and [Cs⊂Cr$_7$MF$_8$(O$_2$C^{t}Bu)$_{16}$]·0.5MeCN (where, M = Mn^{2+}, Zn^{2+}, Ni^{2+}), where the former is templated around a long dialkylammonium group and the latter around a caesium cation. The effect of the templating cation on spectroscopic properties has been determined.

Physical studies on a family of antiferromagnetically-coupled *homometallic* clusters have been pursued. They consist of cyclic arrays of homometallic Cr^{3+} ions in either a octametallic wheel or hexametallic horseshoes. The horseshoes have the general formula: [Cr$_x$F$_{x+5}$L$_{2x-2}$]$_n$$^{3-}$ (where L = carboxylate). Cr^{3+} centres are bridged by pivalate groups and fluorides, while Cr^{3+} centres at the ends of the chain have terminal fluorides completing their coordination sphere. These terminal fluoride groups are labile enough to be substituted, e.g. [EtNH$_2$][Cr$_6$F$_7$(O$_2$C^{t}Bu)$_{10}$(acac)$_2$] is the product of a substitution reaction with acetylacetone.

Declaration

No portion of the work submitted in this thesis has been submitted in support of an application for another degree or qualification of this or any other university or other institute of learning.

Copyright statement

i. The author of this thesis (including any appendices and/or schedules to this thesis) owns certain copyright or related rights in it (the "Copyright") and s/he has given The University of Manchester certain rights to use such Copyright, including for administrative purposes.

ii. Copies of this thesis, either in full or in extracts and whether in hard or electronic copy, may be made **only** in accordance with the Copyright, Designs and Patents Act 1988 (as amended) and regulations issued under it or, where appropriate, in accordance with licensing agreements which the University has from time to time. This page must form part of any such copies made.

iii. The ownership of certain Copyright, patents, designs, trade marks and other intellectual property (the "Intellectual Property") and any reproductions of copyright works in the thesis, for example graphs and tables ("Reproductions"), which may be described in this thesis, may not be owned by the author and may be owned by third parties. Such Intellectual Property and Reproductions cannot and must not be made available for use without the prior written permission of the owner(s) of the relevant Intellectual Property and/or Reproductions.

iv. Further information on the conditions under which disclosure, publication and commercialisation of this thesis, the Copyright and any Intellectual Property and/or Reproductions described in it may take place is available in the University IP Policy (see http://www.campus.manchester.ac.uk/medialibrary/policies/intellectual-property.pdf), in any relevant Thesis restriction declarations deposited in the University Library, The University Library's regulations (see http://www.manchester.ac.uk/library/aboutus/regulations) and in The University's policy on presentation of Theses

Acknowledgements

I would like to thank my supervisors Professors Richard. E. P. Winpenny and Eric. J. L. McInnes for their constant encouragement during this project.

Professor David Collison for many helpful discussions and for giving me lots of good ideas.

I would like to thank Dr Floriana Tuna for teaching about how to use the EPR instruments and the SQUID magnetometer and for giving me lots of guidance and support throughout my Ph.D.

Dr Grigore A. Timco and Mr. Thomas B. Faust for the synthetic parts of this work.

I would like to thank the Institute Laue-Langevin, Grenoble, France and in particular Dr Michael. L. Baker for his help with the INS in chapter V.

Dr Chris Muryn and Dr Robin Pritchard for teaching me about X-ray crystallography.

I would like to thank Mr Dan Sells, Dr Ruth Edge and Dr Joanna Wolowska for keeping the EPR instruments running, for teaching me about cryogens and for always making sure I have enough liquid Helium.

I would like to thank all of the Ph.D. students and postdoctoral workers in the Manchester Magnetism group past and present for making it an enjoyable place to work. In particular I would like to thank Angelika Boeer , Charlene Smith, Floriana Tuna, Faisal Ashraf, George Whitehead, Grigore Timco, Harapriya Rath, Ian Casson, Jon Hawcett, John Machin, Joseph Sharples, Laurent Lisnard, Luke Batchelor, Morten

I   Introduction

I.1   Introduction

There are two distinct classes of exchange coupled oligomers which in the past two decades have been intensively studied. The most thoroughly investigated of the two are single molecule magnets (SMMs). SMMs can be magnetised as single molecules at very low temperatures. The first SMM that was synthesised was a dodecametallic manganese compound of the formula: $[Mn_{12}O_{12}(CH_3COO)_{16}H_2O_4]\cdot4H_2O\cdot2CH_3COOH$, commonly referred to as Mn_{12}.[1]   It was first reported in 1980 and its magnetic properties were heavily analysed in the early 1990s.[2, 3] SMM such as Mn_{12} are characterised by having a large spin ground state (for Mn_{12}, S = 10) and a large negative zero field splitting (ZFS). The second class of molecules which has been the focus of this work are antiferromagnetically-coupled molecular wheels and chains.   In contrast to the SMMs, they have a characteristically low or zero ground spin state. They provide interesting examples to study the quantum theory of total spins generated by coupling together several individual spins. The whole family stems from an octametallic Cr^{3+} molecular wheel, $[Cr_8F_8(O_2CCMe_3)_{16}]$ (**1**), as seen in Figure I.1.[4]

Figure I.1: The structure of octametallic Cr^{3+} wheel $[Cr_8F_8(O_2CCMe_3)_{16}]$ (**1**). Cr^{3+} atoms: green; O atoms: red; Fluorine atoms: yellow; Carbon atoms: black. All H atoms have been omitted for clarity.

1 was first synthesised in 1985 in the former Soviet Union as part of a study into the uses of Cr^{3+} complexes in the catalysis of oxidation and polymerisation reactions.[5] It was only after its later publication in 1990[4] that there was interest in the magnetic properties of this compound. **1** has antiferromagnetic coupling between neighbouring Cr^{3+} centres ($S = {}^3/_2$), resulting in an $S = 0$ ground state.[6] A rich family of molecules developed around **1**, containing homo- and hetero-metallic wheels and chains.[7] They are characterized by having a cyclic motif and by containing Cr^{3+} atoms which are bridged by fluorides and carboxylates. Their formation is controlled by the use of templating molecules, typically an ammonium cation. They have potential applications

in quantum information processing (QIP),[8] this application will be discussed further in section IV.1. To investigate the physical properties of this family, typically a range of techniques have been used; magnetisation, inelastic neutron scattering (INS), electron paramagnetic resonance (EPR) spectroscopy and magnetic circular dichroism (MCD) spectroscopy. EPR spectroscopy has been the main technique used in this thesis.

I.1   Molecular Magnetism

A molecule's magnetic behaviour is a description of its response to an applied magnetic field. It arises from the intrinsic spin of electrons. The nature of the magnetic behaviour depends upon how electrons on adjacent atoms interact with one another.

An unpaired electron is attracted to an applied magnetic field, this is paramagnetism. This effect is temperature dependent and does not depend on the strength of the applied magnetic field. A pair of electrons in a single orbital, according to the Pauli Exclusion Principle, will be spin paired: one electron will be $m_s = -^1/_2$ and the other one will be $m_s = +^1/_2$. The spin paired electrons will be repelled by an applied magnetic field, this is diamagnetism. This effect is weaker than paramagnetism and is not usually temperature dependent and does not depend on the strength of the field.

In an applied magnetic field a single unpaired electron can align with or align against the field. An electron being aligned anti-parallel ($m_s = -^1/_2$) with the field is more energetically favourable; therefore there is an energy gap between the two states. The energy gap between the two states is known as the Zeeman splitting and is given by

Equation 1.1. If there is more than one electron present there will be 2*S*+1 spin levels, where *S* is the total spin of the system.

$$E = g\mu_B H(2S + 1)$$

An energy level diagram depicting the Zeeman splitting of a single electron in an applied magnetic field is shown in Figure I.2.

Figure I.2: An energy level diagram of a single electron in an applied magnetic field.

At RT the spins will be randomly orientated $(kT \gg g\mu_B H)$. At lower T the thermal energy is lower than the energy gap of the Zeeman splitting $(kT \ll g\mu_B H)$, most of the spins will be aligned anti-parallel with the magnetic field. High magnetic polarisation leads to the molecule having a magnetic field of its own and it is itself a magnet.

A sample in an applied homogenous magnetic field acquires a magnetisation (*M*), which is related to the applied magnetic field through *Equation* I.2.

$$M = {-\delta E}/{\delta H}$$

Magnetic susceptibility (χ) is defined as the effect which magnetic field strength has on the magnetisation (*Eqn* I.3).

$$\chi = {\delta M}/{\delta H}$$

The magnetic susceptibility is a sum of the diamagnetic and paramagnetic susceptibilities (*Eqn* I.4)

$$\chi = \chi_p + \chi_d$$

The Curie Law is defined as: molar magnetic susceptibility varies as *C*/*T* as shown in *Equation* I.5. Where *C* is the Curie constant, the value of which depends upon the spin multiplicity of the spin ground state.

$$^1/_\chi = CT$$

The Curie Law assumes that a there is a large separation between the ground spin state and the excited state(s) and that the ground state has no first order angular momentum. The magnetic susceptibility is determined by the thermal population of the m_S levels. Magnetic susceptibility can be calculated with *Equation* I.6.[9]

$$\chi T = \frac{g^2 n.S(S+1)}{8}$$

Where, *S* is spin on individual centres or spin states, *n* is the number of spin centres present and g is the g-value. If two types of spin centre are present which are referred to as a and b, *Equation* I.6 can be adjusted as:

$$\chi T = \frac{n_a g_a^2 . S_a (S_a + 1)}{(n_a + n_b) 8} + \frac{n_b g_b^2 . S_b (S_b + 1)}{(n_a + n_b) 8}$$

<div align="right">*Equation* I.7</div>

In 1932 Van Vleck proposed a very important formula in molecular magnetism (*Eqn* I.8).[10]

$$\chi = \frac{N \sum_n \left(E_n^{(1)2} / kT - 2 E_n^{(2)} \right) exp \left(-E_n^{(0)} / kT \right)}{\sum_n \exp \left(-E_n^{(0)} / kT \right)}$$

<div align="right">*Equation* I.8</div>

The energy levels of a system in a magnetic field can be expanded in a power series (*Eqn* I.9).[11]

$$E_n = E_n^{(0)} + E_n^{(1)} H + E_n^{(2)} H^2 + \cdots$$

<div align="right">*Equation* I.9</div>

Where,

$E_n^{(0)}$ = energy of level n in zero field.

$E_n^{(1)}$ = 1st order Zeeman Coefficent (which splits the energy level into equally spaced components which are separated by $g\beta H$).

$E_n^{(2)}$ = 2nd order Zeeman Coefficent (which mixes the wavefunctions of the ground state with the excited state).

With Equation I.8 the magnetic susceptibility at temperature T can be calculated if $E_n^{(0)}$ is known. $E_n^{(1)}$ and $E_n^{(2)}$ can be calculated using perturbation theory.[9, 11, 12] . It is a particularly useful equation as only these quantities need to be known.

I.2   Magnetic Interactions

Transition metals often contain unpaired d electrons. Within a polymetallic transition metal cluster two such metal ions which are in close proximity can interact. If the spins of the two metal ions are aligned parallel to each other, the interaction is ferromagnetic. If the spins are aligned anti-parallel the interaction is antiferromagnetic.[9]

Exchange interactions between two paramagnetic centres may occur in two different ways. The first way is a direct interaction, when there is direct orbital overlap between the two metal centres. This is usually only possible for larger metal ions, the orbitals of 3d metals tend to be too small to interact in this way. The second way is *via* magnetic superexchange. This is when the magnetic coupling is mediated through a diamagnetic bridging ligand. There must be orbital overlap between the atomic orbitals of the bridging ligand and the metal centres. This can be via σ-bonding or π-bonding.[11] Magnetic superexchange is the most common type of exchange interaction in polynuclear clusters. The sign of *J* is simply a matter of convention. In this thesis, a positive *J*-value indicates that there is a ferromagnetic interaction and a negative *J*-value indicates antiferromagnetic interaction. An isotropic exchange Hamiltonian (*Eqn* I.10) can be constructed for two interacting spin centres (S_A and S_B)

$$\hat{H} = -2JS_A \cdot S_B$$

Equation I.10

I.3   Spin-Orbit Coupling

An electron has spin angular momentum and orbital angular momentum. The interaction of these effects is known as spin-orbit coupling (SOC). Through SOC excited states can mix with orbitally non-degenerate ground state.[13] This can cause g-values to deviate from that of a free electron (g_e = 2.0023) and for g-anisotropy to be present. This effect is less important for organic radicals; this is reflected in the fact they tend to have *quasi*-isotropic g-values which are close to g_e. SOC is more important for transition metals; they often have anisotropic sets of g-values that can deviate significantly from g_e. SOC can also lead to zero field splitting (see section I.4), therefore having significant effect on the spectroscopic properties of a transition metal cluster.[12]

I.4   Zero Field Splitting

When the spin ground state is $S \geq {}^1/_2$, there may be coupling to excited states through spin orbital coupling (SOC). This has the effect of removing the degeneracy of the m_s levels in zero field, this is called zero field splitting (ZFS). The D terms in Equation I.11 describe this interaction.[11]

$$D_{xx} + D_{yy} + D_{zz} = 0$$

Equation I.11

It has three principal values: D_x, D_y and D_z and is a traceless tensor.[14] Only two independent parameters are required.[14] An axial term (D),

$$D = D_{zz} - (D_{xx} + D_{yy})/2$$

Equation I.12

And a Rhombic term (*E*),

$$E = (D_{xx} - D_{yy})/2$$

For a molecule with axial symmetry D will be required and for one with rhombic symmetry D and E will be needed to describe the splitting of the m_s states.

The rhombicity of the system can be defined by

$$\lambda = |E/D|$$

With $\lambda = 0$ (axial) up to $^1/_3$, which is the rhombic limit.[15]

I.5   The g-value

When an external magnetic field (H_{ext}) is applied to a molecule which contains an unpaired electron, it is not necessarily the only magnetic field that the unpaired electron is experiencing. In addition to the applied magnetic field there may be local magnetic fields H_{local} which add vectorially to the external field to produce the total effective H_{eff} at the electron of interest (*Eqn* I.15).[15]

$$H_{eff} = (g/g_e)H$$

Where g_e is the g factor of a free electron and g is the effective g factor; g_e has a value of 2.0023; for transition metal complexes, g can deviate significantly from g_e. If g is isotropic than $g_x = g_y = g_z$. If there is axial g-anisotropy than $g_x = g_y \neq g_z$. If there is rhombic g-anisotropy than $g_x \neq g_y \neq g_z$. There is the following relationship between a g-value and SOC (*Eqn* I.16).[15] Where λ is the spin orbital coupling constant, ΔE is the

energy separation associated with the transition and c is a quantum mechanical coefficient which is dependent on the orbitals which are involved in the ΔE term.

$$g = 2.0023 - \frac{c\lambda}{\Delta E}$$

Hence the g-values of Cr^{3+} complexes are usually lower than g_e as λ is small and positive for Cr^{3+}.[16]

I.6   Hyperfine Splitting

If nuclear spins ($I \neq 0$) are present in the sample, then an unpaired electron can couple with I. The resonance will be split into $2I+1$ lines, which are designated as hyperfine splitting. This gives fine structure to a spectrum. If the electron is able to couple to several sets of nuclei, the overall pattern consists of the superposition of spectra due to different species present.[14]

I.7   Why Cr^{3+}

When the study of paramagnetic cluster compounds began in the 80's and 90's, the initial studies in this field were largely the result of the work of a few dominant groups: Lippard's Fe^{3+} clusters,[17] Christou's manganese clusters[18] and Gatteschi's clusters (which contain a variety of different metal centres).[19-21] These groups reported on all the common paramagnetic 3d metal ions, with the exception of chromium ($S = {}^3/_2$). The electronic structure in a octahedral crystal field is shown in Figure I.3.[13]

Figure I.3: The electronic structure of the d orbitals of octahedral Cr^{3+}.

The absence of chromium examples is likely to be due to the considerable ligand-field stabilization energy that is associated with Cr^{3+} complexes. It is this stability which makes the synthesis of Cr^{3+} complexes difficult. Whilst the stability of these complexes is a challenge, it also follows that the clusters formed will be particularly chemically inert: an essential quality for the utilization of these compounds in quantum information processing (see section IV.1). It wasn't until the publication of **1** in 1991 that Cr^{3+} began to be used in spin cluster complexes. A Cr^{3+} backbone favours the formation of these cyclic clusters, as Cr^{3+} is a stable oxidation state and forms predictable *pseudo*-octahedral geometries, which is a requirement for the wheel motif.

I.8   Templating molecules

The synthesis of this family of magnetic materials is not purely serendipitous. A cation (typically a secondary alkylammonium cation) is found at the centre of these clusters. The templating cation mediates the formation of the polynuclear cluster through H-bonding interactions. The size[22] and form[23] of the structure can be selected by choosing an appropriate templating molecule. It has been previously reported that in the system of (Cr_nNi) wheels, the size of the ring can be controlled by the choice of secondary ammonium templating cations. When secondary ammonium cations with branched alkyl chains were used, nonanuclear wheels such as [Iso_2NH_2][Cr_8Ni

$F_9(O_2C^tBu)_{18}$] were formed. When a linear alkyl chain is used as a templating molecule an octametallic wheel such as [$(C_3H_7)_2NH_2$][$Cr_7CoF_8(OOCMe_3)_{16}$] will be formed.[24]

I.9   Heterometallic "Green" Cr₇M Wheels

I.9.1   A Structure Description of Heterometallic green-Cr₇M Wheels

The family of isostructural heterometallic wheels [H_2NMe_2][$Cr_7MF_8(O_2C^tBu)_{16}$], where M^{2+} = Ni (**2**), Mn (**3**), Zn (**4**), Co, Cd, and Fe have been extensively studied since being first reported in 2003.[25-29]. These compounds are green and shall be named green-Cr₇M for simplicity. Seven Cr^{3+} and one M^{2+} centre form a near perfect, planar octagon, Figure I.4.

Figure I.4: Side and top views of [H_2NMe_2][$Cr_7MF_8(O_2C^tBu)_{16}$], M atom: dark green; All other colours as before.

Between each metal centre there is a single bridging fluoride ion, and two pivalate groups. Eight of the pivalate groups take an equatorial position in the plane of the wheel between each metal ion. The other bridging pivalates take axial positions and are located alternately on either side of the plane of the wheel. There is a dimethylammonium templating cation at the centre of the wheel.

I.9.2   The Effective Spin State of a green-Cr_7M Wheel

The choice of heterometal ion in a green-Cr_7M wheel can be used to tune the magnetic and electronic properties of the wheel, whilst retaining an isostructural geometry. The carboxylate functionality provides delocalised π-electrons and hence a pathway for magnetic superexchange around the circle of metal ions. There is antiferromagnetic coupling between adjacent metal centres, $J \approx$ -6 cm^{-1}, resulting in a non-zero net spin ground state. This has been determined through magnetic measurements[30] Figure I.5 is the coupling scheme for a Cr_7M wheel. The red arrow is the heterometal. For Ni^{2+} S = 1, Mn^{2+} $S = {}^5/_2$ and for Zn^{2+} S = 0. The light and dark green arrows are Cr^{3+} atoms. For a Cr_7Ni wheel the ground spin state will be: $S = 4 \times {}^3/_2 - (3 \times {}^3/_2 + 1) = {}^1/_2$. For a Cr_7Mn wheel: $S = 4 \times {}^3/_2 - (3 \times {}^3/_2 + {}^5/_2) = 1$. For a Cr_7Zn wheel: $S = 4 \times {}^3/_2 - (3 \times {}^3/_2 + 0) = {}^3/_2$. The total spin of the excited state increases in integer steps from the ground state, i.e. for Cr_7Mn the first excited state S = 2.

Figure I.5: Vector coupling scheme of a Cr_7M wheel

I.9.3   The EPR Spectroscopy of green-Cr_7M Wheels

An EPR spectroscopy study has been conducted on **2**, **3** and **4**. The spin-Hamiltonian parameters provided in *Tables* I.1 and I.2 have been fitted to EPR measurements performed on single crystal and polycrystalline samples using the strong exchange limit (SEL).[30]

Table I.1: Spin-Hamiltonian parameters of the ground states of compounds **2**, **3** and **4**.

	2	**3**	**4**
Ground Spin State	$S = {}^1/_2$	$S = 1$	$S = {}^3/_2$
D (cm^{-1})	N/A	0.800	-0.41
E (cm^{-1})	N/A	-0.085	-0.041
g-value	$g_{xy} = 1.78$ $g_z = 1.74$	$g_{iso} = 2.00$	$g_{xy} = 1.955$ $g_z = 1.945$

Table I.2: The spin-Hamiltonian parameters of the first excited states of compounds **2**, **3** and **4**.

	2	**3**	**4**
Excited Spin State	$S = \frac{3}{2}$	$S = 2$	$S = \frac{5}{2}$
D (cm^{-1})	0.56	0.185	0.04
E (cm^{-1})	Not determined	Not determined	Not determined
B^4_0 (cm^{-1})	Not determined	-7.5×10^{-4}	8×10^{-5}
g-value	$g_{xy} = 2.00$	$g_{xy} = 2.000$	$g_{xy} = 1.955$
	$g_z = 2.05$	$g_z = 1.980$	$g_z = 1.945$

These spin-Hamiltonian parameters will be compared those determined for the new heterometallic wheels provided in this thesis.

I.10 Measurement Techniques Used

A brief introduction to the principal concepts of the measurement techniques used in this Ph.D. thesis is provided in this section.

I.10.1 EPR Spectroscopy

EPR spectroscopy is a spectroscopic technique which was first discovered during World War II by Soviet physicist Zavoisky.[31] EPR spectroscopy is a very useful tool in the investigation of the lowest lying energy levels of transition metal clusters. EPR is the primary technique used to analyse the compounds presented in this thesis. EPR utilizes microwaves ranging in frequency from 1 GHz to 254 GHz[28] along with magnetic

fields to study species with one or more unpaired electrons. A fairly wide range of substances can be investigated in this manner including organic radicals and many transition metal compounds. [15]

I.10.1.1 The Experimental Set-up

Figure I.6 is a block diagram of a perpendicular mode continuous wave (cw)-EPR spectrometer which has been adapted from reference.[15]

Figure I.6: A block diagram of a cw-EPR spectrometer adapted from reference[15].

The sample is mounted inside the spectrometer perpendicular to the applied magnetic field. The applied magnetic field is generated by an electromagnet and is swept during the experiment. In addition to this applied magnetic field, there is a smaller oscillating magnetic field which is applied continuously throughout the experiment to the sample *via* Zeeman modulation coils. The signal response from the cavity is modulated at the Zeeman modulation frequency. The direction of the perturbation frequency is perpendicular to the electromagnet's magnetic field. The microwave bridge supplies microwaves which are transmitted to the sample *via* the waveguide. *Table* I.3 shows the nominal microwave frequencies and the bands which have been used for experiments reported in this Ph.D. thesis.

Table I.3: Approximate Microwave Frequencies and Bands

Band	ν (GHz)
S	3.5
X	9.25
K	20.0
Q	35.0
W	95.0

I.10.1.2 What can happen to an unpaired electron in a cw-EPR experiment

The simplest case we can have in EPR is a single unpaired electron with an $S = \frac{1}{2}$ spin state. The applied magnetic field has the effect of lifting the degeneracy of the $m_s = \pm \frac{1}{2}$ due to the Zeeman effect. Once the Zeeman splitting matches the microwave energy, due to the Maxwell-Boltzmann distribution there are typically more electrons in the lower state, there is a net absorption. The first derivative of the absorption spectrum is recorded.

Figure I.7: An energy level splitting diagram depicting the splitting of m_s states and the spectrum that is recorded during a cw-EPR experiment. Where H is the applied magnetic field, and g value is a proportionality factor, equivalent to NMR's chemical shift, which will be discussed in section I.5.

Selection rules can be derived from transition probabilities. For perpendicular mode cw-EPR they are: $\Delta S = 0$, $\Delta m_S = \pm 1$.

I.10.1.3 A Spin Triplet

The energy level diagram for a spin triplet ($S = 1$) is shown below (Figure I.8)

Figure I.8: An energy level diagram of a spin triplet

The m_s states are split by D, and the transitions in the EPR experiment are split by a function of D and centred on a certain g-value. This gives the EPR spectrum fine structure. The EPR spectrum shown in Figure I.8 is for a single orientation. In a powder EPR spectrum, for each orientation there will be a pair of peaks.

I.10.1.4 Strong Exchange Limit

A widely used approach in the interpretation of EPR and magnetic data of exchange coupled systems is the strong exchange limit (SEL). This method assumes $J >> D$, thus D is treated as a small perturbation on the total effective spin state. The EPR spectra

are treated as superpositions of the different total effective spin states which are thermally populated at the temperature at which the measurement is performed.[33] Each spin state is modelled independently and then added together. This has been the main technique used to model EPR data in this thesis.

Equation I.17 is a SEL spin-Hamiltonian.

$$\hat{H}_{eff} = \hat{S}_{eff} D_{eff} \hat{S}_{eff} + \mu_B \vec{B} g_{eff} \hat{S}_{eff}$$

Equation I.17

Where D_{eff} is the axial zero field splitting parameter of the total effective spin state and g_{eff} corresponds to the g-value of the total effective spin state.

I.10.2 Magnetic Measurements

The magnetisation and the magnetic susceptibility data presented in this thesis have been recorded using a Superconducting Quantum Interference Device (SQUID). A SQUID magnetometer has a superconducting magnet which provides a longitudinal uniform magnetic field (up to ~7 T). The superconducting magnet magnetizes the sample. A superconducting detection coil is coupled inductively to the sample and is located in the uniform region of the magnetic field. The sample is moved through the superconducting detection coil and the magnetic moment of the sample induces a current in the coil. The SQUID device converts the current to voltage, a change in magnetic flux in the superconducting detection coil causes a variation in the SQUID output voltage. The change in voltage is proportional to the magnetic moment of the sample. The magnetic moment can be detected as a function of temperature or magnetic field. There are other variables possible.[12] The experimental details of the SQUID measurements presented in this Ph.D. thesis are in section VI.3.

I.10.3 Inelastic Neutron Scattering

During an inelastic neutron scattering (INS) experiment, a monochromatic neutron beam is directed at a polycrystalline sample. When the neutron beam hits the sample three things can happen. (i) The neutron beam can be scattered by the nuclei. (ii). The neutron beam can be absorbed by the nuclei. (iii). The neutron beam can be scattered through magnetic interactions between the intrinsic magnetic moment of the neutrons and the magnetic field generated by the unpaired electrons in the sample. The third case provides information about the electronic structure of the molecule being investigated.[34-38] The INS presented in chapter V was recorded using a time-of-flight neutron scattering spectrometer using non deuterated polycrystalline samples.[39] Figure I.9 below is reproduced from reference[34] and depicts a time-of-flight neutron scattering spectrometer.

Figure I.9: A schematic representation of a time-of-flight inelastic scattering spectrometer, reproduced from reference[34].

The polychromatic neutron beam is generated in a neutron reactor and passes through a monochromator which are a series of choppers. The choppers select the energy and the wavelength of the neutrons, producing a monochromatic beam with a precise initial energy (E_i) and wave-vector (k_i). The monochromatic beam is directed through the sample and is scattered. The scattered neutrons are collected in an array of time-resolved detectors. The time of arrival of the neutrons is recorded, from which the final neutron energy (E_f) is calculated. E_f experience energy loss or energy gain from transitions in the sample. The final wave-vector (k_i) is deduced from the scattering angle 2θ. Q is the scattering vector ($Q = k_i - k_f$). The Q-dependence of a transition is used to obtain information about its magnetic properties. The selection rules for INS are: $\Delta S = 0, \pm 1$ and $\Delta M_S = 0, \pm 1$.

The INS in this Ph.D. thesis was measured at zero applied magnetic field. This is in contrast to EPR spectroscopy which must be measured with an applied magnetic field. This makes INS a very useful technique for determining ZFS directly.

I.11 Project Aims

The first aim of this Ph.D. thesis is to determine the effect of templating cation on the spectroscopic properties on a Cr_7M wheel; this shall be discussed in Chapter II. The second aim is to determine the spin-Hamiltonian parameters of a family of purple-Cr_7M molecular wheels. This is discussed in Chapter III. The purpose of the first two aims is to characterize the electronic structure of single Cr_7M wheels, this is important as the single wheels can be linked into larger supramolecular structures for applications in quantum information processing (QIP). A detailed understanding of the electronic structure of the single wheels is required to understand the properties of the larger supramolecular structures. Thirdly, a series of organic linkers have been used to link purple-Cr_7Ni wheels into dimers, EPR spectroscopy has been used to determine the interaction between the two wheels. The purple-Cr_7Ni dimers are prototype two-qubits systems, which have potential applications in QIP. The structure-property relationship of the organic linkers has been determined. This is discussed in Chapter IV. The fourth aim is to determine the effect of capping ligand on the exchange coupling of a family of hexanuclear horseshoes. This chapter aims for a better understanding how electronic structure is affected by choice of capping ligand and to establish structure-property relationships. This shall be discussed in Chapter V.

I.12 References

1.   T. Lis, *Acta Cryst. Section B*, 1980, **36**, 2042-2046.

2.   C. Paulsen, J. G. Park, B. Barbara, R. Sessoli and A. Caneschi, *J. Magn. Magn. Mater.*, 1995, **140-144**, 1891-1892.

3.   R. Sessoli, D. Gatteschi, A. Caneschi and M. A. Novak, *Nature*, 1993, **365**, 141-143.

4.   N. V. Gerbeleu, Y. T. Struchkov, G. A. Timko, A. S. Batsanov, K. M. Indrichan and G. A. Popovich, *Doklady Akademii Nauk SSSR*, 1990, **313**, 1459-1462.

5.   Pat. Su. 1299116, 1985.

6.   J. van Slageren, R. Sessoli, D. Gatteschi, A. A. Smith, M. Helliwell, R. E. P. Winpenny, A. Cornia, A.-L. Barra, A. G. M. Jansen, E. Rentschler and G. A. Timco, *Chem. Eur. J.* 2002, **8**, 277-285.

7.   E. J. L. McInnes, S. Piligkos, G. A. Timco and R. E. P. Winpenny, *Coord. Chem. Rev.*, 2005, **249**, 2577-2590.

8.   M. Affronte, F. Troiani, A. Ghirri, A. Candini, M. Evangelisti, S. Carretta, P. Santini, G. Amoretti, S. Piligkos, G. Timco and R. E. P. Winpenny, *Polyhedron*, 2005, **24**, 2562-2567.

9.   D. Gatteschi, R. Sessoli, J. Villain Molecular Nanomagnets, Oxford University Press, Oxford, 2006.

10.   J. H. Van Vleck, *The Theory of Electric and Magnetic Susceptibilities*, Oxford University Press, Oxford, 1932.

11.   R. Boca, Theoretical foundations of molecular magnetism, Elsevier, Amsterdam, Oxford, 1999.

12.   O. Kahn, *Molecular Magnetism*, VCH, New York, Weinheim, Cambridge, 1993.

13.   C. E. Housecroft and A. G. Sharpe, *Inorganic Chemistry*, Pearson Education Limited, Harlow, Essex, 2001.

14.   J. A. Weil, J. R. Bolton and W. J. E., *Electron Paramagnetic Resonance: Elementary Theory and Practical Applications*, John Wiley & Sons, Inc, New York, 1994.

15.   F. E. Mabbs and D. Collison, *Electron Paramagnetic Resonance of d Transition Metal Compounds*, Elsevier, Amsterdam, 1992.

16.   T. M. Dunn, *Trans. Faraday Soc.*, 1961, **57**, 1441-1444.

17.   S. M. Gorun and S. J. Lippard, *Inorg. Chem.*, 1988, **27**, 149-156.

18.   R. Sessoli, H. L. Tsai, A. R. Schake, S. Wang, J. B. Vincent, K. Folting, D. Gatteschi, G. Christou and D. N. Hendrickson, *J. Am. Chem. Soc.*, 1993, **115**, 1804-1816.

19.   R. Sessoli, D. Gatteschi, A. Caneschi and M. A. Novak, *Nature (London)*, 1993, **365**, 141-143.

20.   C. Benelli and D. Gatteschi, *Chem. Rev. (Washington, DC, U. S.)*, 2002, **102**, 2369-2387.

21.   C. Sangregorio, T. Ohm, C. Paulsen, R. Sessoli and D. Gatteschi, *Phys. Rev. Lett.*, 1997, **78**, 4645-4648.

22.   S. L. Heath, R. H. Laye, C. A. Muryn, N. Lima, R. Sessoli, R. Shaw, S. J. Teat, G. A. Timco and R. E. P. Winpenny, *Angew. Chem. Int. Ed.*, 2004, **43**, 6132-6135.

23.   M. Rancan, G. N. Newton, C. A. Muryn, R. G. Pritchard, G. A. Timco, L. Cronin and R. E. P. Winpenny, *Chem. Commun.*, 2008, 1560-1562.

24.   F. K. Larsen, J. Overgaard, S. Parsons, E. Rentschler, A. A. Smith, G. A. Timco and R. E. P. Winpenny, *Angew. Chem. Int. Ed.*, 2003, **42**, 5978-5981.

25.   F. K. Larsen, E. J. L. McInnes, H. E. Mkami, J. Overgaard, S. Piligkos, G. Rajaraman, E. Rentschler, A. A. Smith, A. A. Smith, V. Boote, M. Jennings, G. Timco and R. E. P. Winpenny, *Angew. Chem. Int. Ed.*, 2003, **42**, 101.

26.   M. Affronte, I. Casson, M. Evangelisti, A. Candini, S. Carretta, C. Muryn, S. J. Teat, G. A. Timco, W. Wernsdorfer and R. E. P. Winpenny, *Angew. Chem. Int. Ed*, 2005, **44**, 6496.

27.   R. H. Laye, F. K. Larsen, J. Overgaard, C. A. Muryn, E. J. L. McInnes, E. Rentschler, V. Sanchez, S. J. Teat, H. U. Gudel, O. Waldmann, G. A. Timco and R. E. P. Winpenny, *Chem. Commun.*, 2005, 1125-1127.

28.   V. Corradini, R. Biagi, U. del Pennino, V. De Renzi, A. Gambardella, M. Affronte, C. A. Muryn, G. A. Timco and R. E. P. Winpenny, *Inorg. Chem.*, 2007, **46**, 4937-4943.

29.   S. Piligkos, H. Weihe, E. Bill, F. Neese, H. E. Mkami, G. M. Smith, D. Collison, G. Rajaraman, G. A. Timco, R. E. P. Winpenny, E. J. L. McInnes, *Chem. Eur.J.,* 2009, **15**, 3152.

30.   S. Piligkos, Ph.D. Thesis, The University of Manchester (Manchester, UK), 2004.

31.   Y. Zavoisky, *Physics-Uspekhi*, 1941, 977.

32.   G. A. Timco, S. Carretta, F. Troiani, F. Tuna, R. J. Pritchard, C. A. Muryn, E. J. L. McInnes, A. Ghirri, A. Candini, P. Santini, G. Amoretti, M. Affronte and R. E. P. Winpenny, *Nat Nano*, 2009, **4**, 173-178.

33.   A. Bencini and D. Gatteschi, *EPR of Exchanged Coupled System*, Springer-Verlag, Berlin, 1989.

34.   R. Basler, C. Boskovic, G. Chaboussant, H. U. Güdel, M. Murrie, S. T. Ochsenbein and A. Sieber, *ChemPhysChem*, 2003, **4**, 910-926.

35.   S. W. Lovesey, *Theory of neutron scattering from condensed matter Vol. 1*, Oxford, 1984.

36.   S. W. Lovesey, *Theory of neutron scattering from condensed matter: Vol.2*, Clarendon Press, Oxford, 1984.

37.   F. Hippert, E. Geissler, J. L. Hodeau, E. Lelievre-Berna and J. R. Regnard, *Neutron and X-ray spectroscopy*, Springer, Heidelberg, 2006.

38.   G. L. Squires, *Introduction to the theory of thermal neutron scattering*, Cambridge University Press, Cambridge, 1978.

39.   T. Unruh, J. Neuhaus and W. Petry, *Nucl. Instrum. Meth.*, 2007, **580**, 1414-1422.

II Physical Studies on a Family of Green-Cr$_7$M Wheels: Investigating the Influence of Templating Cation on Spectroscopic Properties

II.1 Introduction

As mentioned in chapter one the formation of Cr_7M wheels is templated around a mono cation. This chapter will discuss two new types of templating molecules; long chain alkylammonium cations and caesium cations. The first family of compounds consists of a series of isostructural heterometallic wheels, $[^tBuCONHC_6H_{12}NH_2C_6H_{12}NHCO^tBu][Cr_7MF_8(O_2C^tBu)_{16}]$, where M = Ni^{2+} (**5**), Mn^{2+} (**6**) and Zn^{2+} (**7**). The structure can be described as a rotaxane, as it consists of a long dialkylammonium cationic axle group which is threaded through a heterometallic macrocycle. There are numerous examples in the literature of the use of dialkylammonium groups acting as axle groups in the synthesis of rotaxanes; for example they have been used in cyclic peptides[1], crown ethers[2] and in cucurbituril which is a nonadecacyclic cage compound.[3] Dialkylammonium salts have been selected for these studies as the ammonium group has been found to effectively bind with the molecular ring torus through hydrogen bonding interactions.[4] The ends of the axle groups are typically bulky *tert*-butyl groups, or large aromatic groups. This functionality has the effect of stoppering the axle, thus preventing the two molecules from dissociating.

The second templating group is a caesium cation. The cavity at the centre of a polymetallic wheel can be utilized for host-guest chemistry, providing the cavity is of a reasonably large size. Several research groups have used this as a method to control the properties of polymetallic wheels. For example Saalfrank and co-workers in 1996 controlled the size of a polymetallic Fe wheel by choice of guest alkali metal. The size of the wheel is increased from 6-membered to 8-membered by increasing the size of the cation giving: $Na[Fe_6\{N(CH_2CH_2O)_3\}_6]$ and $Cs[Fe_8\{N(CH_2CH_2O)_3\}_8]$.[5] It has been

reported that the treatment of $[H_3N^nPr][Cr_7MF_8(O_2C^tBu)_{16}]$ with an excess of caesium pivalate followed by recrystallization from diethyl ether / acetonitrile, yields the caesium templated wheel $[Cs \subset Cr_7MF_8(O_2C^tBu)_{16}] \cdot 0.5MeCN$, where M^{2+} = Ni^{2+} (**8**), Mn^{2+} (**9**) and Zn^{2+} (**10**) . This compound can also be made directly from a direct reaction of pivalic acid, chromium(III) tetrahydrate, the appropriate metal carbonate and caesium pivalate. Further details of this synthesis can be found in the literature.[6]

An EPR study has been conducted on compounds **5** to **10**. With the aim of investigating the influence of the templating cation on the spectroscopic and magnetic properties of Cr_7M wheels. The strong exchange limit has been used to fit the experimental data (see section I.10). All the EPR data in this chapter has been modelled with the following spin-Hamiltonian:

$$H = \mu_B B g \hat{S} + D[\hat{S}_z^2 - S(S+1)/3]$$

Equation II.1

Where *S* is the total spin quantum number of the molecule.

II.2 Structural Description of the Rotaxane Wheels: Compounds 5, 6 and 7

Compounds **5** to **7** are isostructural (Figure II.1)
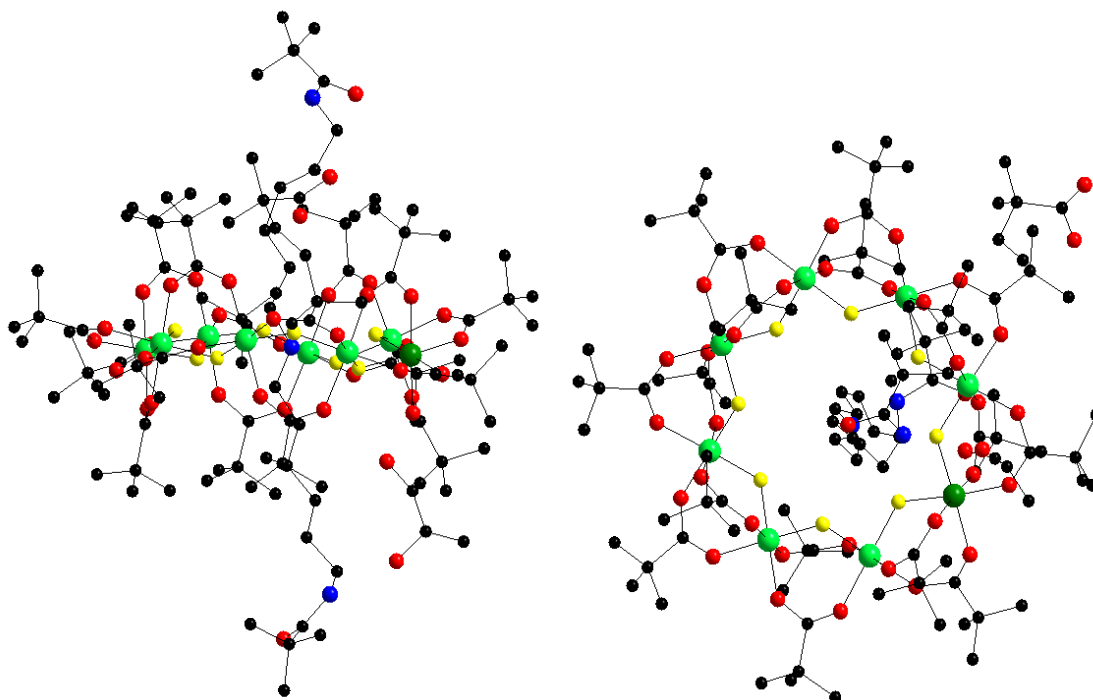
Figure II.1: Top and Side view of [^{t}BuCONHC$_6$H$_{12}$NH$_2$C$_6$H$_{12}$NHCO^{t}Bu][Cr$_7$M^{2+}F$_8$(O$_2$C^{t}Bu)$_{16}$], M^{2+} = Mn, Zn, Ni. Colours; Cr atoms: light green; M^{2+} atom: dark green; C atoms: black; F atoms: yellow; N atoms: blue; O atoms: red. All H atoms have been removed for clarity.

The molecular wheel is assembled around a long dialkylammonium cationic axle group, which is terminated at each end with a bulky tertiary butyl group (Figure II.2). There is a hydrogen bonding interaction between the ammonium group of the axle moiety and the bridging fluorides within the molecular wheel.
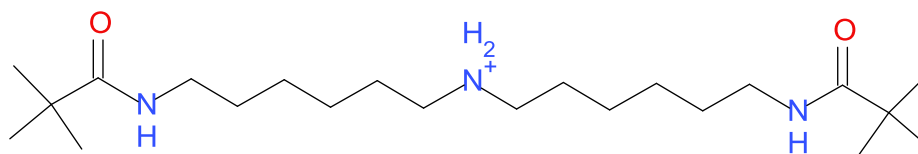
Figure II.2: The dialkylammonium templating molecule of compounds **5**, **6** and **7**.

The wheel formed is not a perfect octagon. A mean plane of the metal centres can be calculated and the mean deviation from the mean plane of the 8 metal centres (MDMP) has been determined with the MPLN command of the crystallographic program SHELX-97.[7] For compounds **8** to **10,** MDMP = 0.175 Å. This is close to the calculated MDMP value for dimethylammonium-templated Cr_7M wheels (**5** to **7**) which is 0.180 Å. Hence inclusion of the longer chain templates does not significantly distort the wheels.

II.3   Structural Description of Caesium Templated Wheels: Compounds 8, 9 and 10

The structure of $[Cs \subset Cr_7MF_8(O_2C^tBu)_{16}] \cdot 0.5MeCN$ can be seen in Figure II.3. Compounds **8**, **9** and **10** are isostructural. At the centre of the structure there is a caesium cation, which is bound to all eight bridging fluoride ions and takes a position which is co-planar to the eight metal centres of the wheel. The Cs···F bond distances range from 3.131 Å to 3.381 Å.
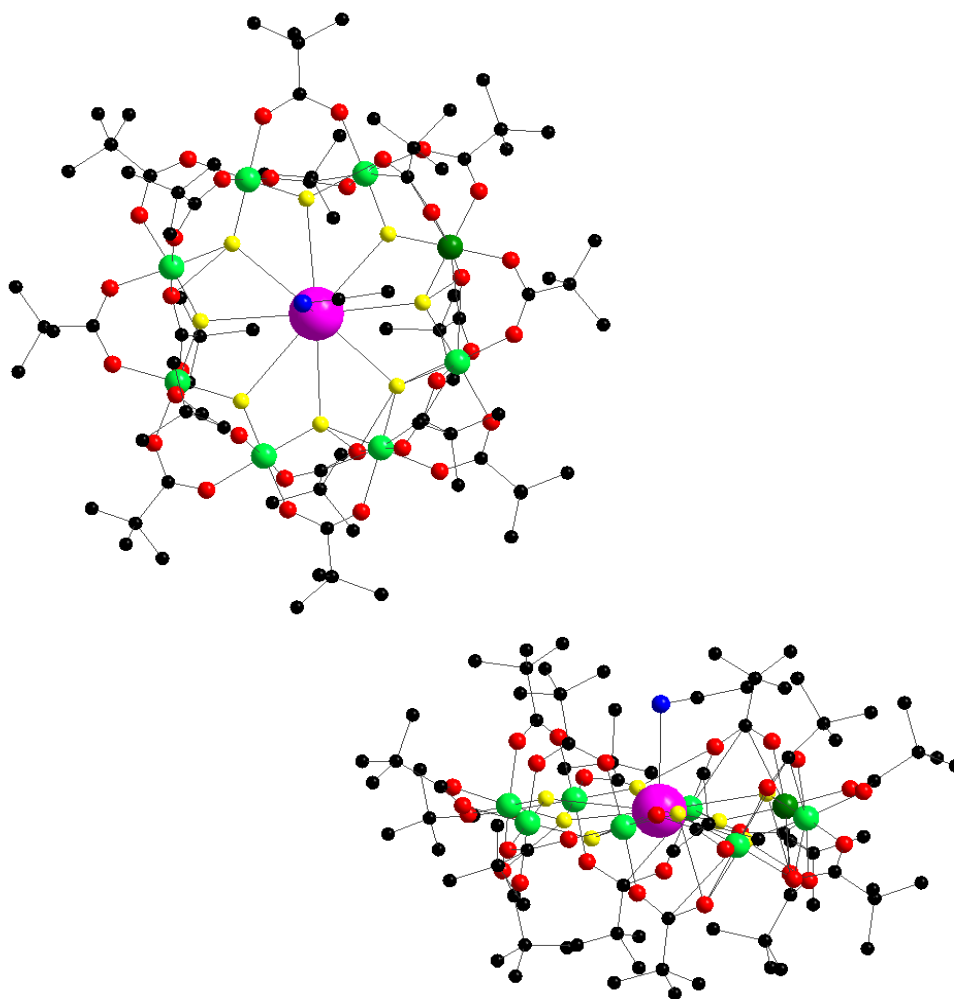
Figure II.3: Top and side view of the caesium centred wheel.
[Cs⊂Cr$_7$MF$_8$(O$_2$C^{t}Bu)$_{16}$]·0.5MeCN. Hydrogen atoms have been moved for clarity and the following colours have been used: light green: chromium atoms; dark green: heterometal; Pink: caesium atom; Yellow: fluoride atoms; Black: carbon atoms; Red; Oxygen atoms.

As with the dimethylammonium templated wheels there are equatorial and axial pivalate groups. However, on one side of the wheel the axial pivalate groups lean in towards the caesium cation and on the other side of the wheel they lean away from the caesium (see Figure II.4). This distortion allows for the inclusion of the partial occupancy of an acetonitrile molecule which is coordinated to the caesium cation. When a Cr$_7$M wheel is templated around an alkylammonium group the axial pivalate

groups have a geometry which is perpendicular to the plane of the metal centres. Figure II.4 is the molecular structure of a caesium templated wheel with the equatorial pivalate groups removed. This has been done so that the reader can clearly see the stereochemistry of the axial pivalate groups.
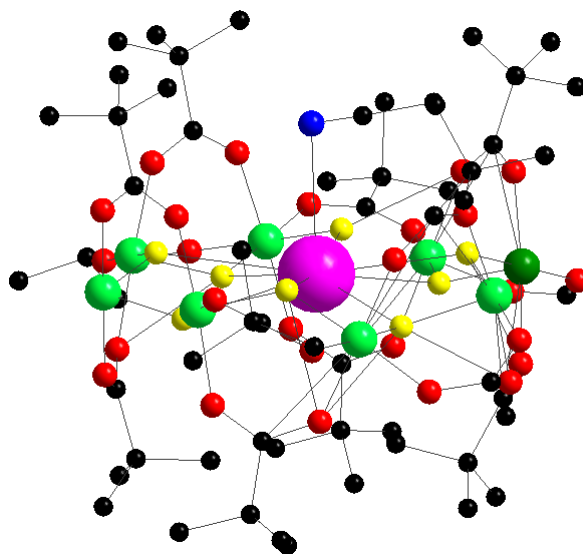
Figure II.4: The molecular structure of $[Cs \subset Cr_7NiF_8(O_2C^tBu)_{16}] \cdot 0.5MeCN$
in the crystal, with the equatorial pivalate groups removed for clarity.

In comparison to the dialkylammonium-templated wheels, the caesium-templated wheels have a more planar arrangement of metal centres. The MDMP of the eight metal centres is 0.148 Å.

II.4 Results

II.4.1 EPR study of [^{t}BuCONHC$_6$H$_{12}$NH$_2$C$_6$H$_{12}$NHCO^{t}Bu][Cr$_7$NiF$_8$(O$_2$C^{t}Bu)$_{16}$]

Variable temperature EPR spectra were measured at X- and Q-band frequencies (Figure II.5 and II.6). There is a single anisotropic resonance due to a $S = ½$ ground state. The coupling scheme (Figure I.5) which was used by Dr. S. Piligkos to model the EPR spectra of compounds **2** to **4** can be used for **5**. Hence, unsurprisingly replacement of dimethylammonium with a long chain template has not changed the coupling scheme.
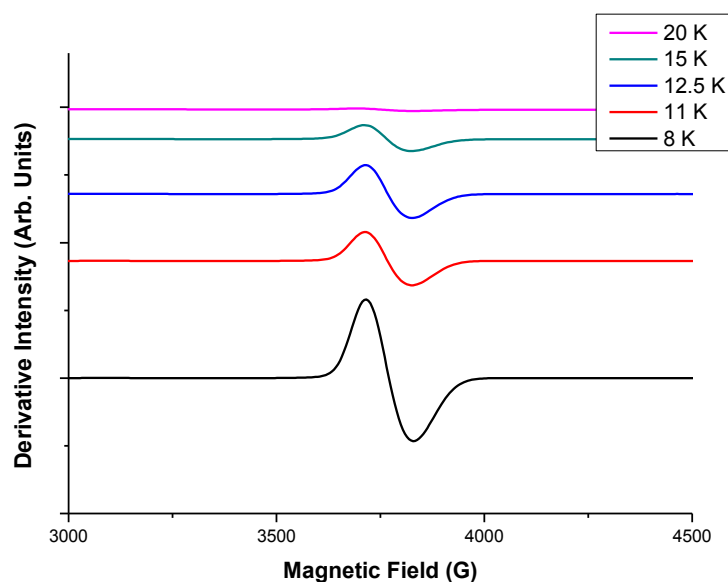
Figure II.5: Variable temperature EPR spectra of a powdered polycrystalline sample of [^{t}BuCONHC$_6$H$_{12}$NH$_2$C$_6$H$_{12}$NHCO^{t}Bu][Cr$_7$NiF$_8$(O$_2$C^{t}Bu)$_{16}$] (**5**) at X-band frequency.
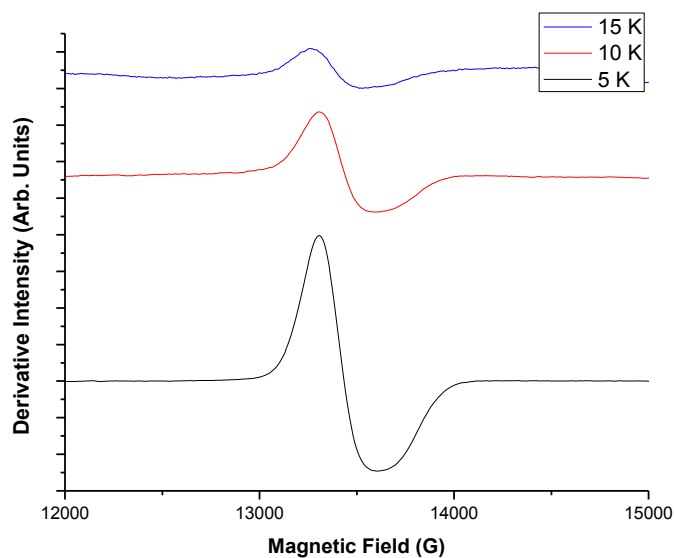
Figure II.6: Variable temperature EPR spectra of a powdered polycrystalline sample of [^{t}BuCONHC$_6$H$_{12}$NH$_2$C$_6$H$_{12}$NHCO^{t}Bu][Cr$_7$NiF$_8$(O$_2$C^{t}Bu)$_{16}$] (**5**) at Q-band frequency.

Figure II.7 compares the Q-band EPR spectra of compounds **2** and **5** at 5 K. In the EPR spectrum of **5** the axial nature of the g-values is resolved; there are two overlapping resonances at ~13,850 G (g = 1.78) and ~14,000 G (g = 1.74). This splitting is unresolved in **8**. The EPR spectrum of **5** can be modelled as $S = {}^1/_2$ with the following spin-Hamiltonian parameters: g_{xy} = 1.780, g_z = 1.740 and an isotropic Gaussian line width of 100 G.[8]
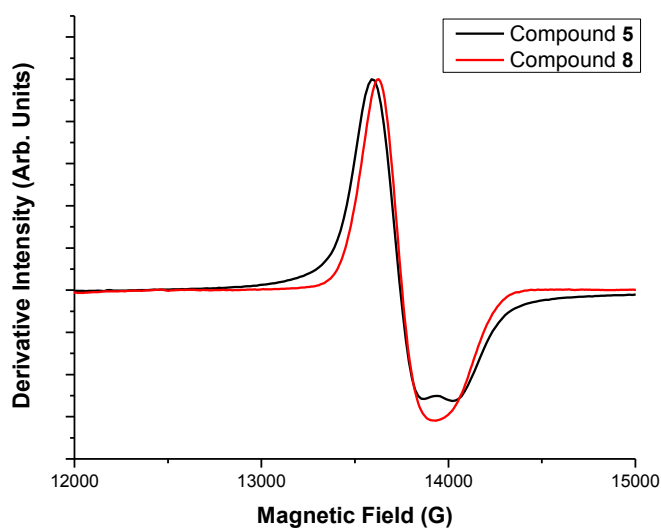
Figure II.7: Comparison of powder EPR spectra of $[H_2NMe_2][Cr_7NiF_8(O_2C^tBu)_{16}]$ (**2**) and $[^tBuCONHC_6H_{12}NH_2C_6H_{12}NHCO^tBu][Cr_7NiF_8(O_2C^tBu)_{16}]$ (**5**) at Q-band frequency.

Compound **8** can be modelled with slightly different spin-Hamiltonian parameters: g_{xy} = 1.780, g_z = 1.745 and isotropic line widths of 100 G (Figure II.8)
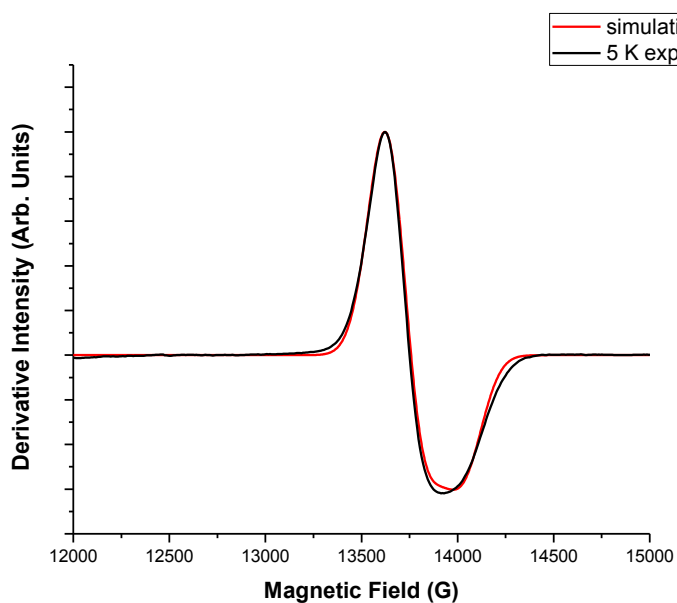
Figure II.8: 5 K Q-band spectrum of a powdered sample of **5** and simulation.

II.4.2 EPR Study of [^{t}BuCONHC$_6$H$_{12}$NH$_2$C$_6$H$_{12}$NHCO^{t}Bu][Cr$_7$MnF$_8$(O$_2$C^{t}Bu)$_{16}$]

Variable temperature EPR measurements were performed on powdered samples of **6**, in a similar fashion to **5**. The EPR spectra obtained give evidence of the population of two different total spin states between 5 K and 20 K. By observing the temperature dependences of the resonances the transitions have been assigned to a $S = 1$ spin ground state and an $S = 2$ excited state. The $S = 1$ transitions decrease in intensity with increasing temperature. The $S = 2$ transitions increase in intensity with increasing temperature. Figure II.9 shows the assignment of these transitions.
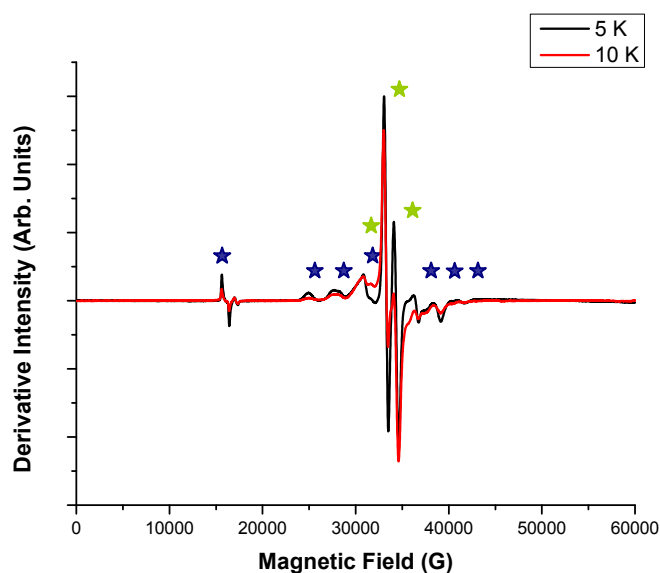
Figure II.9: EPR spectrum of a powdered polycrystalline sample of **6** at W-band frequency at 5 K and 10 K. Blue stars indicate that the resonance originates from the ground spin state and green stars are from the next adjacent excited state.

The two spin states have been modelled independently. Then each calculated spectrum is normalized to the most intense transition of that spin state. The two calculated spectra are then added together. Figure II.10 shows the modelled and

64

experimental spectra of **6**. The following parameters were obtained: $S = 1$, $D_{s=1} =$ +0.800 cm^{-1}, $E_{S=1} = 0.085$ cm^{-1}, $g_{xy} = 2.00$ and $g_z = 2.05$; S = 2, $D_{S=2} = +0.185$ cm^{-1}, E not determined, $B^4_0 = -7.5 \times 10^{-4}$ cm^{-1}, $g_{xz} = 2.00$, $g_y = 1.98$ with a Gaussian isotropic line width of 200 G, where B^4_0 is a fourth order term in the SEL spin Hamiltonian, this term removes the degeneracy of the m_s states of the S = 2 spin state in zero field. These are the same parameters as those previously determined for single crystal and powder samples of [H$_2$NMe$_2$][Cr$_7$MnF$_8$(O$_2$C^{t}Bu)$_{16}$] (**6**).[8]
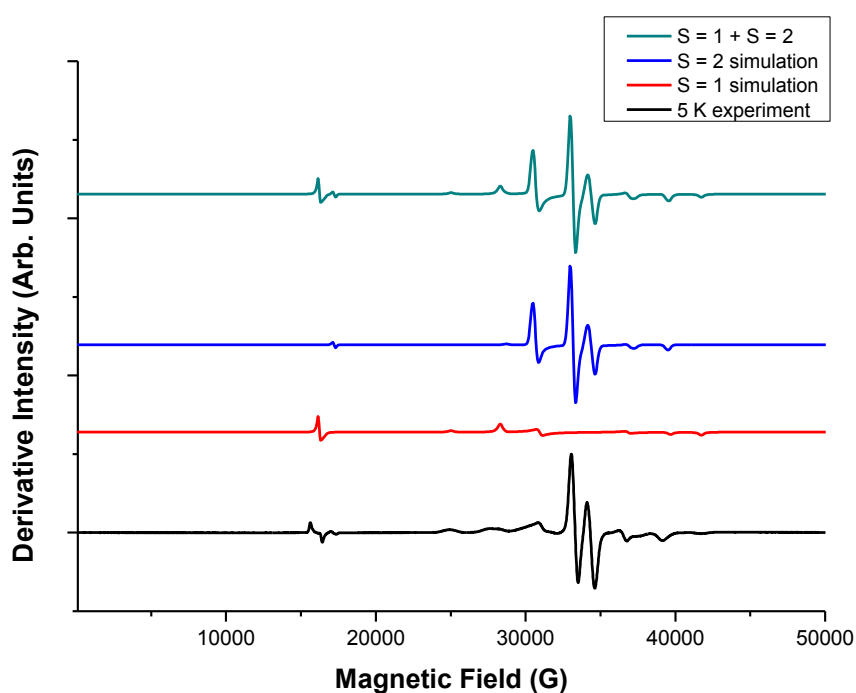
Figure II.10: 5 K W-band experimental powder EPR spectrum and simulation of **6**. The following spin-Hamiltonian parameters that have been used to fit the experimental spectrum; $S = 1$: $D = +0.800$ cm^{-1}, $E = 0.085$ cm^{-1}, $g_{xy} = 2.00$ and $g_z = 2.05$; $S = 2$: $D = 0.185$ cm^{-1}, $B^4_0 = -7.5 \times 10^{-4}$ cm^{-1}, $g_{xz} = 2.00$ and $g_y = 1.98$. At frequency $v = 94.5186$ GHz, with Gaussian isotropic line-widths of 200 G.
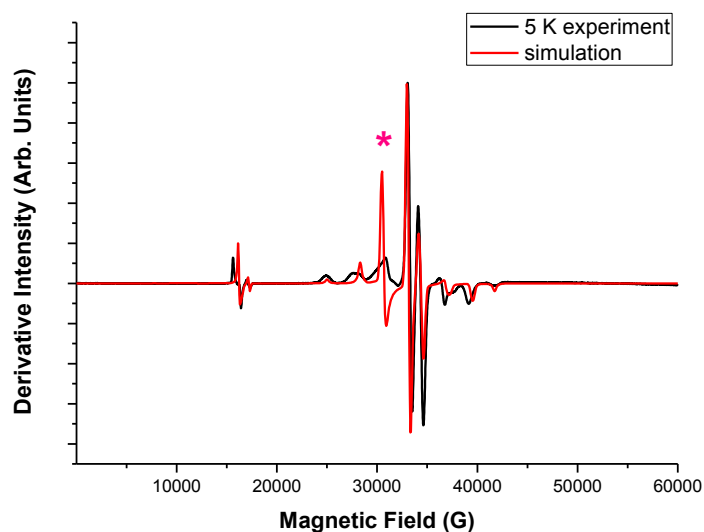
Figure II.11: 5 K W-band spectrum of a powdered sample of **6** and $S = 1+ S = 2$

simulation.

A good fit of the $S = 1$ resonances is achieved with these parameters. However the amplitude of the $S = 2$ resonance at ~30,875 G (pink asterisk) is not very well reproduced in the simulation. This is probably due to a D-strain effect which we have not included in the model. Figure II.12 compares the 5 K W-band spectra of compounds **2**[8] and **6**, showing that the spin Hamiltonian parameters are unchanged with the change in templating cation.
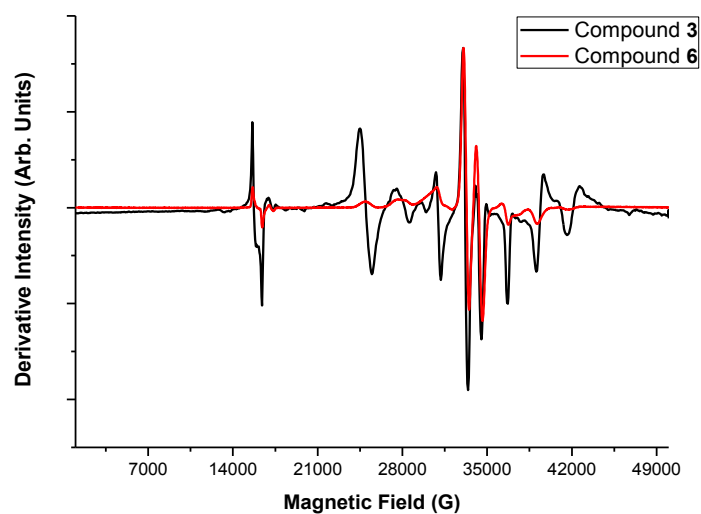
Figure II.12: Comparison of powder EPR spectra of compounds **6** (red line) and **3** (black line) at W-band frequency.

II.4.3 EPR Study of [^{t}BuCONHC$_6$H$_{12}$NH$_2$C$_6$H$_{12}$NHCO^{t}Bu][Cr$_7$ZnF$_8$(O$_2$C^{t}Bu)$_{16}$]

Compound **7** gives rich, temperature dependent EPR spectra between 5 and 20 K. EPR measurements were performed on a powdered sample of **7** at Q- and W-band frequencies in a similar fashion to the previous compounds. By observing the temperature dependence of the EPR resonances recorded between 5 K and 20 K, they can be assigned to two different spin states (Figure II.13). The ground state is $S = {}^3/_2$, with an excited state of $S = {}^5/_2$.
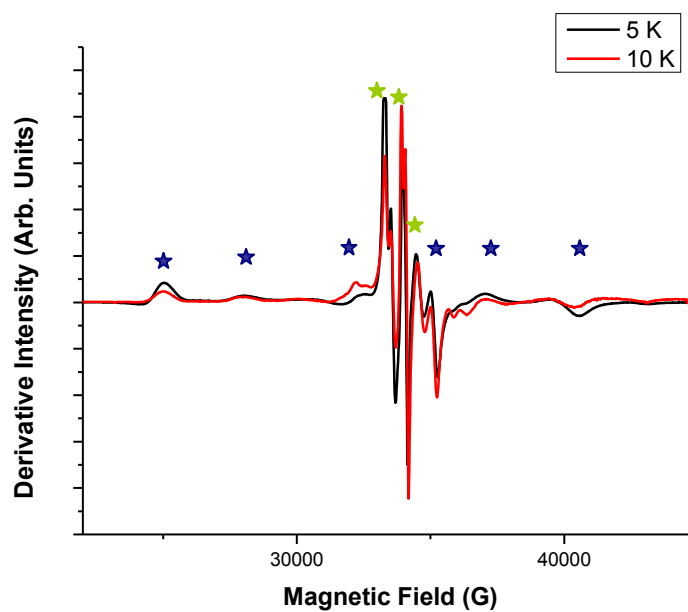
Figure II.13: EPR spectrum of a powdered polycrystalline sample of **7** at W-band frequency at 5 K and 10 K. Blue stars indicate that the resonance originates from the ground spin state and green stars are highlighting the resonances from the next excited spin state.

The following spin-Hamiltonian parameters are used to model the spin ground state, $D_{3/2} = 0.41$ cm^{-1}, $E_{3/2} = 0.051$ cm^{-1}, $g_{iso} = 2.00$. The $S = {}^5/_2$ resonances can be modelled with $D_{5/2} = 0.035$ cm^{-1} and $g_{iso} = 2.00$ (Figure II.14).
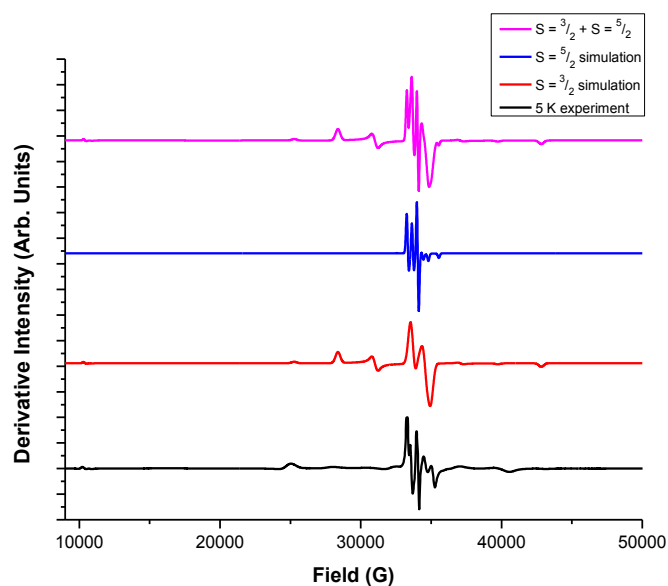
Figure II.14: 5 K W-band experimental powder EPR spectrum and simulation of **7**. The following spin-Hamiltonian parameters that have been used to fit the experimental spectrum; $S = {}^{3}/_{2}$: $D = 0.41$ cm^{-1}, $E = 0.041$ cm^{-1}, and $g_{iso} = 2.00$. $S = {}^{5}/_{2}$: $D = 0.035$ cm^{-1} and $g_{iso} = 2.00$. At frequency, $v = 95.31050$ GHz and with Gaussian isotropic line-widths of 200 G.
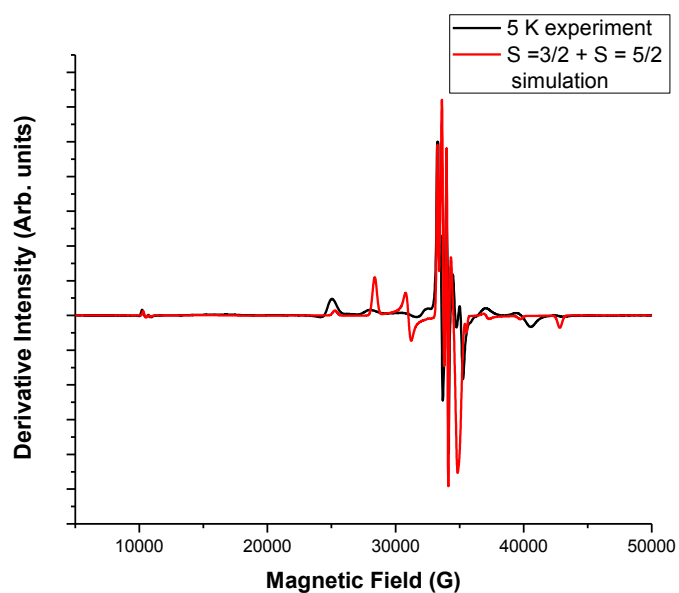
Figure II.15: 5 K W-band spectrum of a powdered sample of **7** and $S = {}^{3}/_{2} + S = {}^{5}/_{2}$ simulation.

The spin-Hamiltonian parameters that have been used are identical to those used in the modelling of the EPR spectra of compound **4**,[8] (Figure II.16) and there are only minor differences in the spectra.
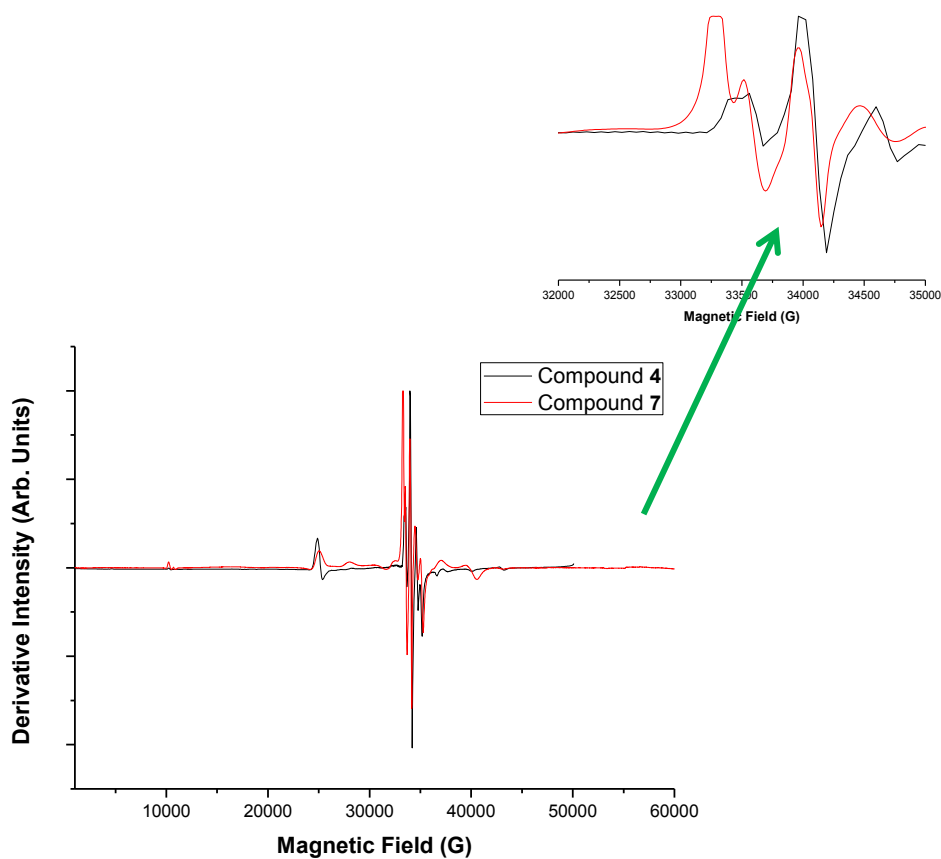
Figure II.16: Comparison of powder EPR spectra of compounds **4** (black line) and **7** (red line) at W-band frequency.

However, one notable difference is that ratio of the resonances at 33,400 G and 34,050 G is not the same for compounds **7** and **10**. Attempts have been made to recreate this feature in the modelling, but have been unsuccessful.

II.4.4   EPR Study of [Cs⊂Cr$_7$NiF$_8$(O$_2$C^{t}Bu)$_{16}$]·0.5MeCN

Multi-frequency spectra of polycrystalline samples were recorded at X- and Q-band frequencies. Low temperature Q-band spectra (Figure II.17) are consistent with an $S = \frac{1}{2}$ ground state, as with the Cr$_7$Ni wheels with other templates. However, there is a significant variation in g-values. Compound **8** has considerable less g-anisotropy than **2**.
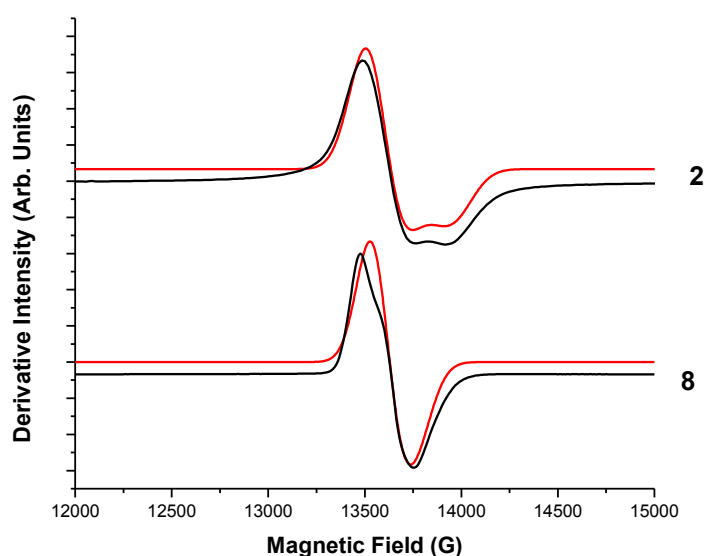
Figure II.17: Comparison powder EPR spectra of compound **2** and **8** at Q-band frequency. The black lines are experimental data and the red lines are simulation. Compound **2**: g_{xy} = 1.79, g_z = 1.74, isotropic Gaussian line widths of 100 G. Compound **8**: g_{xy} = 1.79, g_z = 1.77, isotropic Gaussian line widths of 100 G.

The EPR spectra of **8** can be modelled with the following spin-Hamiltonian parameters: g_{xy} = 1.79 and g_z = 1.77. Compound **2** can be modelled with g_{xy} = 1.780 and g_z = 1.740. Isotropic Gaussian line widths of 100 G have been used in both simulations.

II.4.5   EPR Study of [Cs⊂Cr$_7$MnF$_8$(O$_2$C^{t}Bu)$_{16}$]·0.5MeCN

Variable temperature EPR measurements were performed at X-, Q- and W-band frequencies on powdered samples of **9**. Analysis of the wheel within the coupling scheme given in Figure II.18 indicates that **9** has a ground spin state of $S = 1$, this is confirmed by the EPR measurements. The $S = 1$ spin ground state of compound **9** can be modelled with the following spin-Hamiltonian parameters: $D_{S = 1} = 0.700$ cm^{-1}, $E_{S = 1} = 0.07$ cm^{-1}, g$_{xy} = 2.00$ and g$_z = 2.02$. The $S = 2$ excited state can be modelled with: $D_{S = 1} = 0.075$ cm^{-1} and g$_{iso} = 1.98$. Gaussian line widths of 200 G have been used throughout. The 5 K W-band spectrum of compound **9** and simulation are shown in Figures II.18 and II.19.
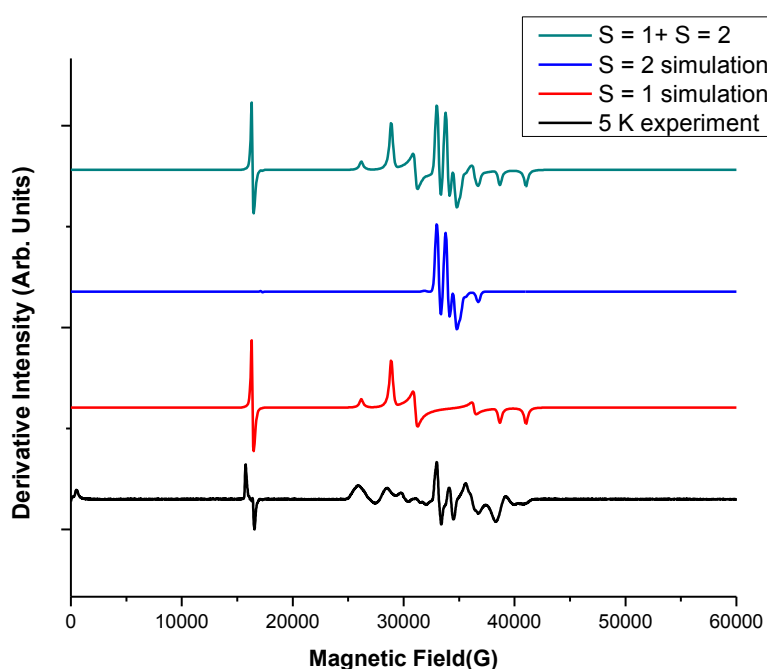
Figure II.18: 5 K W-band experimental powder EPR spectrum and simulation of **9**. The following spin-Hamiltonian parameters that have been used to fit the experimental spectrum; $S = 1$: $D = 0.70$ cm^{-1}, $E = 0.07$ cm^{-1}, g$_{xy} = 2.00$ and g$_z = 2.02$. S = $^5/_2$: $D = 0.075$ cm^{-1} and g$_{iso} = 1.98$. At frequency, $v = 95.31050$ GHz and with Gaussian isotropic line-widths of 200 G.

Figure II.19 consists of the $S = 1 + S = 2$ simulation and 5 K W-band experiment overlaid, the simulation is a good fit of the experimental data.
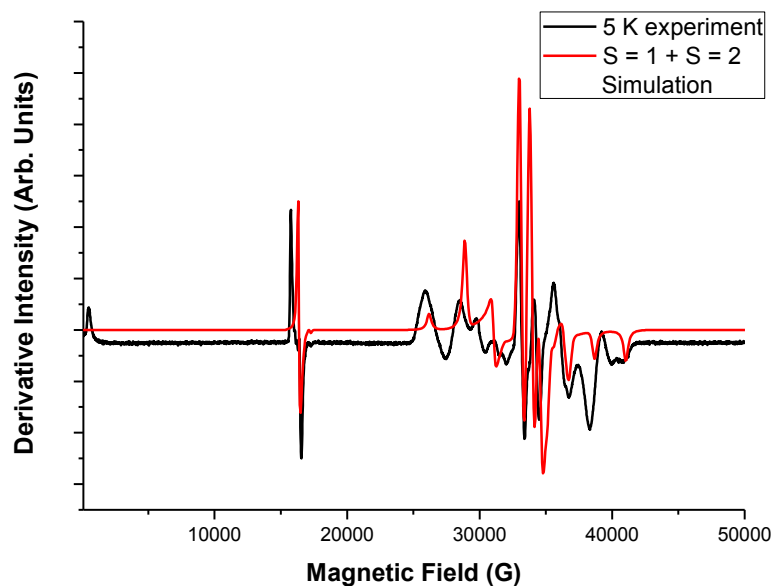
Figure II.19: 5 K W-band frequency spectrum of compound **9** and simulation.

The D values for the $S = 1$ ground state and the $S = 2$ excited state are significantly smaller in compound **9** than **3**. Figure II.20 compares the W-band 5 K spectra of **9** and **3**, highlighting the much narrower spread of resonance fields.
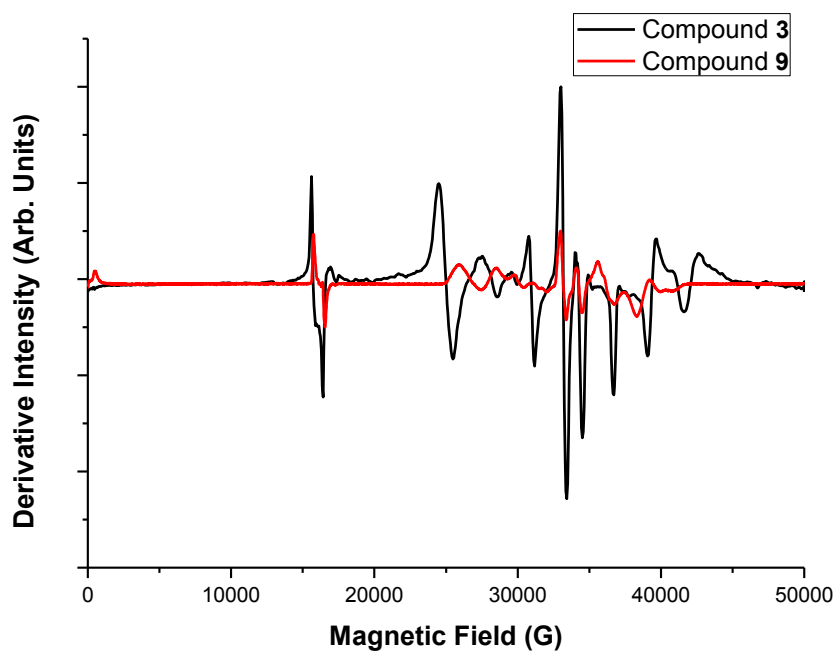
Figure II.20: Comparison of powder EPR spectra of compounds **3** (black line) and **9** (red line) at W-band frequency.

II.4.6 EPR study of [Cs⊂Cr$_7$ZnF$_8$(O$_2$C^{t}Bu)$_{16}$]·0.5MeCN]

EPR spectra were measured at Q- and W-band frequencies of a powdered sample of compound **10**. Confirming that there is an spin ground state of $S = ^3/_2$ and an excited state of $S = ^1/_2$. The $S = ^3/_2$ spin ground state can modelled with the following spin-Hamiltonian parameters: $D_{S = 3/2} = 0.32$ cm^{-1}, $E_{S = 3/2} = 0.035$ cm^{-1}, $g_{xy} = 2.00$ and $g_z = 2.03$. The $S = ½$ excited state can be modelled with an isotropic g-value of 2.00.
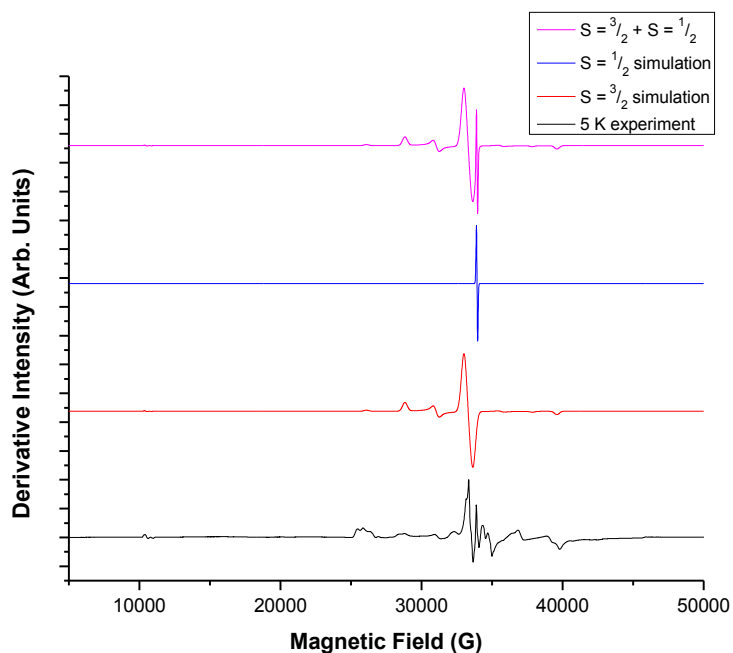
Figure II.21: 5 K W-band experimental powder EPR spectrum and simulation of **10**. The following spin-Hamiltonian parameters that have been used to fit the experimental spectrum; $S = ^3/_2$: $D = 0.32$ cm^{-1}, $E = 0.035$ cm^{-1}, $g_{xy} = 2.00$ and $g_z = 2.03$. $S = ^1/_2$: $g_{iso} = 2.00$. At frequency, $v = 93.3338$ GHz and with Gaussian isotropic line-widths of 200 G.
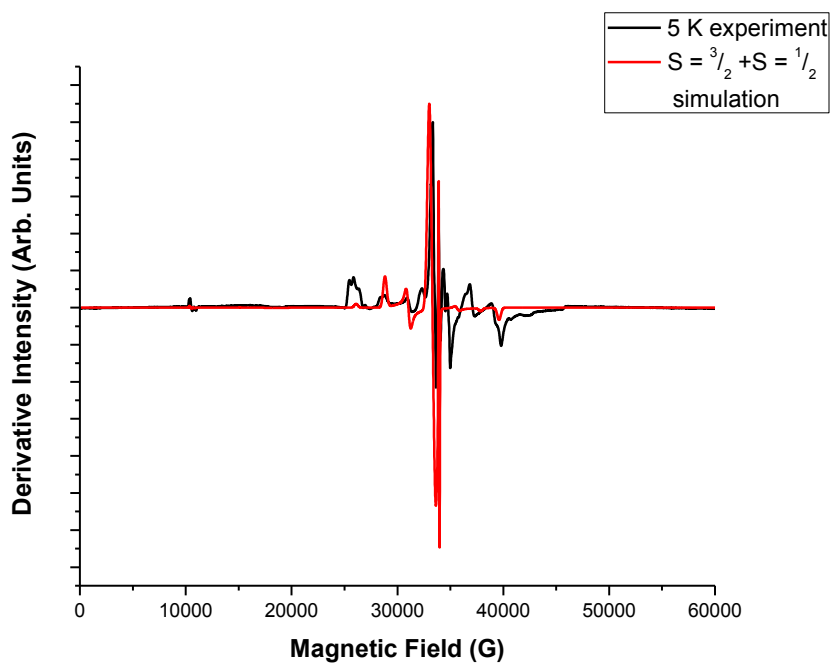
Figure II.22: 5 K W-band spectrum of compound **10** and $S = ^3/_2 + S = ^1/_2$ simulation.

Figure II.23 compares the 5 K W-band EPR spectra of compounds **4** and **10**. Again, there is a significantly smaller *D* value for the caesium templated wheel, shown by the smaller spread of the resonances. Compound **10** is different from the other Cr_7Zn wheels with other templating cations, because there is an $S = {}^1/_2$ excited state rather than an $S = {}^5/_2$ excited state.
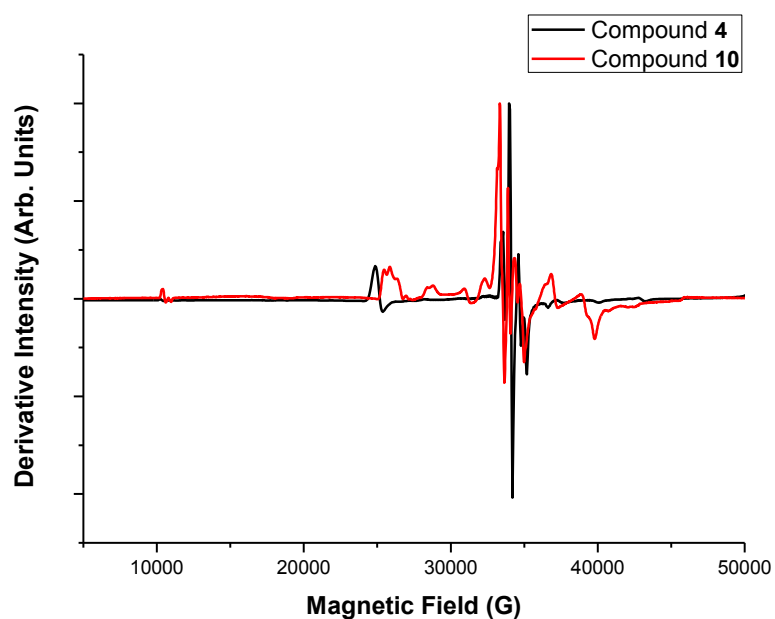
Figure II.23: Comparison of powder EPR spectra of compounds **4** (black line) and **10** (red line) at W-band frequency.

II.5   Discussion and Conclusions

The rotaxane-Cr_7M wheels (**6** and **7**), can be modelled with identical ground state *D* and *E* values to those provided for the dimethylammonium templated wheels (**3** and **4**).[8] The EPR spectra of compound **5** has a very similar set of g-values as previously reported for compound **2**. The caesium templated wheels are spectroscopically

different. The D value for the ground spin state of **9** and **10** is significantly smaller than those determined for the dimethylammonium templated wheels, D = +0.70 cm^{-1} for **9**, +0.80 cm^{-1} for **3**, +0.32 cm^{-1} for **10** and +0.41 cm^{-1} for **4**. The rhombicity (λ = E/D) of the two families is very different. For the ground spin state of **9** and **10**, λ = 0.109. For **3** λ = 0.106 and for **4** λ = 0.100. Apart from **2** and **5**, line widths of 200 G have been used throughout the green wheel family to model the spectroscopic data. Two different types of Cr$_7$M wheels have been discussed: rotaxane-Cr$_7$M wheels and caesium templated Cr$_7$M wheels. It has been found that when the wheels are templated with a long dialkylammonium group, the spectroscopic properties of the wheel are not altered. This is an expected result; The MPLN for compounds **5** to **7** is 0.175 Å and for **2** to **4** is 0.180 Å. The MPLN values are similar; therefore the wheels have very similar geometries and we should not expect any significant change in electronic structure. There are more significant differences in the spin Hamiltonian parameters of the caesium templated wheels. There is a ~20 % decrease in the ground state D values of **9** and **10** in comparison to the dialkylammonium templated wheels. The ground state g-values of **8** are more isotropic than the g-values of the Cr$_7$Ni dialkylammonium templated wheels. The local coordination spheres of the metal ions are identical in all "green" wheels; therefore it is unlikely that there are significant differences in the local ZFS of the metal centres. It is more likely that the differences in spectroscopic parameters originate from the differences in MPLN values, the MPLN of **8** to **10** is 0.148 Å. This means the metal ions have a more planar arrangement in comparison to the dimethylammonium templated wheels. This increase in symmetry is induced by the templating caesium ion. The central caesium ion is coordinated to all of the bridging fluoride atoms, inducing a greater symmetry. Whereas in the dialkylammonium templated molecular wheels there are only hydrogen bonding interactions between two of the bridging fluoride ions and the hydrogen's of the dialkylammonium cation. This will affect the relative orientations of the local ZFS and hence their projection onto the total

D of the ground spin state. The caesium templated wheels may have greater alignment of local ZFS, which would result in a smaller D of the total spin state.

II.6 References

1.   V. Aucagne, D. A. Leigh, J. S. Lock and A. R. Thomson, *J. Am. Chem. Soc.*, 2006, **128**, 1784-1785.

2.   A. G. Kolchinski, D. H. Busch and N. W. Alcock, *J. Chem. Soc., Chem. Commun.*, 1995, 1289-1291.

3.   M. L. Mock, T. A. Irra, J. P. Wepsiec and M. Adhya, *J. Org. Chem.*, 1989, 5302-5308.

4.   D. B. Amabilino and J. F. Stoddart, *Chem. Rev.*, 1995, **95**, 2725-2828.

5.   R. W. Saalfrank, I. Bernt, E. Uller and F. Hampel, *Angew. Chem. Int. Ed.*, 1997, **36**, 2482-2485.

6.   T. B. Faust, P. G. Heath, C. A. Muryn, G. A. Timco and R. E. P. Winpenny, *Chem. Commun*, 2010, **46**, 6258-6260.

7.   SHELX-PC Package, Bruker Analytical X-Ray Systems, Madison, WI, 1998.

8.   S. Piligkos, Ph.D. Thesis, The University of Manchester (Manchester, UK), 2004.

III Physical Studies on a Family of purple-Cr$_7$M Molecular Wheels: Isostructural Compounds with Different Ground Spin States

III.1 Introduction

The physical properties of a family of isostructural heterometallic wheels of the form [$Cr_7M^{2+}F_3$(Etglu)(O_2C^tBu)$_{15}$(L)], where M is a divalent metal cation (M^{2+} = Mn, Zn, Ni; Etglu = *N*-ethyl-*D*-glucamine) have been investigated. These compounds are a vibrant purple colour and hereafter for simplicity shall be named purple-Cr_7M. These single purple-Cr_7M wheels can be linked together through coordination chemistry into larger supramolecular structures. The purpose of this project is to determine the spin-Hamiltonian parameters and therefore the electronic structure of purple-Cr_7M wheels. The characterization of the single purple-(Cr_7Ni) wheels will aid the understanding of the subtle interactions between wheels in the larger linked supramolecular systems.

III.2 A Structural Description of the Purple-Cr$_7$M Wheels

The octanuclear wheel is formed in the reaction of *N*-ethyl-*D*-glucamine (Figure III.1), chromium(III) fluoride tetrahydrate, the appropriate metal carbonate and an excess of pivalic acid. The yield of this reaction is around 30 %.[1]

$7CrF_3{\cdot}4H_2O$ + $^1/_5$[$2NiCO_3{\cdot}3Ni(OH)_2{\cdot}4H_2O$] + H_5Etglu + xs HO_2C^tBu →
[Cr_7MF_3(Etglu)(O_2C^tBu)$_{15}$(H_2O)]
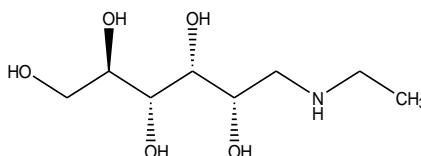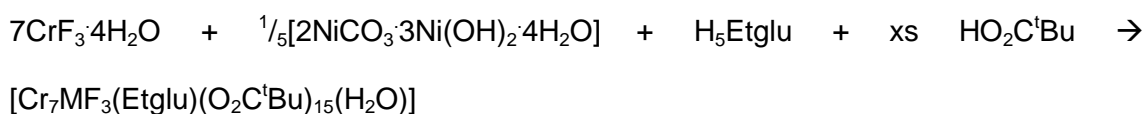
Figure III.1: The templating molecule *N*-ethyl-*D*-glucamine.

There are seven Cr^{3+} ions and a single heterometal ion which form an octagon of metal centres (Figure III.2) The formation of the cluster is templated around a chiral *N*-ethyl-*D*-glucamine molecule which is penta-deprotonated and bound to the metal sites through all available O-donors, forming five bridging alkoxide groups inside the wheel. The other three remaining sites inside the wheel are bridged by fluoride ions. For seven of the eight edges of the octanuclear wheel there are two bridging carboxylate groups and at the eighth edge there is only a single bridging pivalate and one bridging fluoride ion. At the heterometal site there is a terminal ligand, which is a water molecule in the original preparation. If the compound is recrystallized, the terminal ligand can be an acetonitrile or diethyl ether molecule, this ligand is circled in Figure III.2. To summarize there are five different metal coordination environments, making this a rather complex system.
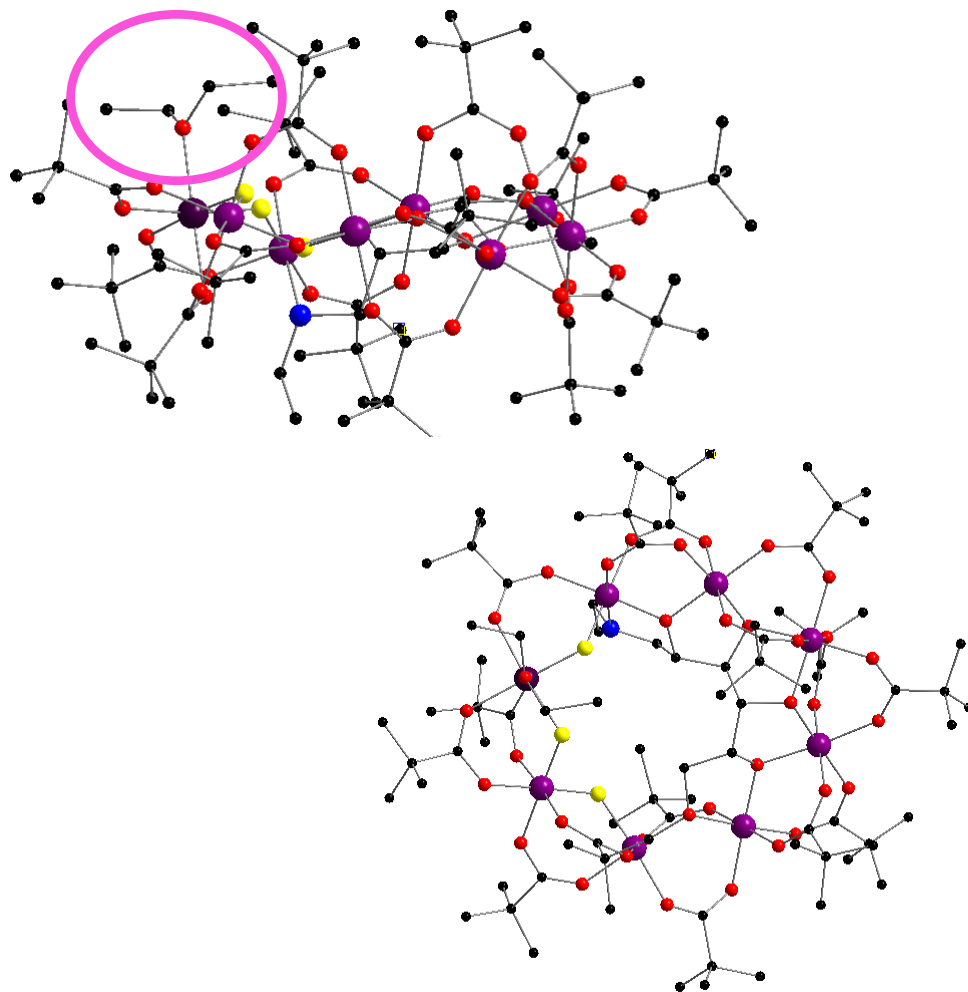
Figure III.2: Side and top views of $[Cr_7M^{2+}F_3(Etglu)(O_2C^tBu)_{15}(Et_2O)]$, M^{2+} = Mn, Zn, Ni. Colours; Cr atoms: purple; M atom: green; C atoms: black; F atoms: yellow; N atoms: blue; O atoms: red. All H atoms have been removed for clarity. The labile terminal ligand at the heterometal site is circled in pink.[1]

The terminal ligand can also be substituted for a variety of N-donor organic ligands. For example 4-phenylpyridine, which occupies a site which is perpendicular to the plane of the wheel (Figure III.3)
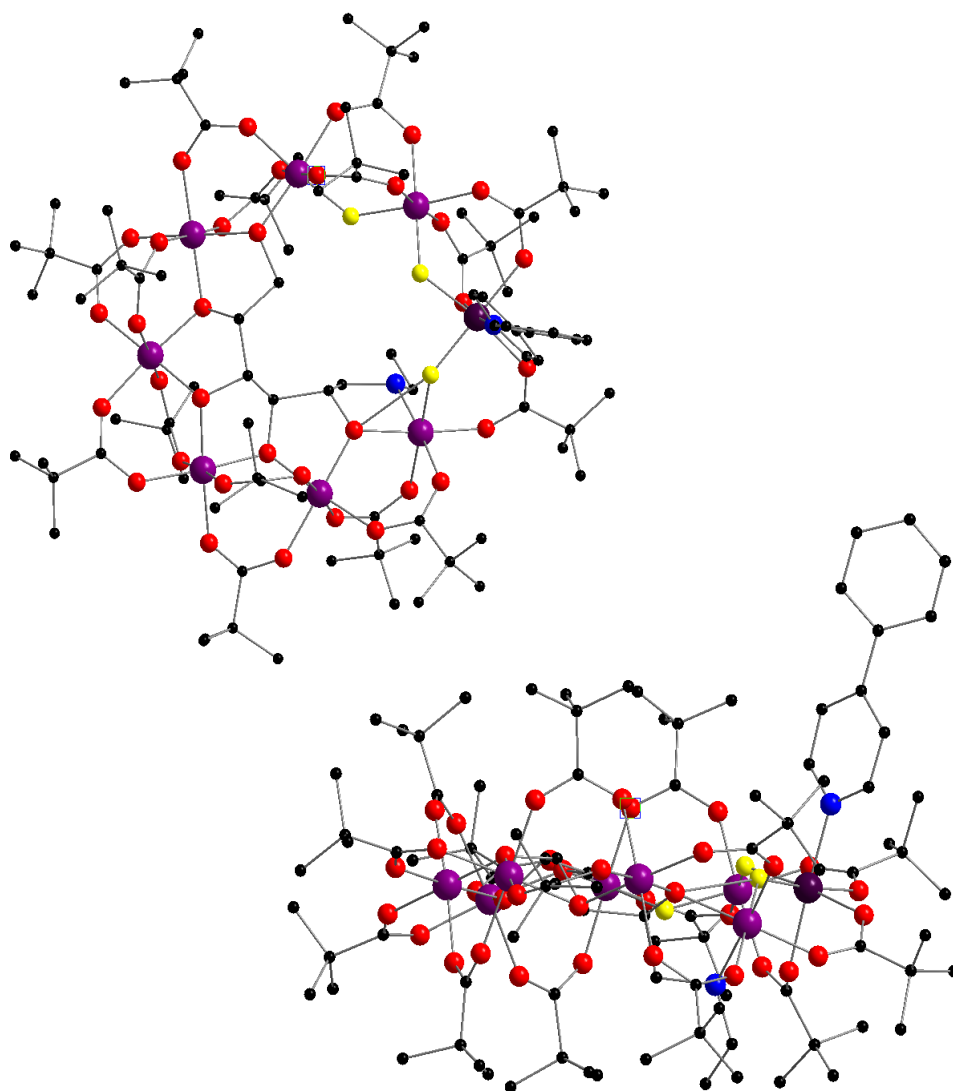
Figure III.3: Side and top views of [Cr$_7$MF$_3$(Etglu)(O$_2$C^{t}Bu)$_{15}$(phpy)], M^{2+} = Mn, Zn, Ni.

This chapter will discuss the physical properties of the purple-Cr$_7$M wheels with 4-phenylpyridine at the heterometal site. These types of wheels have been chosen as it closely models "half" of the dimeric systems formed when N,N-bridging ligands (*e.g.* 4,4'-bipyridine) are used. These systems shall be discussed in chapter IV.

III.3 Results and Discussion

III.3.1 Magnetic Measurements of the Purple-Cr$_7$M Wheels

Magnetic susceptibility measurements were performed on compounds [Cr$_7$NiF$_3$(Etglu)(O$_2$C^{t}Bu)$_{15}$(phpy)] (**11**), [Cr$_7$MnF$_3$(Etglu)(O$_2$C^{t}Bu)$_{15}$(phpy)] (**12**) and [Cr$_7$ZnF$_3$(Etglu)(O$_2$C^{t}Bu)$_{15}$(phpy)] (**13**). For compounds **11** to **13** the $\chi_m T$ at 300 K has a value of 11.66 emu K mol^{-1} for **11**, 17.03 emu K mol^{-1} for **12** and 11.37 emu K mol^{-1} for **13**. These values are somewhat smaller the calculated values ($\chi_M T = \sum \frac{g_i^2}{8} S_i(S_i + 1)$, where g = 2.00) for seven non interacting Cr^{3+} ions and the appropriate heterometal, which is 14.13 emu K mol^{-1} for **11**, 17.50 emu K mol^{-1} for **12** and 13.13 emu K mol^{-1} for **13**. The value of $\chi_m T$ falls as the temperature falls for each of the compounds; which indicates that there is antiferromagnetic exchange within the rings. The 2 K value of $\chi_m T$ for **11** is 0.31 emu K mol^{-1}, for **12** is 0.99 emu K mol^{-1} and for **13** is 1.76 emu K mol^{-1}. This is consistent with ground spin states of $S = \frac{1}{2}$ for **11**, $S = 1$ for **12** and $S = \frac{3}{2}$ for **13**. The ground spin states are confirmed further by field dependent magnetization measurements at 2 K, the Brillouin function saturates at 0.99 N_β for **11**, 2.09 N_β for **12** and 3.02 N_β for **13** ($M_{sat} = gS$).

The magnetic susceptibility and magnetization data has been modelled with the following exchange spin-Hamiltonian:

$$\hat{H} = -2_{(i,j)} \sum_{\substack{i \neq j}}^{8} \hat{S}_i \hat{S}_j$$

Equation III.1

The magnetic data and simulations of are shown in Figures: III.4 and III.5 (**11**); III.6 III.7 (**12**); III.8 III.9 (**13**). Best fit parameters are in Table III.1 using the exchange scheme defined in Figure III.10.
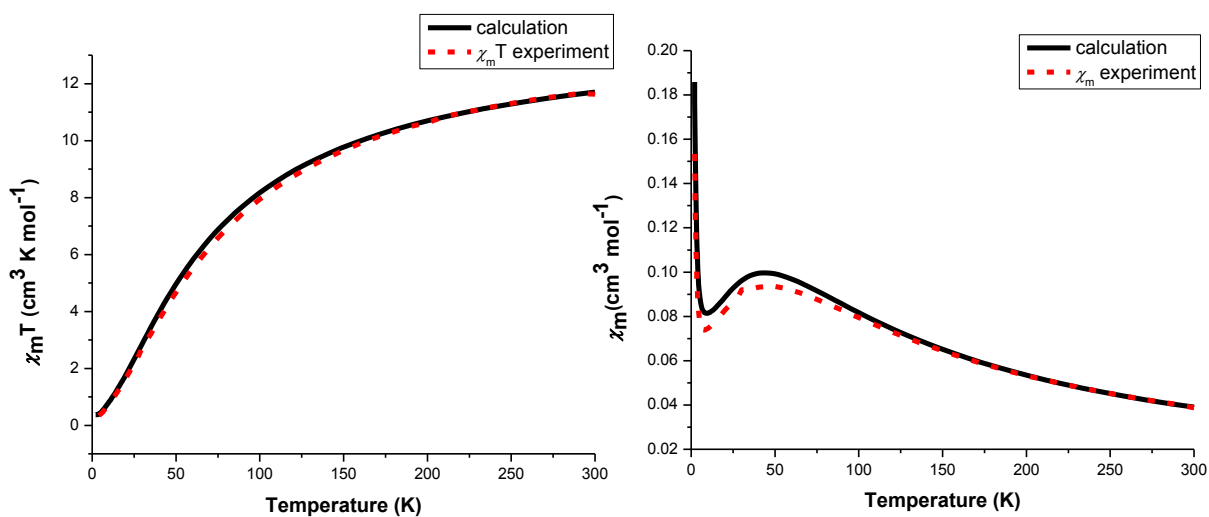
Figure III.4: The magnetic susceptibility data of $[Cr_7NiF_3(Etglu)(O_2C^tBu)_{15}(phpy)]$ (**11**) measured on a polycrystalline powdered sample which was fixed with eicosaine. Left: temperature dependent susceptibility at 0.1 T, Right: temperature dependent susceptibility at 0.1 T plotted as χ_mT vs. T. The solid black lines were calculated with the parameters given in Table III.1.
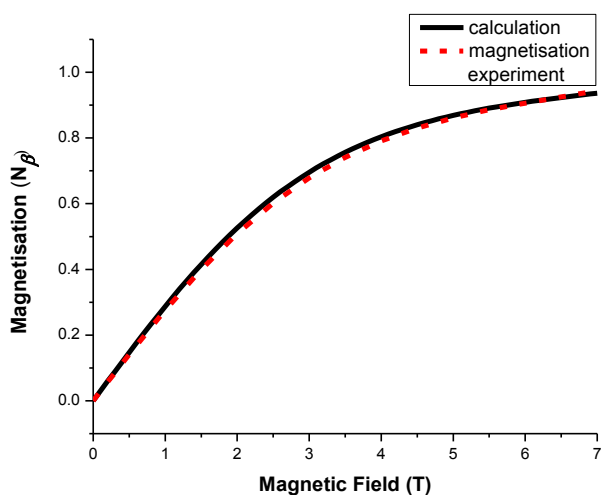
Figure III.5: The field dependent magnetization at 2 K of $[Cr_7NiF_3(Etglu)(O_2C^tBu)_{15}(phpy)]$ (**11**) measured on a polycrystalline powdered sample which was fixed with eicosaine.
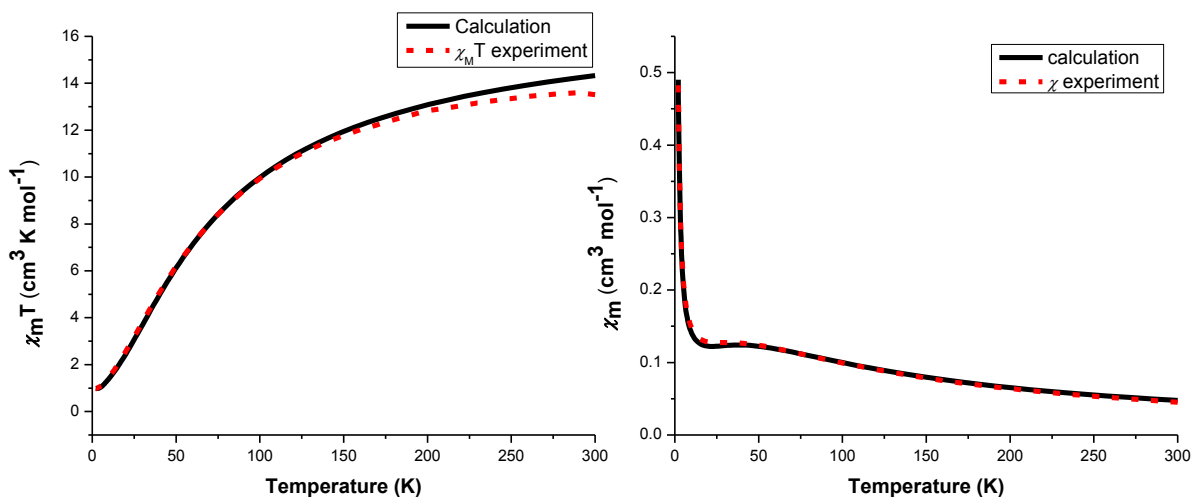
Figure III.6: The magnetic susceptibility data of [Cr$_7$MnF$_3$(Etglu)(O$_2$C^{t}Bu)$_{15}$(phpy)] (**12**) measured on a polycrystalline powdered sample which was fixed with eicosaine. Left: temperature dependent susceptibility at 0.1 T, Right: temperature dependent susceptibility at 0.1 T plotted as $\chi_m T$ vs. *T*.
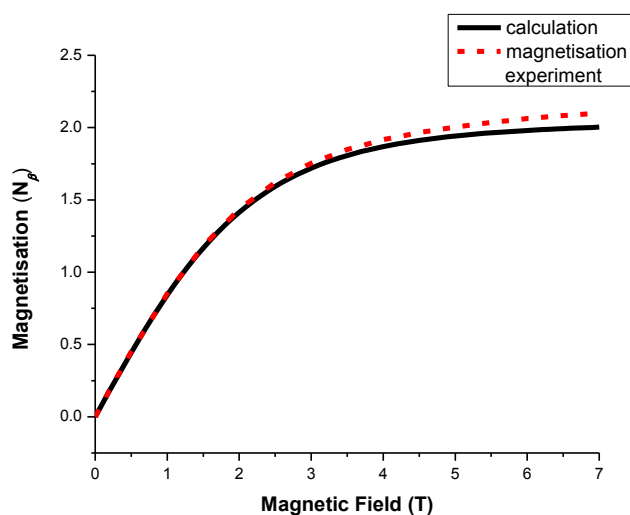
Figure III.7: The field dependent magnetization at 2 K of [Cr$_7$MnF$_3$(Etglu)(O$_2$C^{t}Bu)$_{15}$(phpy)] (**12**) measured on a polycrystalline powdered sample which was fixed with eicosaine.
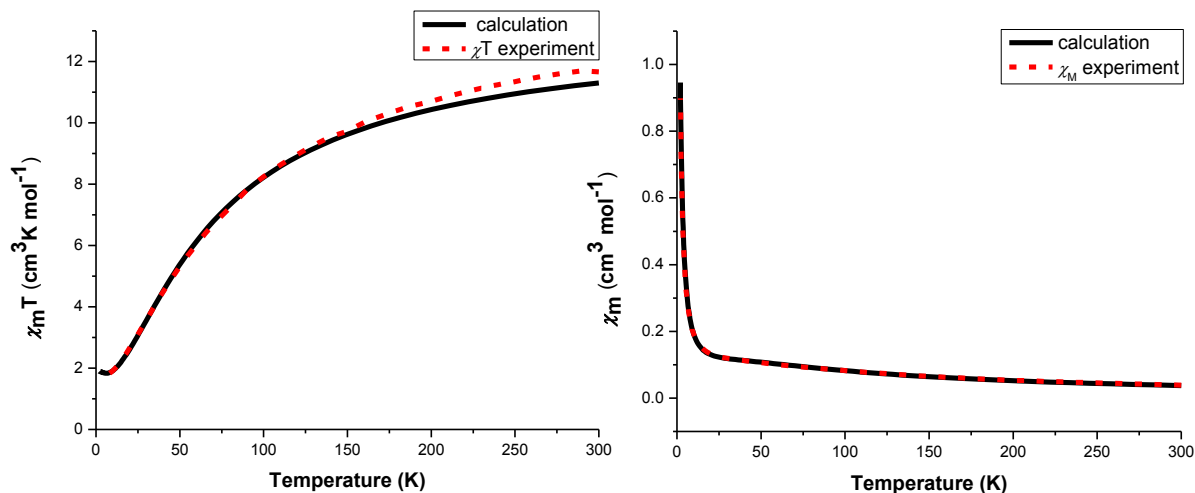
Figure III.8: The magnetic susceptibility data of [Cr$_7$ZnF$_3$(Etglu)(O$_2$C^{t}Bu)$_{15}$(phpy)] (**13**) measured on a polycrystalline powdered sample which was fixed with eicosaine. Left: temperature dependent susceptibility at 0.1 T, Right: temperature dependent susceptibility at 0.1 T plotted as $\chi_m T$ vs. *T*.
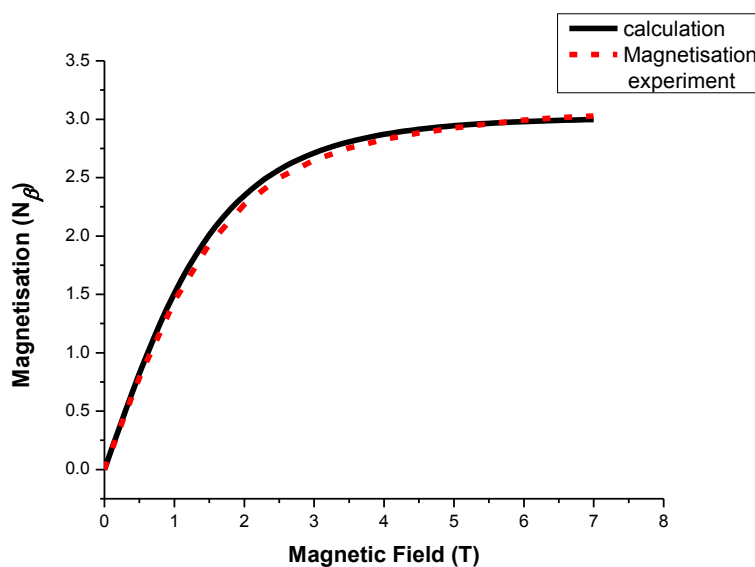
Figure III.9: The field dependent magnetization at 2 K of [Cr$_7$ZnF$_3$(Etglu)(O$_2$C^{t}Bu)$_{15}$(phpy)] (**13**) measured on a polycrystalline powdered sample which was fixed with eicosaine.
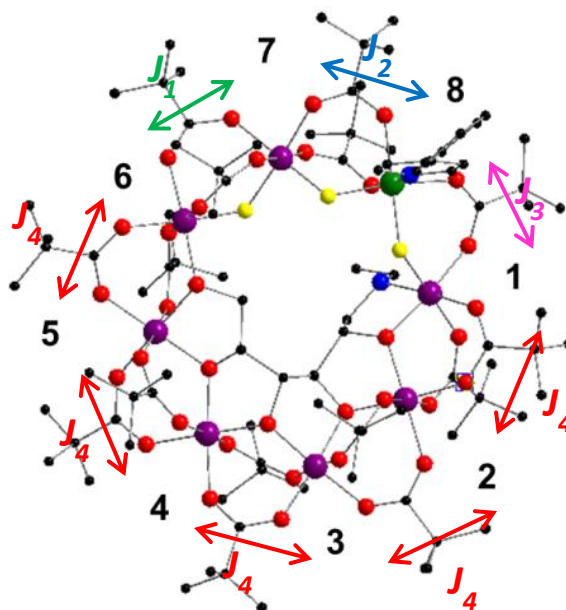
Figure III.10: An annotated picture of a purple-Cr_7M wheel defining the differing J-values used to model the magnetic susceptibility data.

Table III.1: The spin-Hamiltonian parameters which have been used to model compounds **11**, **12** and **13**.

Parameter	Purple-Cr_7Ni (**11**)	Purple-Cr_7Mn (**12**)	Purple-Cr_7Zn (**13**)
J_1	-5.90 cm^{-1}	- 5.90 cm^{-1}	- 5.90 cm^{-1}
J_2	- 8.66 cm^{-1}	- 6.01 cm^{-1}	n.a.
J_3	- 8.66 cm^{-1}	- 4.00 cm^{-1}	n.a.
J_4	- 8.00 cm^{-1}	- 8.00 cm^{-1}	- 8.00 cm^{-1}
g_{iso} (susceptibility)	1.99	1.98	2.01
g_{iso} (magnetization)	1.88	2.01	1.96

The simplest model would be to model the magnetic data with a single isotropic exchange interaction. The magnetic data of compound **11** has been previously modelled with a single J-value of 8.00 cm^{-1}, a good fit of the experimental data has been achieved with this method.[2] However the magnetic data of compounds **12** and **13** cannot be fitted with a single J-value. Plus it makes little chemical sense to have a single exchange term when there are 8 unique interactions. However there is a need to avoid over-parameterization, so the structure has been analysed and certain parameters have been fixed to literature values. There are four chemically distinct bridging arrangements: (i) Cr-Cr involving a fluoride and two carboxylates, (ii) Cr-M involving one fluoride and two carboxylates, (iii) Cr-M involving one fluoride and (iv) one carboxylate and Cr-Cr involving an alkoxide and two carboxylates. Hence, in our model we use four distinct J-values, J_{1-4} respectively (see Figure III.10). The J_1 interaction is equivalent to what has been determined for the Cr···Cr interaction of green-Cr$_7$M wheels from the modeling of INS and EPR data.[3, 4] The J_2 interaction is also equivalent to Cr···M^{II} interaction in green-Cr$_7$M wheels, hence the J_2 term has also been fixed to literature values. This gives one free variable for **13**, namely J_4, and two for **11** and **12**, namely J_3 and J_4. The J_4 term has been fixed to be common to all three compounds, hence reducing the number of variables further. The g-values have been restrained to be within sensible values. Using this procedure and fitting to the magnetization and the magnetic susceptibility data simultaneously, a good fit of the experimental data has been achieved. Different g-values have been used to model the magnetic susceptibility and the magnetization; this is due to limitations of the MAGPACK software.[5] From the J-values which have been determined a zero-field energy level diagram can be calculated using MAGPACK.[5] The 12 lowest lying spin states of compounds **11, 12** and **13** are shown in Figure III.11.
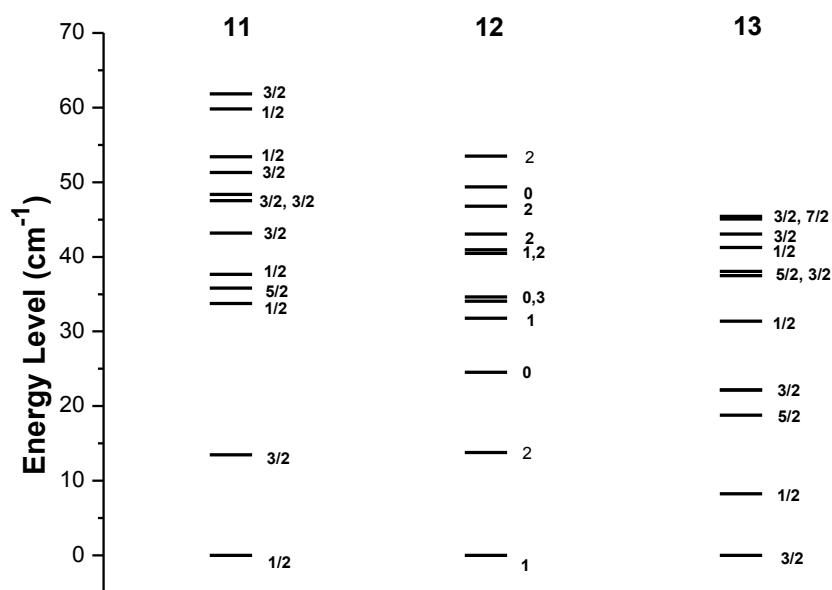
Figure III.11: An zero field energy level diagram of the 12 lowest lying total spin states of **11** purple-(Cr$_7$Ni), **12** purple-(Cr$_7$Mn) and **13** purple-(Cr$_7$Zn). The parameters used to calculate the energy levels are given in Table III.3. This energy level diagram was calculated using the program "MAGPACK".

The calculated ground states of compounds **11**, **12** and **13** are $S = ^1/_2$, 1 and $^3/_2$ respectively, consistent with the low temperature limit of $\chi_m T$ and M_{sat} values. There is a gap between the ground state and the first excited state of 13.46 cm^{-1} for **11**, 13.76 cm^{-1} for **12** and 8.27 cm^{-1} for **13**. Therefore we should not expect the effective spin ground state to be thermally isolated from the first excited state at the liquid helium temperatures.

III.3.2 UV / Visible Absorption Spectroscopy of Purple and Green Cr₇M Wheels
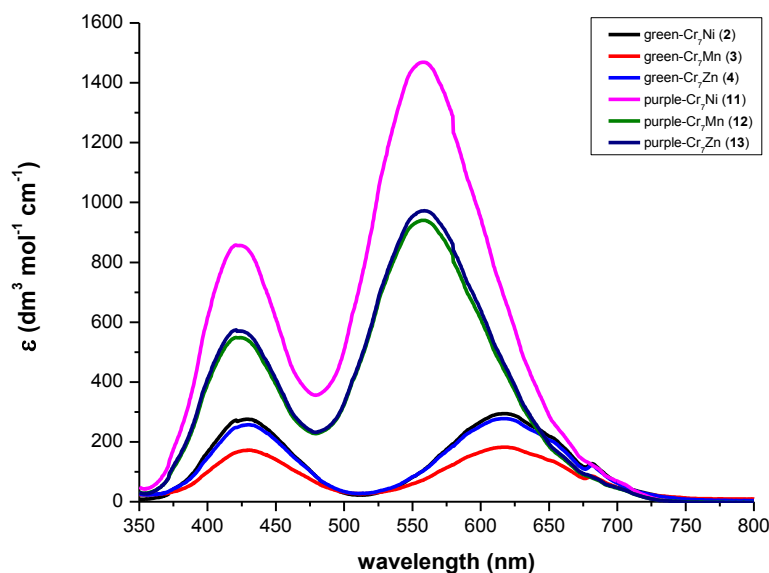
Figure III.12: UV/visible spectra of compounds **2-4** and **11-13**, recorded at room temperature.

The UV/visible spectra of the purple-Cr₇M wheels (**11** to **13**) and the green-Cr₇M (**2** to **4**) have been recorded in hexane at room temperature (Figure III.12). The UV/visible spectra consist of two broad peaks which resemble that of monomeric Cr^{3+} with two of the three expected spin allowed d-d absorptions.[6] The electronic ground state of a d^3 metal ion in octahedral symmetry is $^4A_2$. The peak which is observed in both families at 425 nm, originates from a $^4A_2 \rightarrow {}^4T_1$ transition. The peak which is at 560 nm in the purple family and 625 nm in the green family corresponds to a $^4A_2 \rightarrow {}^4T_2$ transition. The longest wavelength transitions give Δ_{oct} directly: for the purple wheel family this is 17,874 cm^{-1} and for the green family 16,177 cm^{-1}. The value of Δ_{oct} is bigger in the purple wheel family. This is due to the replacement of five very weak field fluorine ligands with stronger field alkoxide ligands in the purple wheels. The molar extinction

coefficients of the purple wheel family are much higher than those of the green wheel family.

III.3.3 EPR Study of [Cr$_7$NiF$_3$(Etglu)(O$_2$C^{t}Bu)$_{16}$(phpy)]

EPR spectra of the molecular wheel [Cr$_7$NiF$_3$(Etglu)(O$_2$C^{t}Bu)$_{16}$(phpy)] (**11**) have been previously reported.[1] As described in section III.3.1, the magnetic measurements show a doublet ground spin state and quartet excited spin state. The EPR data has been modelled with the spin-Hamiltonian shown in *Equation* II.1. The EPR spectrum of **11** at 5 K shows a resonance from an $S = \frac{1}{2}$ state which can be fitted with an axially symmetric set of g-values, g_{xy} = 1.84, g_z = 1.78 and isotropic line widths of 65 G. The EPR spectrum of the green analogue [H$_2$NR$_2$][Cr$_7$NiF$_8$(O$_2$C^{t}Bu)$_{16}$] (**2**) can be modelled with an axially symmetric set of g-values, g_{xy} = 1.84 and g_z =1.74 and isotropic line widths of 100 G (Figure III.13).[7]
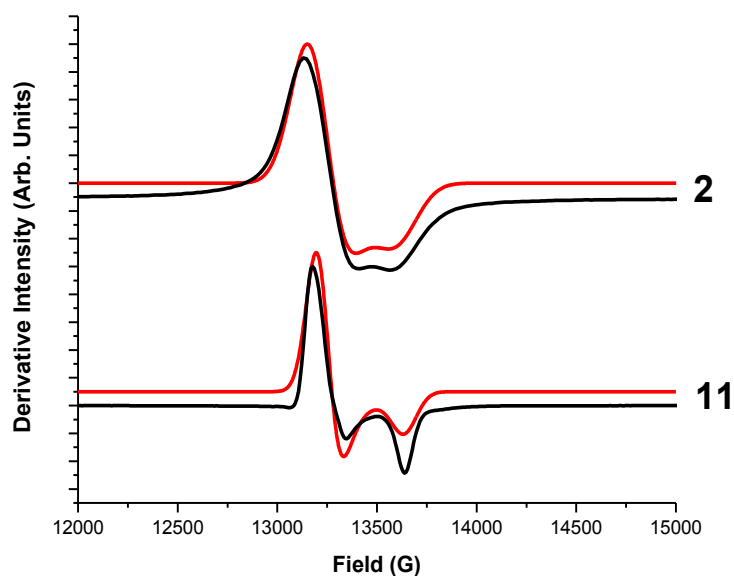
Figure III.13: EPR spectra of polycrystalline samples of [Cr$_7$NiF$_3$(Etglu)(O$_2$C^{t}Bu)$_{16}$(phpy)] (**11**) and [H$_2$NR$_2$][Cr$_7$NiF$_8$(O$_2$C^{t}Bu)$_{16}$] (**2**) at 5 K Q-band frequency.

The g anisotropy is considerably better resolved in compound **11** than in compound **2**. This can be partially attributed to the slightly larger g anisotropy in **11**, but it is largely due to the reduction in line width. The narrower line width of **11** could be due to there being five less bridging fluoride ions (^{19}F, I = ½) which may be a source of unresolved hyperfine interactions.

III.3.4 EPR Study of [Cr$_7$MnF$_3$(Etglu)(O$_2$C^{t}Bu)$_{15}$(phpy)]

A EPR study of the molecular wheel [Cr$_7$MnF$_3$(Etglu)(O$_2$C^{t}Bu)$_{16}$(phpy)], compound **12**, was carried out at X-, Q- and W-band frequencies (Figures III.14, III.15 and III.16 respectively).
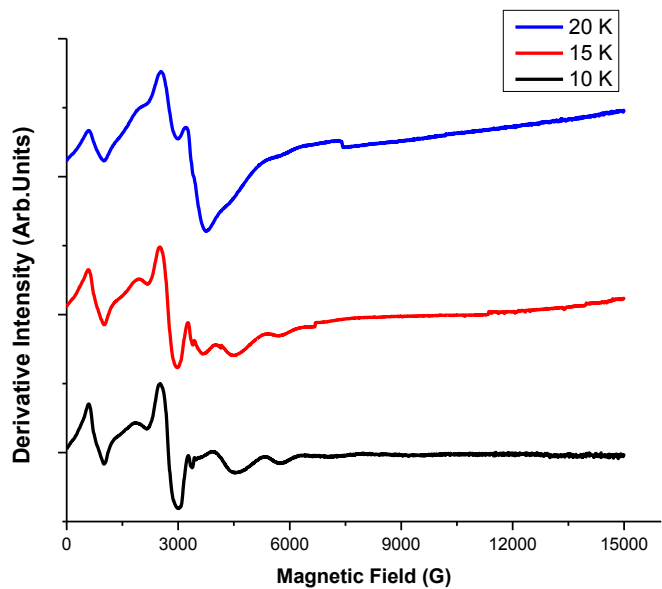
Figure III.14: Variable temperature EPR spectra of a powdered polycrystalline sample of [Cr$_7$MnF$_3$(Etglu)(O$_2$C^{t}Bu)$_{15}$(phpy)] (**12**) at X-band frequency.
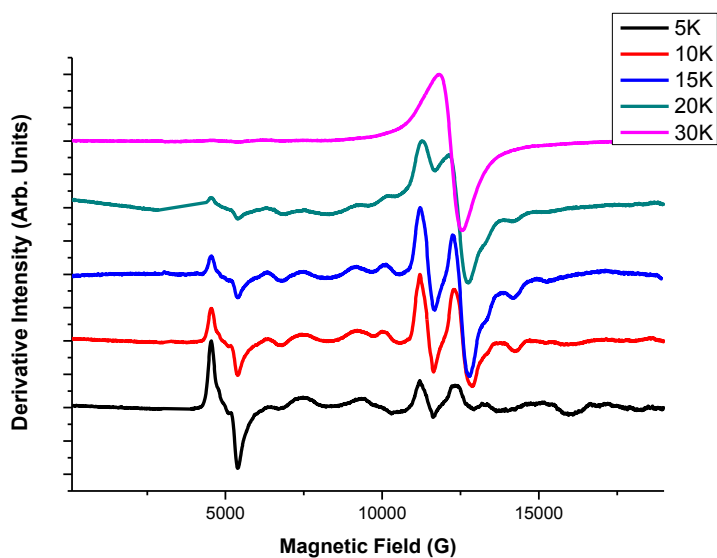
Figure III.15: Variable temperature EPR spectra of a powdered polycrystalline sample of [Cr$_7$MnF$_3$(Etglu)(O$_2$C^{t}Bu)$_{15}$(phpy)] (**12**) at Q-band frequency.
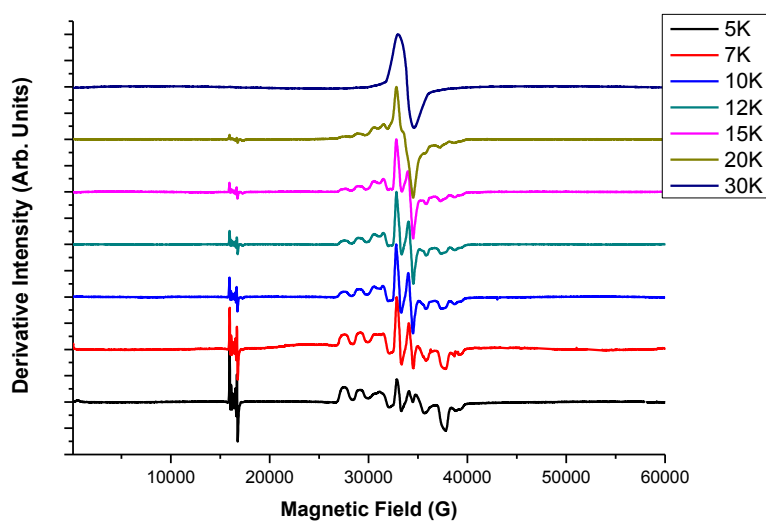
Figure III.16: Variable temperature EPR spectra of a powdered polycrystalline sample of $[Cr_7MnF_3(Etglu)(O_2C^tBu)_{15}(phpy)]$ (**12**) at W-band frequency.

Magnetic measurements and fitting with MAGPACK (see section III.3.1), lead to a picture of the electronic structure where there is an effective ground spin state of $S = 1$, with the first excited spin state being $S = 2$. Below 20 K EPR measurements of polycrystalline powders give rich temperature dependent spectra. At all of the frequencies which were measured, the spectra become much broader above 20 K. By observing the temperature dependences of the resonances it is clear that more than one spin state is populated even at 5 K. This is most apparent at W-band frequency, where the high resolution allows assignment of each resonance to either $S = 1$ or $S = 2$ (Figure III.17).
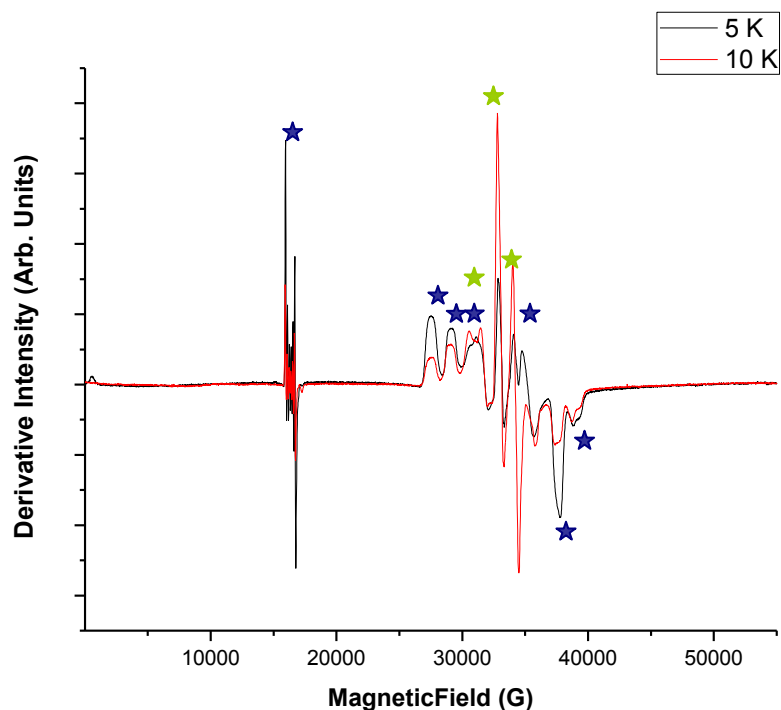
Figure III.17: EPR spectrum of a polycrystalline sample of [Cr$_7$MnF$_3$(Etglu)(O$_2$C^{t}Bu)$_{15}$(phpy)] (**12**) at W-band frequency at 5 K and 10 K. Blue stars indicate that the resonance originates from the ground spin state and green stars are highlighting the resonances from the first excited spin state.

The SEL approach has been used to model the data. Using this assumption, for the purple-(Cr$_7$M) family the ground spin state and the first excited spin state have been modelled independently, and then summed. The S = 1 ground state can be modelled with the following parameters: D = -0.547 cm^{-1}, E = 0.09 cm^{-1} and g$_{iso}$ = 2.01 (Figure III.18). There is not enough resolution to model the S = 2 spin state. To provide enough information to determine the spin-Hamiltonian parameters of the S = 2 spin state a single crystal EPR study needs to be performed.
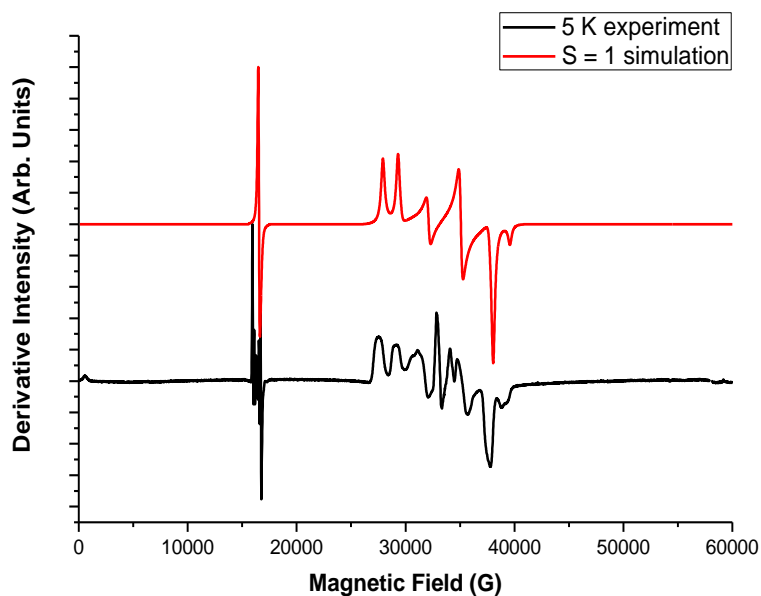
Figure III.18: 5 K W-band experimental powder EPR spectrum and simulation of [Cr$_7$MnF$_3$(Etglu)(O$_2$C^{t}Bu)$_{15}$(phpy)] (**12**) using the following spin-Hamiltonian parameters: S = 1: D = -0.547 cm^{-1}, E = 0.09 cm^{-1}, and g$_{iso}$ = 2.01. At frequency ν = 93.9538 GHz and with Gaussian isotropic line-widths of 100 G.

The resonance at ~ 16,000 G originates from a formally forbidden ΔM_s = ± 2 transition in the S = 1 spin state (Figure III.19), and is sometimes called the half field transition. This formally forbidden transition may be observed when $^D/_{h\nu} < {^3/_4}$.[8] It is observed at a field position which is roughly half of that for g ≈ 2.
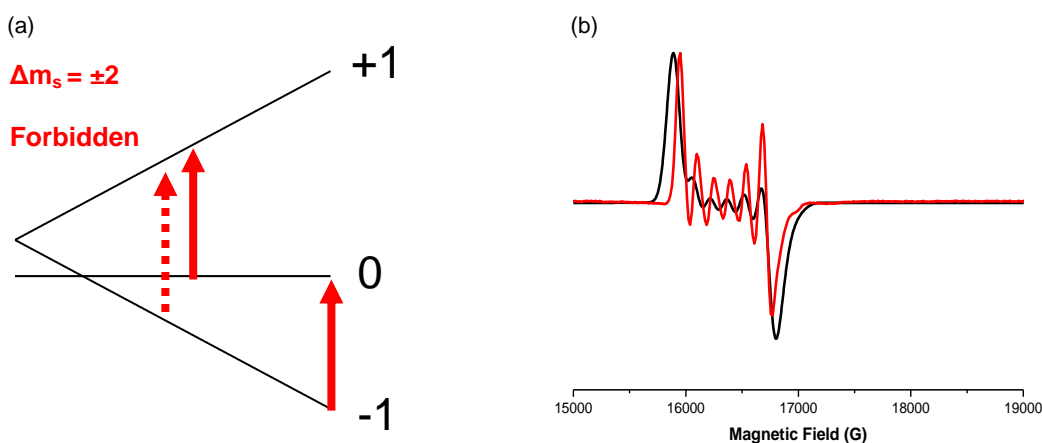
Figure III.19: (a) An energy level diagram depicting the $\Delta m_s = \pm 2$ transition which is the origin of the half field transition. (b) 5 K W-band experimental spectrum of **12** (red line) and simulation (black line). The hyperfine splitting was modelled with $A_{iso} = 0.0146 \text{ cm}^{-1}$.

The manganese (^{55}Mn I = $^5/_2$) hyperfine structure of this transition has been resolved in the 5 K to 20 K W-band spectra and is also the cause of the unusual "squaring" of the half field resonance in the Q-band spectra.

Figure III.20 compares the 5 K W-band spectra of compound **12** with the green analogue which is [H$_2$NR$_2$][Cr$_7$MnF$_8$(O$_2$C^{t}Bu)$_{16}$] (**3**). The EPR spectrum of **3** can be modelled with the following spin-Hamiltonian parameters: D = + 0.800 cm^{-1}, E = 0.085 cm^{-1}, λ = 0.106, g$_{iso}$ = 2.00 and isotropic line widths of 200 G.[7]
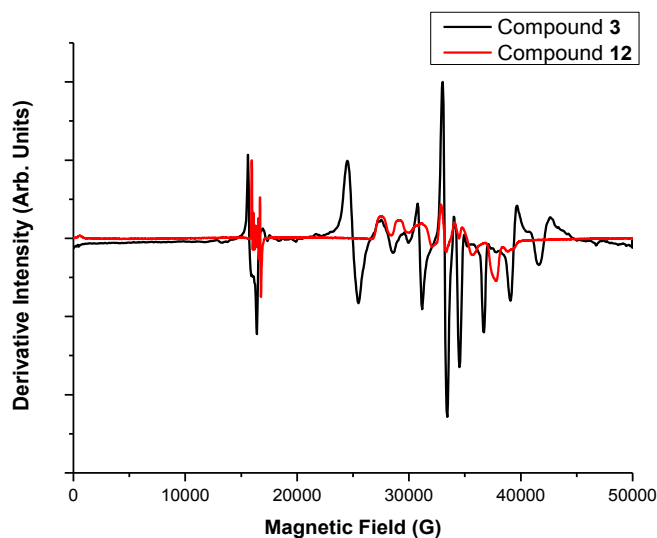
Figure III.20: EPR spectrum of a powdered polycrystalline samples of **12** (red line) and **3** (black line) at W-band frequency at 5 K.

III.3.4.1 Interpretation of the EPR Data of [$Cr_7MnF_3(Etglu)(O_2C^tBu)_{15}(phpy)$] (12)

In comparison to **3**, compound **12** has considerably narrower line widths, possibly due to the reduction of ^{19}F unresolved hyperfine interactions. Due to the narrower line widths, the $^{55}Mn^{2+}$ hyperfine splitting of the half-field resonance of compound **12** has been resolved. The hyperfine structure of the green-Cr_7M family has never been resolved. The hyperfine splitting in the 5 K W-band spectrum of **3** can be fitted with A_{iso} = 0.0147 cm^{-1}. This value is larger than a typical Mn^{2+} ion in an octahedral geometry. For example the hyperfine splitting of an Mn^{2+} ion surrounded by an octahedron of fluoride doped in a single crystal of K_2MgF_4, A_{iso} was found to be ~0.0090 cm^{-1}.[9] A crude explanation of the large hyperfine value can be found by analysis of the single ion projection coefficients, c_i, (*Appendix* VIII.2) of the eight metal ions. The c_i coefficients relate the total spin hyperfine coupling constants with those of the eight individual metal centres. The values of c_i for Cr_7Mn are shown in Table III.2. Under the

100

SEL approximation we only need to consider the projection coefficient of the $^{55}Mn^{2+}$ ion, and from this we should expect to see a hyperfine splitting of x 1.75 that of an isolated $^{55}Mn^{2+}$ ion (1.75 x 90 G = 157.5 G). This is in good agreement with the experimental value of 147 G. This assumes that the hyperfine coupling to $^{55}Mn^{2+}$ is only due to the electrons on the Mn^{2+} ion.

Table III.2: Single ion projection coefficients (c_i) and zero field splitting projection coefficient (d_i) of the ground spin state S =1 of Cr_7Mn. The vector coupling scheme used is described in Figure I.5.[10]

Metal Site	Cr(1)	Cr(2)	Cr(3)	Cr(4)	Cr(5)	Cr(6)	Cr(7)	Mn(8)
c_i	-0.525	0.45	-0.525	0.45	-0.525	0.45	-0.525	1.750
Di	0.095	0.060	0.095	0.060	0.095	0.060	0.095	2.800

Compound **12** has a smaller value of D than compound **3** the $S = 1$ ground state. Table III.2 shows the zero field splitting (d) projection coefficients of a Cr_7Mn wheel, they relate the D tensor of the effective spin state of the wheel with the D tensors of the individual metal centres. The Mn^{2+} centre has a higher d_i projection coefficient than the seven other metal centres ($D_{S=1} = 0.56 \, D_{Cr} + 2.80 \, D_{Mn}$). At the Mn^{2+} centre we have a coordination environment of MnO_3F_2N in **12** and in **3** MnO_4F_2; we have replaced one oxygen donor (pivalate) with a nitrogen donor (phenyl-pyridine) in **12**. In the spectrochemical series of ligands the N atom of a phenyl-pyridine is a stronger field ligand than the O atom of a pivalate group. A stronger field ligand has the effect of increasing Δ_{oct}; therefore Δ_{oct} will be larger in compound 5. An increase in Δ_{oct} will mean

reduced mixing with excited states via SOC (see section I.3). This means that we should expect a smaller value of D in compound **12**. Examples of the relationship between ligand field strength and the D tensor can be found in the literature.[11][12]

The E/D (λ) ratio is a measure of rhombicity. In compound **12**, λ is higher than compound **3** for both spin states. This can be rationalized as there are 5 different coordination geometries in compound **12** and just three in compound **3** The higher λ of **12** indicates lower symmetry.

III.3.5 EPR Study of $[Cr_7ZnF_3(Etglu)(O_2C^tBu)_{16}(phpy)]$

Multi-frequency (W-, Q- and X-band) powder spectra were obtained for $[Cr_7ZnF_3(Etglu)(O_2C^tBu)_{16}(phpy)]$ (**13**) giving well resolved, temperature dependent spectra below 20 K. At 5 K, there are features in the spectrum for the spin ground state of $S = {}^3/_2$ and the sharp feature at g $\approx$ 2.00 arises from the $S = {}^1/_2$ first excited state. The temperature dependence of the resonances can be used to assign the spin state that they originate from. This analysis has been done in a similar fashion to compound **12**. W-band EPR spectra measured at 5 and 10 K are shown in Figure III.21. The green star indicates a resonance which originates from an excited state and the blue stars highlight those from the ground spin state.
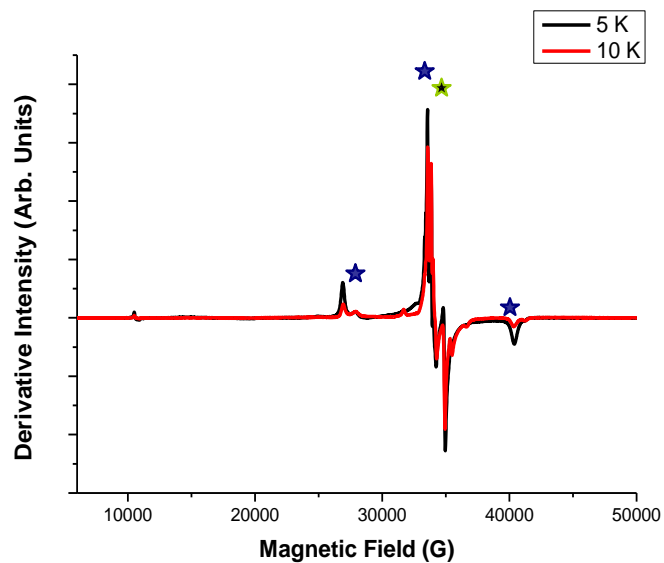
Figure III.21: EPR spectra of a polycrystalline sample of
[Cr$_7$ZnF$_3$(Etglu)(O$_2$C^{t}Bu)$_{15}$(phpy)] (**13**) at W-band frequency at 5 K and 10 K. Blue stars
indicate that the resonance originates from the ground spin state and green stars
highlight the resonances from the first excited spin state.

The resonances for the $S = {}^3/_2$ ground state can be simulated with an axially symmetric
set of g values: g_{xy} = 1.96, g_z = 1.98, with zero field splitting parameters of D = -0.329
cm^{-1} and E = 0.076 cm^{-1}. The $S = {}^1/_2$ excited state can be simulated with: g_{xy} = 1.97
and g_z =1.98 (Figure III.22).
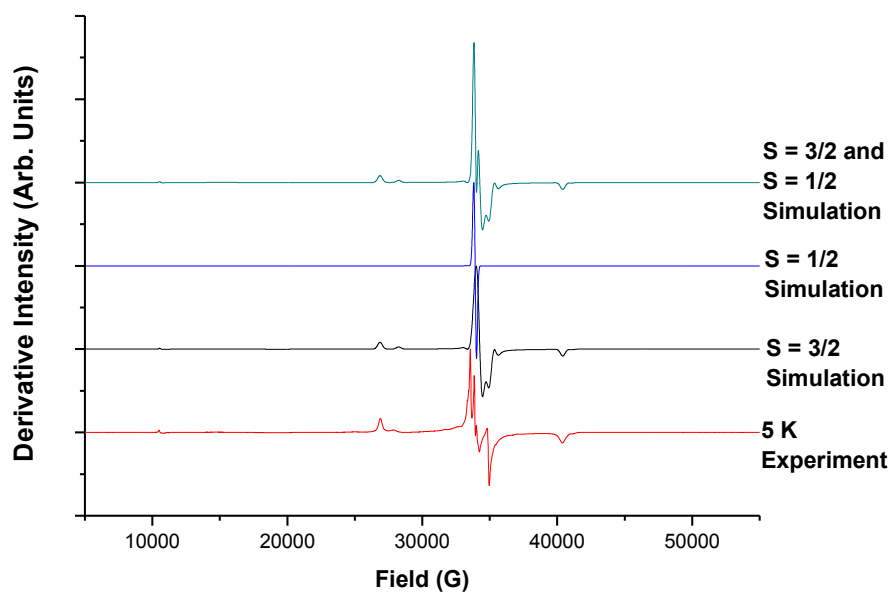
Figure III.22: 5 K W-band experimental powder EPR spectrum and simulation of [Cr$_7$ZnF$_3$(Etglu)(O$_2$C^{t}Bu)$_{15}$(phpy)] (**13**). The following spin-Hamiltonian parameters that have been used to fit the experimental spectrum; $S = {}^3/_2$: $D = -0.329$ cm^{-1}, $E = 0.076$ cm^{-1}, $g_{xy} = 1.96$ and $g_z = 1.98$. $S = {}^1/_2$: $g_{xy} = 1.97$ and $g_z = 1.98$. At frequency $\nu = 93.06387$ GHz, with Gaussian isotropic line-widths of 100 G.

Figure III.23 compares the W-band spectra of compound **13** with the green analogue [H$_2$NR$_2$][Cr$_7$ZnF$_8$(O$_2$C^{t}Bu)$_{16}$] (compound **4**).
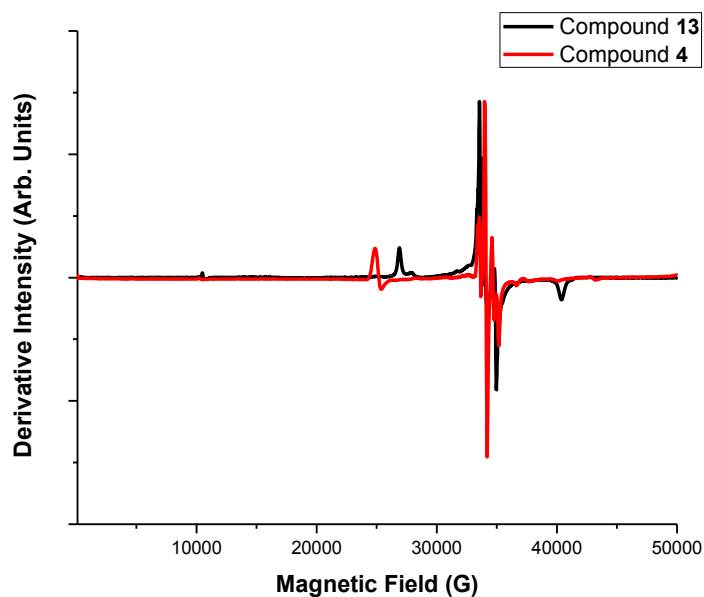
Figure III.23: EPR spectra of a powdered polycrystalline samples of **4** (red line) and **13** (black line) at W-band frequency at 5 K.

The W-band spectra of compounds **4** and **13** are considerably different from one another.

III.3.5.1 Interpretation of the EPR Data of [Cr$_7$ZnF$_3$(Etglu)(O$_2$C^{t}Bu)$_{15}$(phpy)] (13)

Compound **13** has narrower line widths than compound **4**. A possible explanation of this is analogous to that given for compounds **3** and **12**.

The value of the ground state *D* tensor is much larger in compound **4** compared to **13**. This can be explained by analysis of the coordination environment of the seven paramagnetic Cr^{3+} metal centres. The d$_i$ projection coefficients for the ground state are given in Table III.3, derived from the coupling scheme given in Figure III.10.

Table III.3: Single ion projection coefficients (c_i) and zero field splitting projection coefficient (d_i) of the ground spin state $S = {}^3/_2$ of Cr_7Zn. The vector coupling scheme used is described in Figure I.5.[10]

Metal Site	Cr(1)	Cr(2)	Cr(3)	Cr(4)	Cr(5)	Cr(6)	Cr(7)	Zn(8)
c_i	0.700	-0.600	0.700	-0.600	0.700	-0.600	0.700	0.00
D_i	0.318	0.200	0.318	0.200	0.318	0.200	0.318	0.00

The d_i projection coefficients of the seven Cr^{3+} ions take values of 0.318 and 0.200, which alternate around the wheel, the total zero field splitting arises from these individual Cr^{3+} ions. From this it can be seen that it is sensible to look towards the coordination chemistry of the Cr^{3+} metal centres. In compound **13** there are five bridging alkoxide groups, replace the bridging fluoride ligands in compound **4**. Fluoride ligands are a weaker field ligand than an alkoxide ligand, therefore **13** will have a larger value Δ_{oct} than **4**. This has been confirmed by UV/visible spectroscopy in section III.3.2. We can therefore expect there to be less SOC in compound **13**, and the *D* tensor to be smaller.

The λ value is larger for **13** and this can be explained by the larger number of different coordination environments at the metal centres in comparison to compound **4**. There is a greater deviation away from axial symmetry in **4**. This is reflected in the larger value of λ, which is close to the rhombic limit of $E/D = {}^1/_3$.

III.3.6 Single Crystal Study of [Cr$_7$NiF$_3$(Etglu)(O$_2$C^{t}Bu)$_{15}$(H$_2$O)]

A partial single crystal EPR study at K-band frequency of [Cr$_7$NiF$_3$(Etglu)(O$_2$C^{t}Bu)$_{15}$(H$_2$O)] (**14**) was attempted in order to determine the principal directions of the g-matrix in relation to the structure of the octametallic wheel. Compound **14** crystallizes in an orthorhombic $P2_12_12_1$ space group and a single crystal was indexed (see Figure III.24). In a general orientation there will be 4 magnetically inequivalent sites, collapsing to 2 when the field is along a crystal plane and 1 when the field is orientated along a crystal axis.
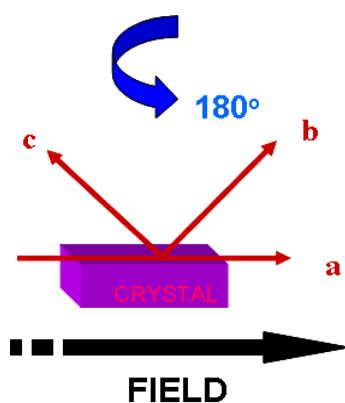
Figure III.24: A schematic diagram demonstrating how the Cr$_7$Ni orthorhombic crystal has been indexed.

Preliminary rotation experiments, performed normal to the large flat face of the plate crystal that contains the crystallographic *a* axis, show considerable anisotropy (Figure III.25). At certain orientations there is a clear structure in the spectra, with separations of *ca.* 30 G. It is possible that these features could be due to hyperfine interaction with bridging F$^-$ ions within the wheel.
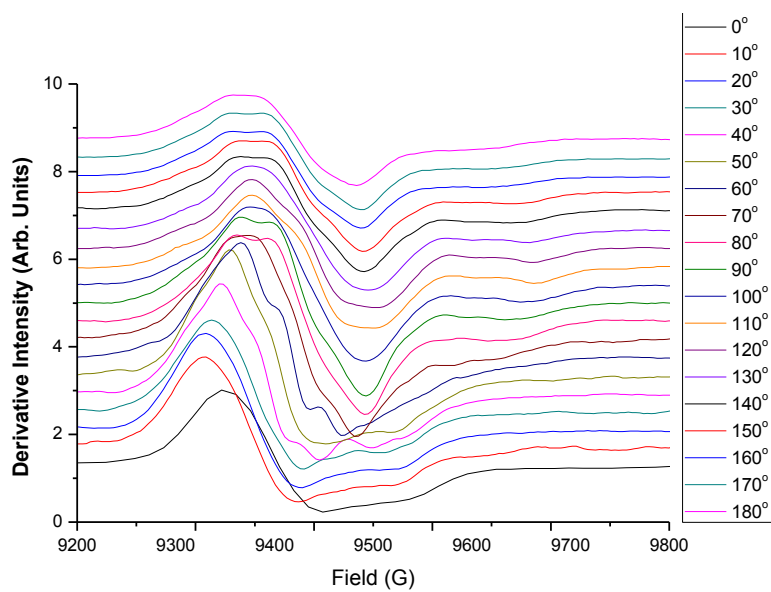
Figure III.25: EPR spectra at K-band frequency of a orthorhombic single crystal of

[$Cr_7NiF_3(Etglu)(O_2C^tBu)_{15}(H_2O)$] (**14**) at 10 K.

This study is incomplete, as spectra from two further, mutually orthogonal planes of rotation will be required in order to perform the required analysis using the method of Schonland.[13] The resolution is insufficient to resolve the magnetically inequivalent sites, thus making analysis impossible.

III.4 Conclusions

The spin-Hamiltonian parameters which have been determined for the ground states of the purple-Cr_7M and green-Cr_7M wheels are summarized in Table III.4.

Table III.4: The spin-Hamiltonian parameters of the ground states of the green and purple Cr_7M wheels.

Compound	D (cm^{-1})	E (cm^{-1})	$\lambda = E/D$	g-value	Line width (G)
(**11**) Purple-Cr_7Ni	N/A	N/A	N/A	$g_{xy} = 1.84$ $g_z = 1.78$	65
(**2**) Green-Cr_7Ni	N/A	N/A	N/A	$g_{xy} = 1.84$ $g_z = 1.74$	100
(**12**) Purple-Cr_7Mn	-0.547	0.090	0.165	$g_{iso} = 2.01$	100
(**3**) Green-Cr_7Mn	+0.800	0.085	0.106	$g_{iso} = 2.00$	200
(**13**) Purple-Cr_7Zn	-0.329	0.076	0.231	$g_{xy} = 1.96$ $g_z = 1.98$	100
(**4**) Green-Cr_7Zn	+0.410	0.041	0.106	$g_{iso} = 2.00$	200

Magnetic and EPR measurements have confirmed that the purple wheels have the same ground spin states as the green wheels. Hence an equivalent coupling scheme can be used for both the green and purple wheels. The purple wheels have a larger gap between the ground state and the first excited state in comparison to the green

wheel family. For the purple wheel family this gap is ~13.5 cm^{-1} for **11**, ~13.7 cm^{-1} for **12** and ~8.2 cm^{-1} for **13**. For the green wheel family, there is a gap of ~10.0 cm^{-1} for **2**, ~12.9 cm^{-1} for **3** and ~7.0 cm^{-1} for **4**. The J_{CrCr}-values are larger for the purple wheel family. There is a 35% increase in J_{CrCr}-values from 5.90 cm^{-1} to 8.00 cm^{-1}. This must mean that there is a better exchange pathway *via* bridging alkoxide groups compared to bridging fluoride ions. The ground states of the purple wheel family have smaller *D* values than the green wheel family. This is due to crystal field effects. The ground state of the purple wheel family also has larger λ values; this is due to the purple wheels being less symmetrical.

The purple wheel family has narrower EPR line widths than the green wheel family; this is partly due to the larger ground state- to excited state energy gap. The narrower line widths can also be attributed to a reduction in the number of bridging $^{19}F^{-}$ ions, which may be a source of unresolved hyperfine interactions. It is likely that longer spin relaxation times will be measured for the purple wheel family due to the larger ground state to excited state energy gap and the reduction in $^{19}F^{-}$ hyperfine. The narrow line widths of **11** will allow for more accurate determination of the interaction between linked dimers of **11** (see chapter IV).

III.5 Reference

1. G. A. Timco, E. J. L. McInnes, R. J. Pritchard, F. Tuna and R. E. P. Winpenny, *Angew. Chem. Int. Ed.*, 2008, **47**, 9681-9684.

2. A. Candini, G. Lorusso, F. Troiani, A. Ghirri, S. Carretta, P. Santini, G. Amoretti, C. Muryn, F. Tuna, G. Timco, E. J. L. McInnes, R. E. P. Winpenny, W. Wernsdorfer and M. Affronte, *Phys. Rev. Lett.*, **104**, 037203.

3. S. Piligkos, H. Weihe, E. Bill, F. Neese, H. El Mkami, G. M. Smith, D. Collison, G. Rajaraman, G. A. Timco, R. E. P. Winpenny and E. J. L. McInnes, *Chem. Eur. J.*, 2009, **15**, 3152-3167.

4. R. Caciuffo, T. Guidi, G. Amoretti, S. Carretta, E. Liviotti, P. Santini, C. Mondelli, G. Timco, C. A. Muryn and R. E. P. Winpenny, *Phys. Rev. B.*, 2005, **71**, 174407.

5. J. J. Borrás-Almenar, J. M. Clemente-Juan, E. Coronado and B. S. Tsukerblat, *J. Comput. Chem.*, 2001, **22**, 985-991.

6. R. M. Macfarlane, *J. Chem. Phys.*, 1963, **39**, 3118-3126.

7. S. Piligkos, Ph.D. Thesis, The University of Manchester (Manchester, UK), 2004.

8. F. E. Mabbs and D. Collison, *Electron Paramagnetic Resonance of d Transition Metal Compounds*, Elsevier, Amsterdam, 1992.

9. S. Ogawa, *J. Phys. Soc. Jpn.*, 1960, **15**, 1475.

10. A. Bencini and D. Gatteschi, *EPR of Exchanged Coupled System*, Springer-Verlag, Berlin, 1989.

11. E. Pedersen and S. Kallesoe, *Inorg. Chem.*, 1974, **14**, 85-88.

12. H. I. Karunadasa, K. D. Arquero, L. A. Berben and J. R. Long, *Inorg. Chem.*, **49**, 4738-4740.

13. D. S. Schonland, *Proceedings of the Physical Society*, 1959, 788.

IV Tuning the Interaction between Linked Dimers of Purple-Cr$_7$M Wheels

IV.1 Introduction

Recent times have seen the advent of several powerful quantum algorithms.[1-3] This has sparked a considerable research effort into development of molecular-scale devices for uses in quantum information processing (QIP).[4-8] It has been proposed that linked dimers of $[Cr_7NiF_3(Etglu)(O_2C^tBu)_{15}(Et_2O)]$ (purple-Cr_7Ni) may have applications in QIP.[9, 10]

This introduction will briefly discuss some of the concepts in QIP that are relevant to the implementation of the purple-{Cr_7Ni} wheels in devices. No attempt has been made at an in depth discussion, as there are several good, accessible, introductory books available on the subject.[11, 12] In classical computing, a bit is a basic unit of information and can only have one of the two states: 0 or 1. A quantum bit (qubit) is a unit of quantum information, which consists of a two-level quantum mechanical system, where the two states are conventionally written as $|0\rangle$ and $|1\rangle$, which corresponds to the 0 or 1 state of a classical bit.

There are two important differences between a qubit and a classical bit. Firstly a qubit can exist as a linear combination of states, which are known as superpositions. Secondly, multiple qubits can exhibit quantum entanglement, which is a quantum phenomenon in which the states of two or more quantum systems cannot be described independently from one another. For QIP to be implemented, there must controlled generation of quantum entanglement between qubits. A result of this phenomenon is that the amount of information that can be contained in an entangled state of n qubits grows exponentially with n, and not linearly as in the case of classical bits. The combination of these two properties, linear superposition and entanglement, enable the

113

possibility of performing a large number of operations in parallel. This would enable Shor's[2] and Grover's[1] algorithms to be implemented. In 2003 Loss proposed that QIP could be implemented with antiferromagnetically coupled molecular spin clusters with an effective spin state of $S = {}^1\!/_2$.[13] His proposal was that two of these $S = {}^1\!/_2$ clusters could be joined together to form a two-qubit gate, where between the two halves of the dimer there is a weak and switchable interaction (J_*). A schematic diagram of this proposal can be seen in Figure IV.1. The inter-cluster exchange interaction J_* must be much weaker than the intra-cluster exchange interaction J. The Manchester Magnetism group is working towards finding a physical realisation of this proposal.
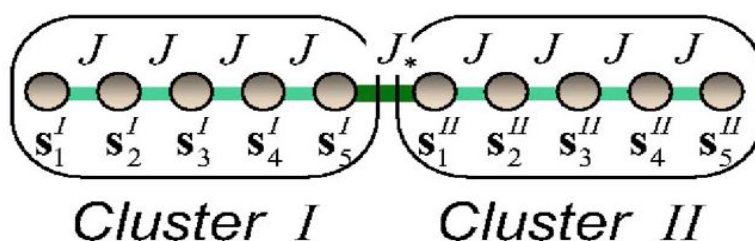
Figure IV.1 A picture of the proposed two-qubit gate taken from reference[13].

There are several examples in the literature of linking discrete polymetallic cages into larger supramolecular structures by coordination chemistry. An example of this is the work of Yamashita's group where they have linked together {Mn$_4$} single molecule magnets into 2D and polymer networks. The magnetic properties of the polymers are controlled by the choice of organic linker.[14, 15] There is only one example of a dimer of clusters. Hill and co-workers conducted EPR studies on two dimers of the SMMs [Mn$_4$O$_3$Cl$_4$(O$_2$CEt)$_3$(py)$_3$]$_2$·R (R = MeCN or C$_6$H$_{14}$).[16] These two dimers are formed by

crystallization from different solvents and the dimer is formed only via H-bonding. Therefore the chemistry of these dimers is not easily controllable.

In contrast, the chemistry of purple-(Cr$_7$Ni) wheels is highly controllable allowing covalent linking of the clusters. Purple-(Cr$_7$Ni) wheels have a rich coordination chemistry and are robust building blocks. We are able to engineer weak magnetic couplings between purple-Cr$_7$Ni wheels by relatively simple synthetic chemistry. Purple-(Cr$_7$Ni) wheels have been identified as being well suited to applications in QIP as they have a suitable energy level structure. The seven chromium atoms and the single Ni are antiferromagnetically coupled resulting in an effective spin-$\frac{1}{2}$ system at sufficiently low temperatures.[10] They have few proximal F$^-$ ions (I = $\frac{1}{2}$) and as a result long decoherence times have been measured for [Cr$_7$NiF$_3$(Etglu)(O$_2$C^{t}Bu)$_{15}$(phpy)] (**11**) in comparison to [H$_2$NMe$_2$][Cr$_7$NiF$_8$(O$_2$C^{t}Bu)$_{16}$] (**5**).[17] The magnitude of the exchange coupling *J* between the two wheels can be controlled by choice of the N-donor linker.

IV.2 The Coordination Chemistry of the Purple-Cr$_7$M Wheels

As described in chapter three, at the heterometal site of a purple-{Cr$_7$Ni} wheel, there is a labile ligand which can be a water molecule, acetonitrile or diethyl ether. This labile ligand can be substituted for a variety of organic ligands. It is through this functionality that the single purple-(Cr$_7$Ni) wheels can be linked together into oligomers through the use of diimines.[10] The organic linkers which have been used are shown in Figure IV.2.

(15) 4,4'-bpy   **(18)** pyCHCHPy

(16) pyN=Npy   **(19)** pyCH₂CH₂py

(17) pyCCpy   **(20)** pyCH(OH)CH(OH)Py
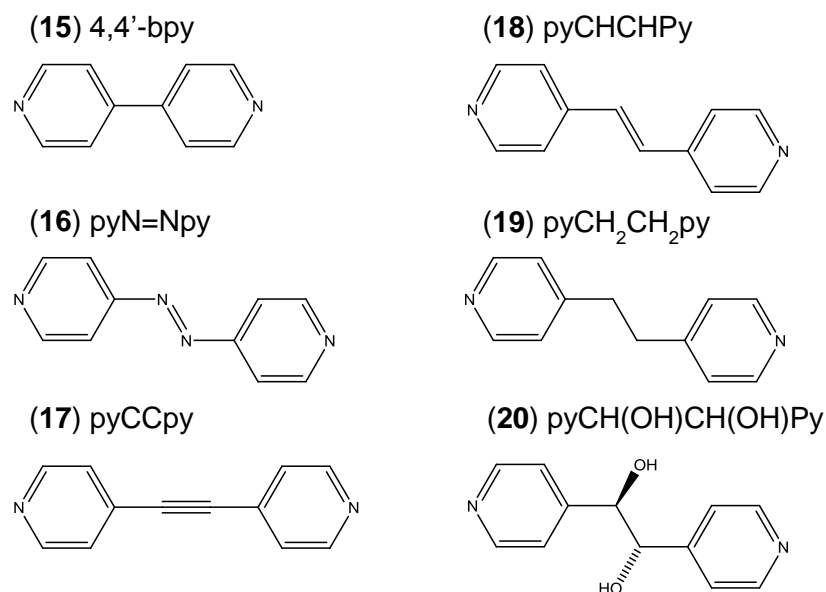
Figure IV.2: Organic Linkers: 4,4'-bipyridine (**15**), 4,4'-azopyridine (**16**), 1,2-di(4-pyridyl)ethyne (**17**), *trans*-(1,2)-di(4-pyridyl)ethene (**18**), 1,2-bis(4-pyridyl)ethane (**19**) and 1,2-ethanediol-1,2-di-4-pyridine (**20**).

Organic linkers of varying length have been selected, for example 4,4'-bipyridine is shorter than *trans*-(1,2)-di(4-pyridyl)ethane. This is to test if there is a relationship between D and the length of organic linker. The series contains unsaturated and saturated molecules, this to test the effect of conjugation on magnetic superexchange. 1,2-bis(4-pyridyl)ethane, *trans*-(1,2)-di(4-pyridyl)ethene and 1,2-di(4-pyridyl)ethyne have been selected because they contain single, double and triple bonds respectively. This is to test if the strength of interaction is dependent on the hybridisation of the carbon-carbon bonds. 4,4'-azopyridine and *trans*-(1,2)-di(4-pyridyl)ethene are isoelectronic, they have been chosen to test if there is more efficient magnetic superexchange between nitrogen or carbon atoms. Figure IV.3 is a reaction scheme depicting the coordination chemistry of the purple Cr_7Ni wheels. In this study EPR spectroscopy has been used to determine electronic interaction between the two halves of a series of $(Cr_7M)_2$-L dimers.
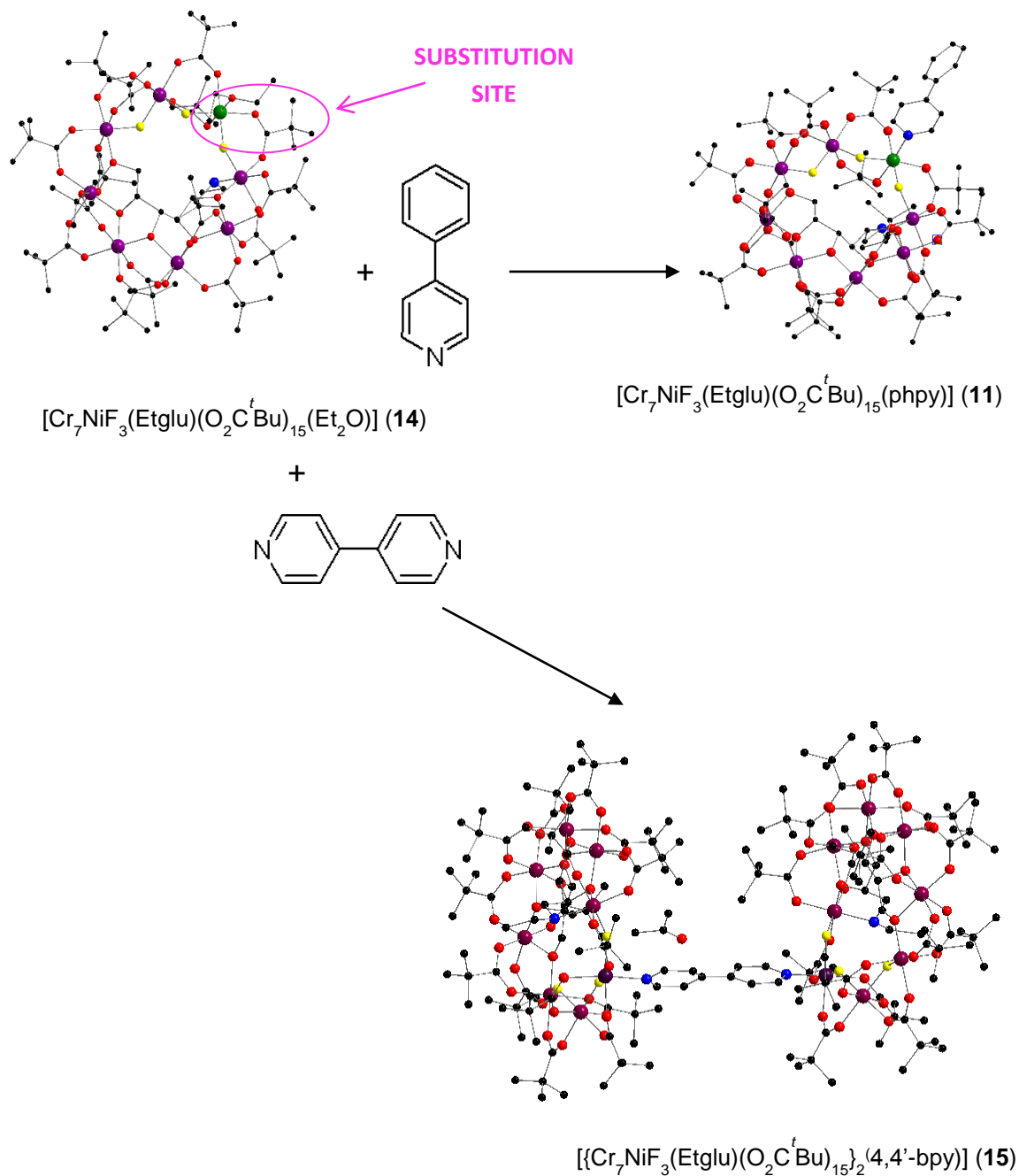
Figure IV.3: Reaction scheme depicting the coordination chemistry of purple-Cr$_7$Ni wheels. All hydrogen atoms have been removed for clarity.

The synthesis has been designed so that [Cr$_7$NiF$_3$(Etglu)(O$_2$C^{t}Bu)$_{15}$(phpy)] (**11**) approximately equals one half of the dimeric [{Cr$_7$NiF$_3$(Etglu)(O$_2$C^{t}Bu)$_{15}$}$_2$(4,4'-bpy)]

(**15**). Figure IV.4 shows Q-band EPR spectra of powdered samples of [Cr_7NiF_3(Etglu)(O_2C^tBu)$_{15}$(Et_2O)] (**14**) and **11**. The EPR spectrum of **14** shows an asymmetric single resonance at 4 K due to its $S_{eff} = {}^1/_2$ ground spin state. When the solvent molecule is substituted for 4-phenylpyridine, a spin doublet is still observed but with increased g-anisotropy. Compound **11** can be modelled with an axially symmetric set of g-values, $g_{xy} = 1.84$ and $g_z = 1.78$.
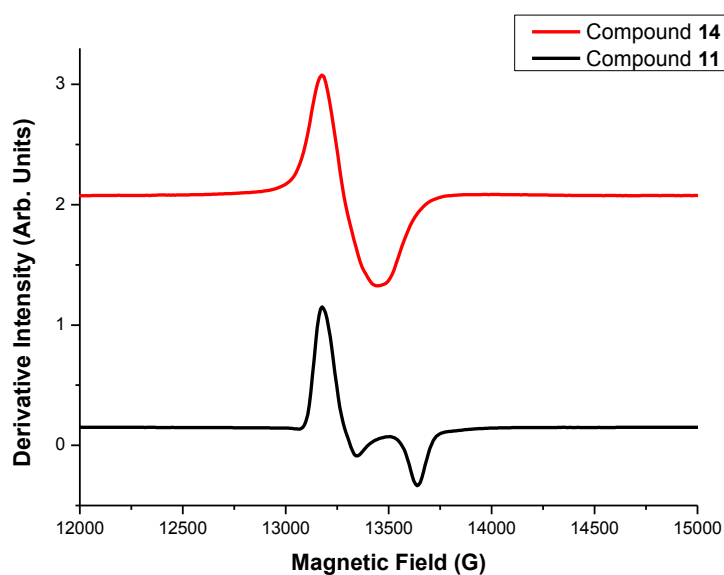
Figure IV.4: EPR spectra of powdered sample of compounds [Cr_7NiF_3(Etglu)(O_2C^tBu)$_{15}$(Et_2O)] (**14**) and [Cr_7NiF_3(Etglu)(O_2C^tBu)$_{15}$(phpy)] (**11**) at 4 K at Q-band frequency.

When 4,4'-bipyridine is used in the substitution reaction, compound **15** is formed where the two wheels are coupled through the 4,4'-bipyridine. When trans-(1,2)-di(4-pyridyl)ethene is used in a substitution reaction with **11** [{Cr_7NiF_3(Etglu)(O_2C^tBu)$_{15}$}$_2$](pyCHCHpy)] (**18**) is formed. A spin triplet is observed for both **15** and **18** at low temperatures, which proves that the wheels are also coupled electronically. Figure IV.5 shows the 5 K Q-band frequency EPR spectra and simulations of compounds **11**, **15** and **18**.
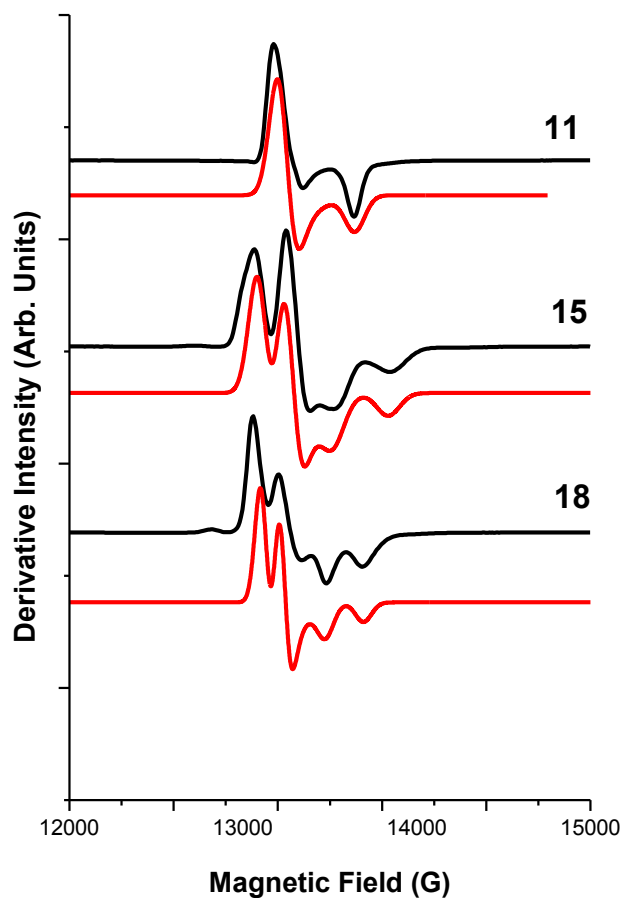
Figure IV.5: EPR spectra at Q-band frequency of compounds
[Cr$_7$NiF$_3$(Etglu)(O$_2$C^{t}Bu)$_{15}$(phpy)] (**11**), [{Cr$_7$NiF$_3$(Etglu)(O$_2$C^{t}Bu)$_{15}$}$_2$(4,4'-bpy)] (**15**) and
[{Cr$_7$NiF$_3$(Etglu)(O$_2$C^{t}Bu)$_{15}$}$_2$](pyCHCHpy)] (**18**), the black lines are experimental spectra
and the red lines are simulations.

The powder EPR spectrum of **15** can be modelled as $S = 1$ with an axially symmetric

set of g-values, which deviate slightly from those of **11**, and a small positive zero-field

splitting parameter: $D = + 0.013$ cm^{-1}, $g_{xy} = 1.84$ and $g_z = 1.77$. The EPR spectrum of

18 can be fitted with: $D = + 0.009$ cm^{-1}, $g_{xy} = 1.84$ and $g_z = 1.77$. Compound **15** has a

larger D value than **18**, this implies that there is stronger exchange between the wheels

when there is a shorter organic linker. This indicates that the interaction between the

wheels in a dimer can be tuned. This chapter will investigate further whether the strength of the exchange interaction between a dimer of purple-{Cr$_7$Ni} wheels can be controlled by the choice of bridging ligand, and what factors will afford a stronger or weaker interaction.

IV.3 Generation of a Spin Triplet within Di-ring Cluster 15

The interaction between the two molecular wheels in dimer **15** is directly routed through the nickel centres *via* the organic linker. Specific heat and magnetic measurements performed at 30mK by W. Wernsdorfer and co-workers have characterized this interaction.[9] They have found that for **15** the wheel-wheel interaction is weakly antiferromagnetic, giving an $S = 0$ spin ground state (which is EPR inactive) and an $S = 1$ excited state (which is EPR active). There is very small gap between the singlet and triplet state ($\approx$ 0.04 cm^{-1}) therefore the triplet excited state is thermally accessible at the liquid helium temperature (4.2 K) at which EPR measurements are performed. The microscopic intermolecular coupling between the two wheels (named A and B) of **15** was modelled with the following Hamiltonian:

$$H_{AB} = J' s_8^A \cdot s_8^B$$

Equation IV.1

It was reported that the wheel-wheel J-value of **15** was $\leq$ 0.1 cm^{-1}. As a wheel-wheel J-value of this magnitude is too small to be measured by following VT intensity of triplet transitions in the EPR. However, the triplet ZFS is reporting on the anisotropic part of

the exchange and can therefore be used as a simple gauge of the interaction without the need for mK micro-squid measurements.

IV.4 Results and Discussion

IV.4.1 EPR Study of [{Cr$_7$NiF$_3$(Etglu)(O$_2$C^{t}Bu)$_{15}$}$_2$(pyN=Npy)]

[{Cr$_7$NiF$_3$(Etglu)(O$_2$C^{t}Bu)$_{15}$}$_2$(pyN=Npy)] (**16**) is a dimer of Cr$_7$Ni molecular wheels. The two Cr$_7$Ni wheels are linked via 4,4'-azopyridine, which coordinates to the Ni^{2+} site of each wheel. The structure of **16** in the crystal is shown in Figure IV.7.
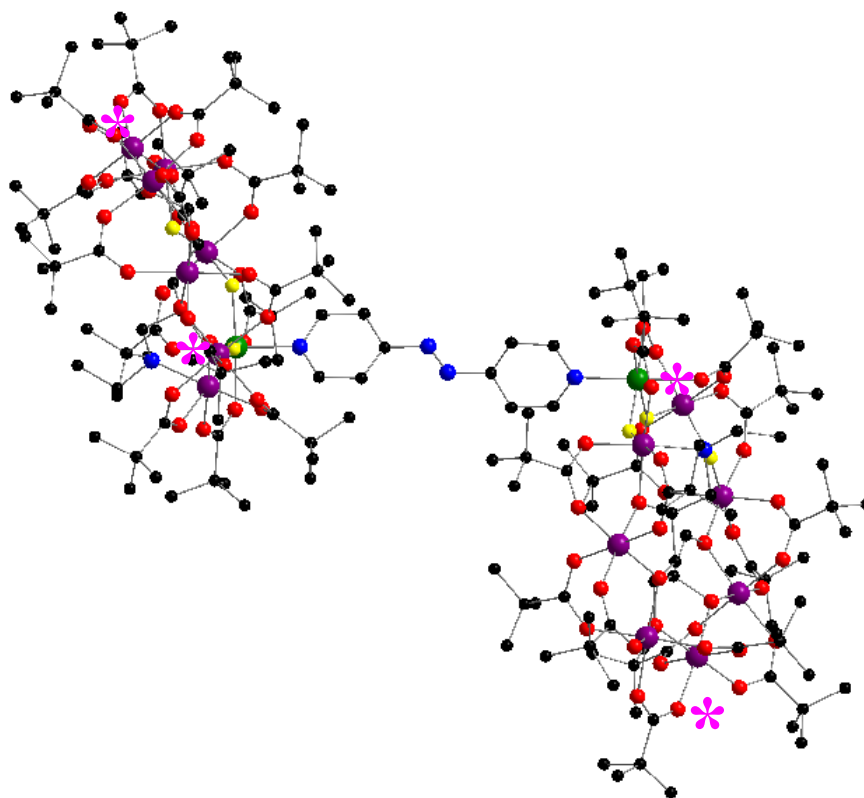
Figure IV.6: [{Cr$_7$NiF$_3$(Etglu)(O$_2$C^{t}Bu)$_{15}$}$_2$(pyN=Npy)] (**16**). Colours; Cr atoms: purple; Ni atom: green; C atoms: black; F atoms: yellow; N atoms: blue; O atoms: red. All H atoms have been removed for clarity. The pink asterisked atoms have been used to define a Cr···Ni···Ni···Cr torsion angle.

The two wheels of the dimer are in a staggered conformation to one another. To quantify the conformation of the two wheels and to aid comparison to other members of the wheel dimers family, a mean plane has been calculated through the eight metal centres in each of the purple-(Cr_7Ni) wheels in the dimer. The angle between the two planes was found to be 21.37° for **16** (Figure IV.8). An alternative measure is the Cr···Ni···Ni···Cr torsion angle as defined in Figure IV.7. The torsion angle for **16** is 130.74°. A through bond measurement between Ni centres has been made to determine if there is a relationship between the length of the organic linker and the magnitude of the D tensor of the $S = 1$ spin state. For **16** this measurement is 16.33 Å. The through-space distance between Ni^{2+} centres is 13.12 Å for **16**.
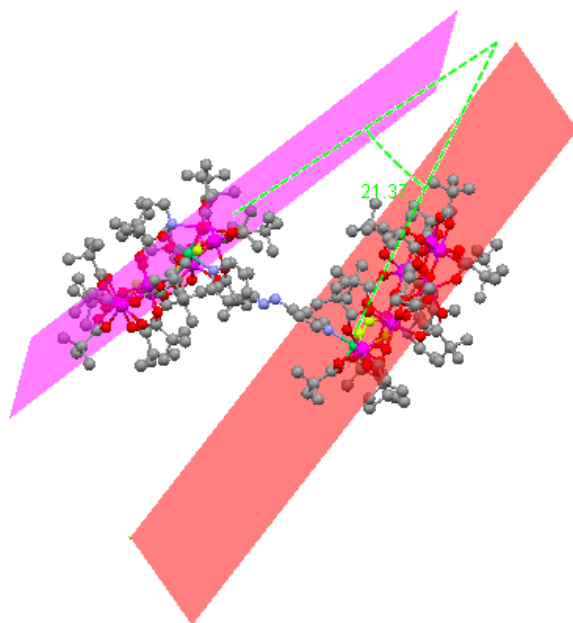
Figure IV.7: Angle between the mean planes of each wheel in
[{Cr_7NiF_3(Etglu)(O_2C^tBu)$_{15}$}$_2$(pyN=Npy)] (**16**).

EPR spectra have been obtained of powdered samples of **16** at Q-, S- and X-band frequencies (figures IV.9, IV.10 and IV.11).
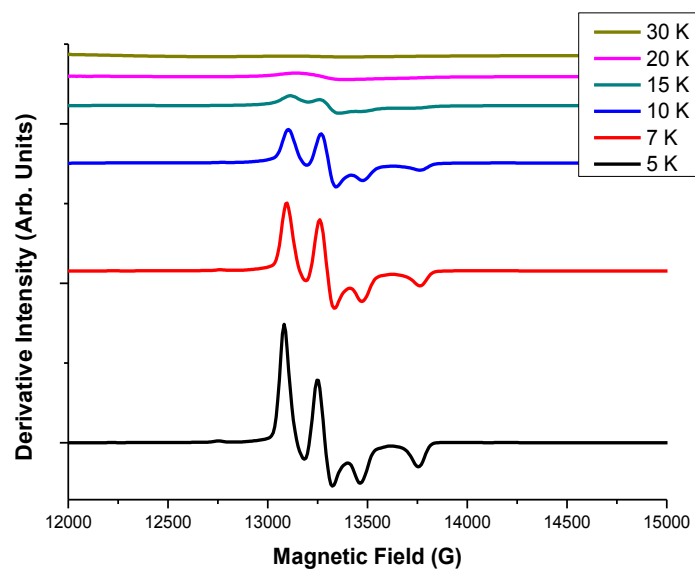
Figure IV.8: Variable temperature EPR spectra of a powdered sample of [{Cr$_7$NiF$_3$(Etglu)(O$_2$C^{t}Bu)$_{15}$}$_2$(pyN=Npy)] (**16**) at Q-band frequency.
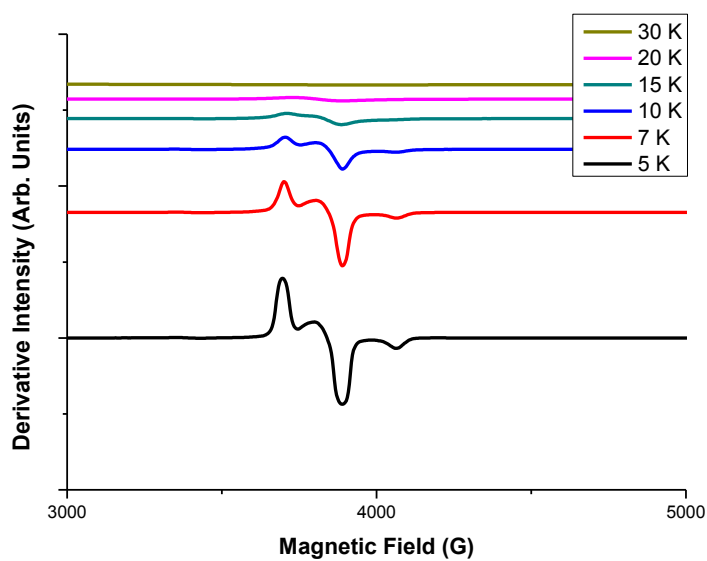
Figure IV.9: Variable temperature EPR spectra of a powdered sample of [{Cr$_7$NiF$_3$(Etglu)(O$_2$C^{t}Bu)$_{15}$}$_2$(pyN=Npy)] (**16**) at X-band frequency.
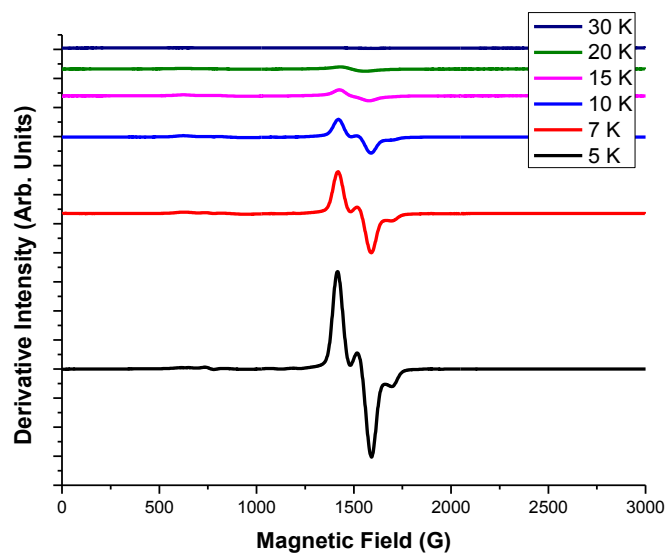
Figure IV.10: Variable temperature EPR spectra of a powdered sample of [{Cr$_7$NiF$_3$(Etglu)(O$_2$C^{t}Bu)$_{15}$}$_2$(pyN=Npy)] (**16**) at S-band frequency.

Below 20 K at S-, X- and Q-band frequencies the EPR resonances are well resolved and are clearly due to an $S = 1$ spin state. Above 20 K the spectra become much broader and single isotropic resonances are observed due to population of further excited states. Figures IV.12 and IV.13 show 5 K Q-band and S-band experimental EPR spectra of **16** and simulations.
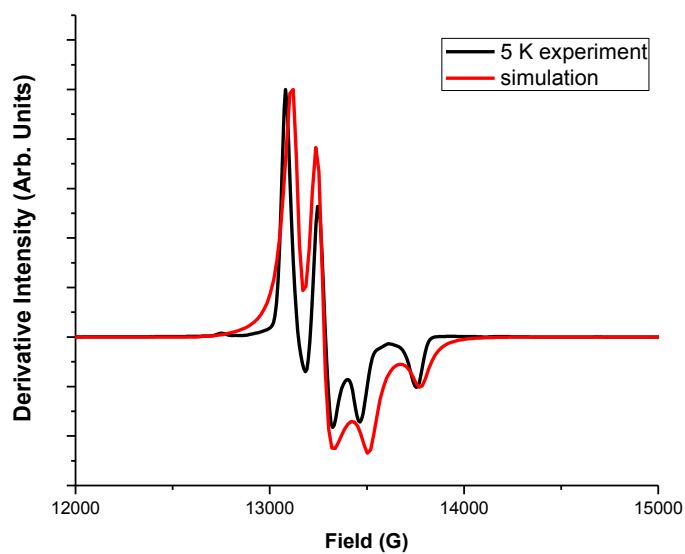
Figure IV.11: EPR spectrum (black line) and simulation (red line) of a powdered sample of compound [{Cr$_7$NiF$_3$(Etglu)(O$_2$C^{t}Bu)$_{15}$}$_2$(pyN=Npy)] (**16**) at Q-band frequencies.
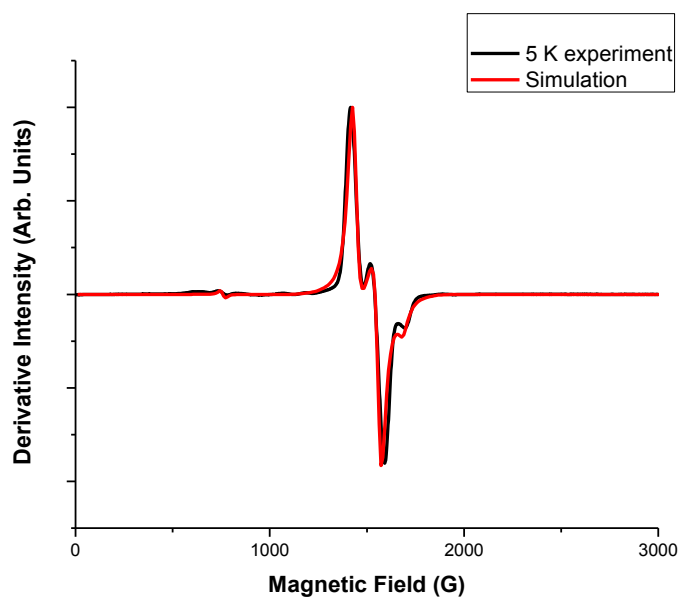
Figure IV.12: EPR spectrum (black line) and simulation (red line) of a powdered sample of compound [{Cr$_7$NiF$_3$(Etglu)(O$_2$C^{t}Bu)$_{15}$}$_2$(pyN=Npy)] (**16**) at S-band frequencies.

.

All of the $(Cr_7Ni)_2$ wheel dimers in this section have been modelled with Equation II.2, which is a SEL spin-Hamiltonian for a total spin $S = 1$. The following spin-Hamiltonian parameters have been used to fit the experimental spectra: $D = + 0.011$ cm^{-1}, $g_{xy} = 1.84$ and $g_z = 1.78$. The simulation is sensitive to the sign of D and has been found to be positive.

IV.4.2 EPR Study of [{Cr$_7$NiF$_3$(Etglu)(O$_2$C^{t}Bu)$_{15}$}$_2$](pyCCpy)]

Figure IV.14 shows a crystal structure of [{Cr$_7$NiF$_3$(Etglu)(O$_2$C^{t}Bu)$_{15}$}$_2$](pyCCpy)] (**17**). The two wheels are linked by 1,2-di(4-pyridyl)ethyne.
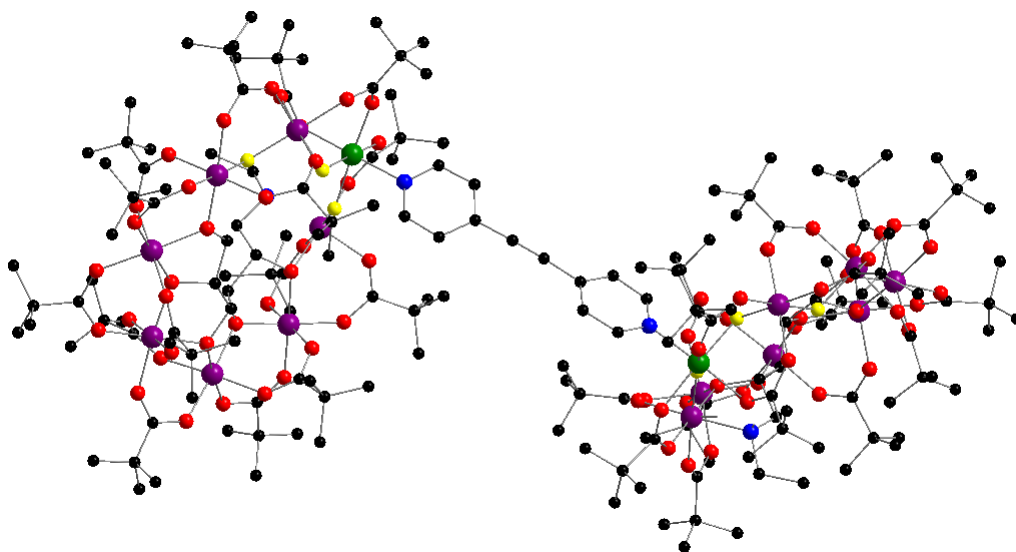
Figure IV.13: [{Cr$_7$NiF$_3$(Etglu)(O$_2$C^{t}Bu)$_{15}$}$_2$](pyCCpy)] (**17**) Colours are the same as before. All H atoms have been removed for clarity.

The torsion angle, calculated in a similar fashion to **16**, is 135.30°. There is an angle of 21.37° between the two planes of the metal centres and a through-bond distance

between Ni atoms of 16.34 Å. There is a through-space Ni^{2+} to Ni^{2+} distance of 13.68 Å. EPR spectra of powdered samples of **17** were performed at Q-, X- and S-band frequencies (Figure IV.14, IV.15 and IV.16).
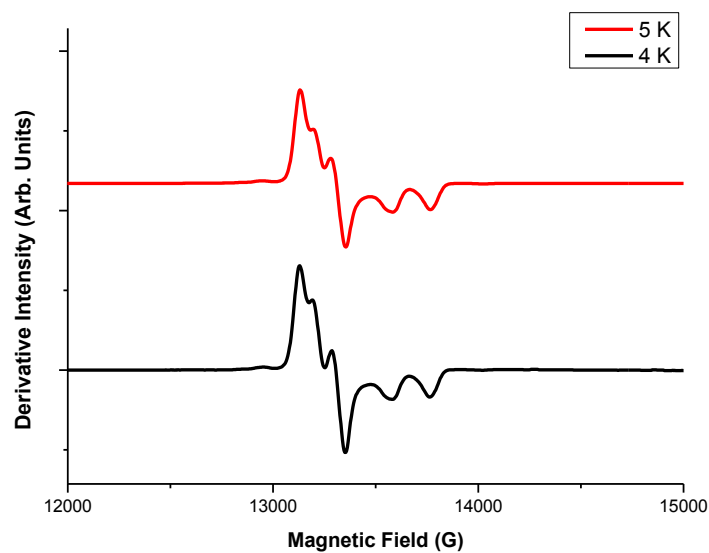
Figure IV.14: Variable temperature EPR spectra of a powdered sample of [{Cr_7NiF_3(Etglu)(O_2C^tBu)$_{15}$}$_2$(pyCCpy)] (**17**) at Q-band frequency.
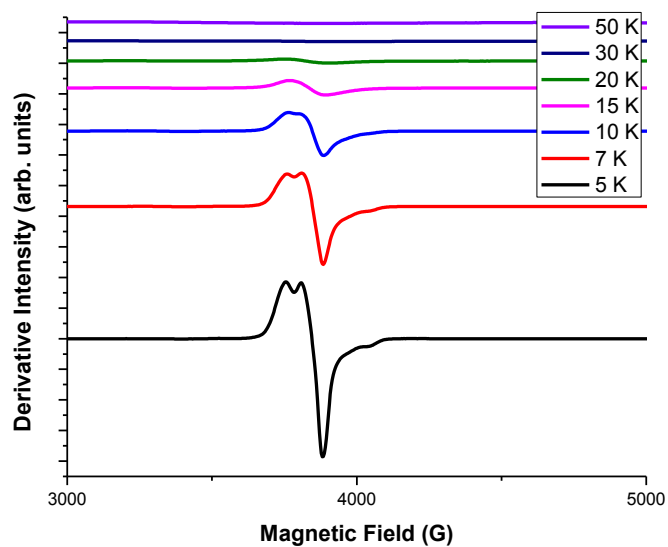
Figure IV.15: Variable temperature EPR spectra of a powdered sample of [{Cr_7NiF_3(Etglu)(O_2C^tBu)$_{15}$}$_2$(pyCCpy)] (**17**) at X-band frequency.
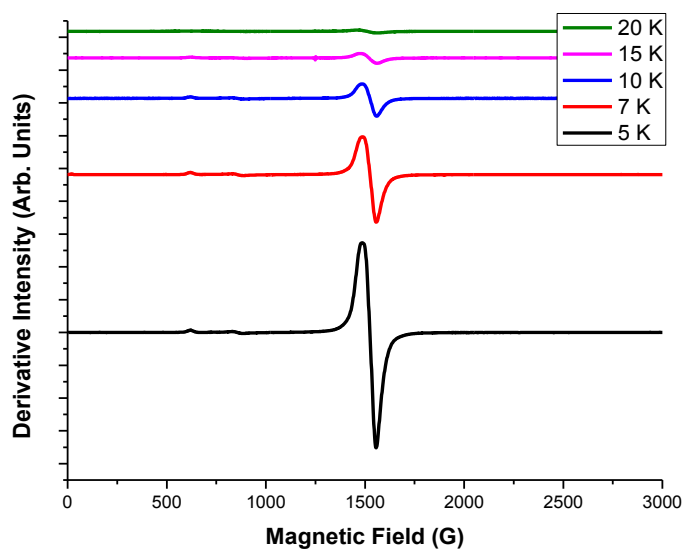
Figure IV.16: Variable temperature EPR spectra of a powdered sample of [{Cr$_7$NiF$_3$(Etglu)(O$_2$C^{t}Bu)$_{15}$}$_2$(pyCCpy)] (**17**), at S-band frequency.

At Q-band frequency the EPR spectrum is clearly a spin triplet. At X-band frequency the spin triplet is less well resolved and at S-band (the lowest frequency) the fine structure is not resolved. This is due the *D* tensor of the spin triplet being smaller than that was determined for **15** and **16**. The powder EPR spectra can be modelled with: *D* = + 0.008 cm^{-1}, g$_{xy}$ = 1.84 and g$_z$ = 1.77. The simulations of **17** at Q- and S-band frequencies are shown in Figure IV.17 and IV.18 respectively.
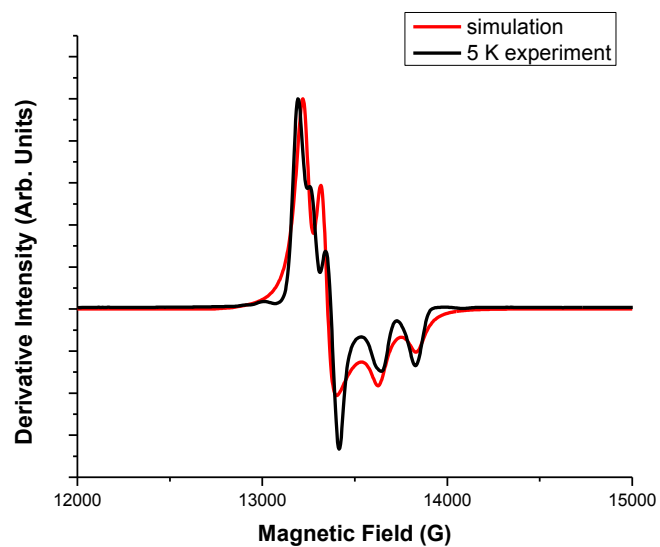
Figure IV.17: EPR spectrum (black line) and simulation (red line) of a powdered sample of compound [{Cr$_7$NiF$_3$(Etglu)(O$_2$C^{t}Bu)$_{15}$}$_2$(pyCCpy)] (**17**) at Q-band frequency.
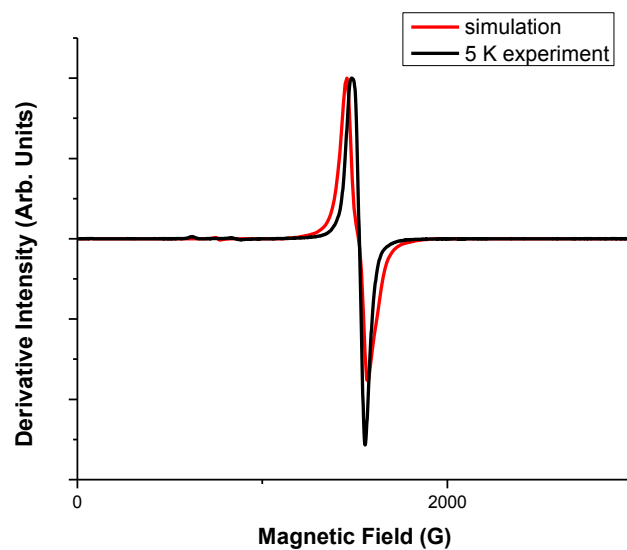
Figure IV.18: EPR spectrum (black line) and simulation (red line) of a powdered sample of compound [{Cr$_7$NiF$_3$(Etglu)(O$_2$C^{t}Bu)$_{15}$}$_2$(pyCCpy)] (**17**) at S-band frequency.

IV.4.3 EPR Study of [{Cr$_7$NiF$_3$(Etglu)(O$_2$C^{t}Bu)$_{15}$ }$_2$(pyCH$_2$CH$_2$py)]

The next purple-(Cr$_7$Ni) dimer in the series is [{Cr$_7$NiF$_3$(Etglu)(O$_2$C^{t}Bu)$_{15}$}$_2$(pyCH$_2$CH$_2$py)] (**19**)**.** The two wheels of the dimer are linked together through 1,2-bis(4-pyridyl)ethane. The two wheels are in a staggered conformation to one another. The torsion angle was found to be 133.59° for **19**, the through-bond Ni^{2+} to Ni^{2+} distance is 16.59 Å, the through-space Ni^{2+} to Ni^{2+} distance is 12.89 Å and the angle between the two planes of the metal centres is 33.06°. The structure of **19** in the crystal is shown in Figure IV.19.
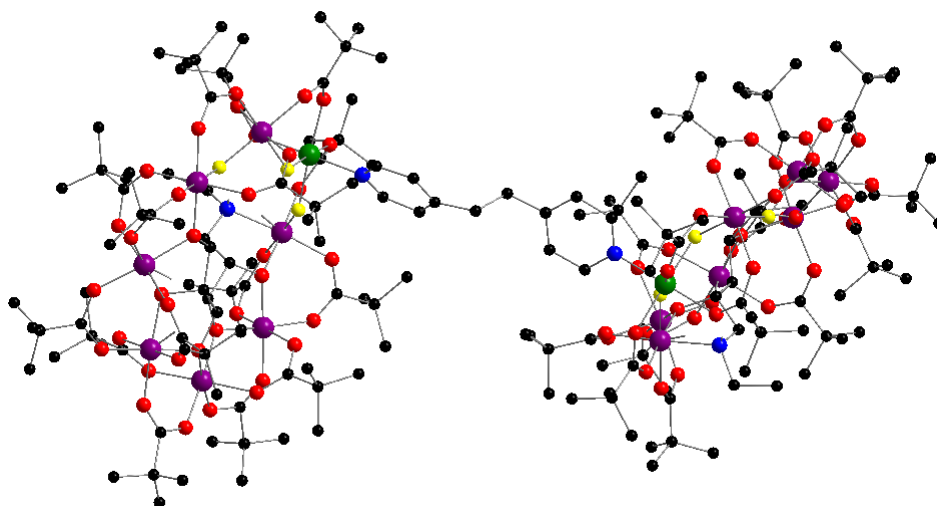
Figure IV.19: [{Cr$_7$NiF$_3$(Etglu)(O$_2$C^{t}Bu)$_{15}$ }$_2$(pyCH$_2$CH$_2$py)] (**19**).
Colours: same as before. All H atoms have been removed for clarity.

EPR spectra of a powdered sample of **19** were obtained at Q-.S- and X-band frequencies (Figures IV.20, IV.21 and IV.22 respectively).
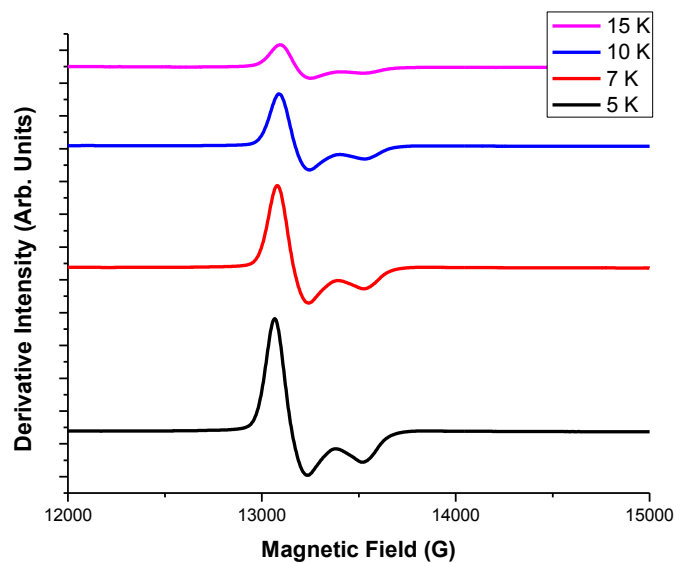
Figure IV.20: Variable temperature EPR spectra of a powdered sample of

[{Cr$_7$NiF$_3$(Etglu)(O$_2$C^{t}Bu)$_{15}$}$_2$(pyCH$_2$CH$_2$py)] (**19**), at Q-band frequency.
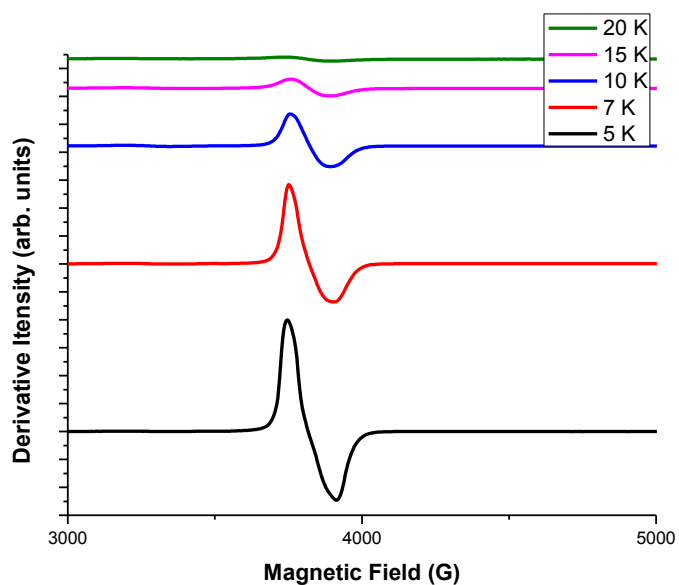
Figure IV.21: Variable temperature EPR spectra of a powdered sample

of[{Cr$_7$NiF$_3$(Etglu)(O$_2$C^{t}Bu)$_{15}$}$_2$(pyCH$_2$CH$_2$py)] (**19**), at X-band frequency.
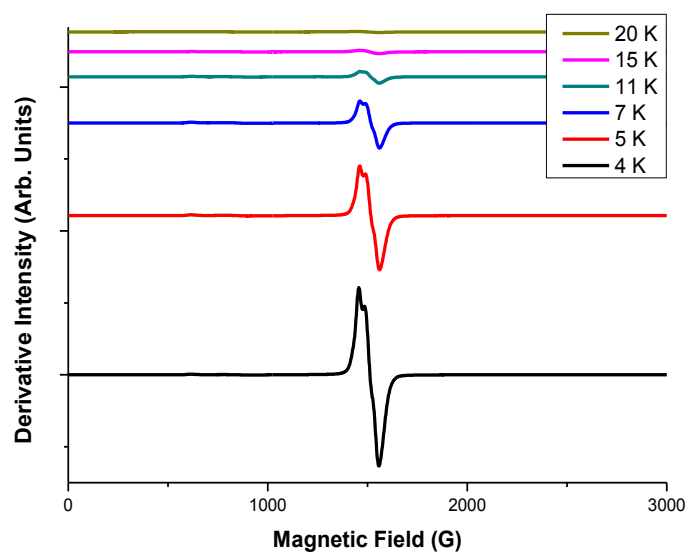
Figure IV.22: Variable temperature EPR spectra of a powdered sample of

[{Cr$_7$NiF$_3$(Etglu)(O$_2$C^{t}Bu)$_{15}$ }$_2$(pyCH$_2$CH$_2$py)] (**19**), at S-band frequency.

At all the frequencies which have been measured there is no resolved fine structure. Hence, the spectra resemble the $S = {}^1/_2$ spectra of the free wheel. However, the peaks are broader than those of **11**. This indicates that there is a weak interaction between the two halves of the (Cr$_7$Ni)$_2$ dimer. Therefore the spectra have been modelled as $S = 1$. The simulation and 5 K experiment at Q-band frequency are shown in Figure IV.23
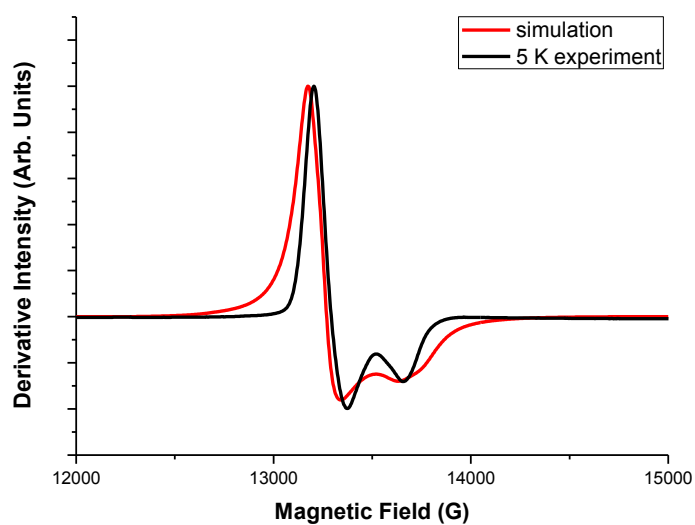
Figure IV.23: EPR spectrum (black line) and simulation of a powdered sample of compound **19** at Q-band frequency.
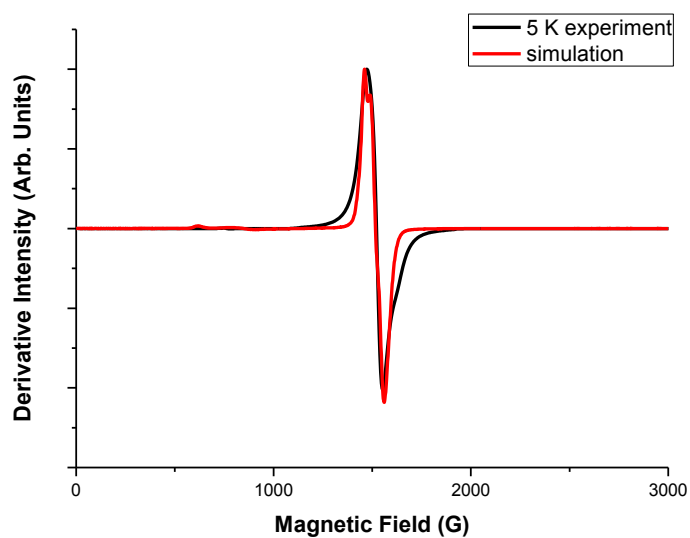
Figure IV.24: EPR spectrum (black line) and simulation of a powdered sample of compound **19** at S-band frequency.

The following spin-Hamiltonian parameters were used to model the experimental EPR data: D = +0.005 cm^{-1}, g_{xy} = 1.84 and g_z = 1.77. A D value of +0.005 cm^{-1} is the upper limit of the anisotropic exchange.

IV.4.4 EPR Study of [(Cr$_7$NiF$_3$(Etglu)(O$_2$C^{t}Bu)$_{15}$)$_2$(pyCH(OH)CH(OH)py)]

A multi-frequency, variable temperature EPR study was performed on [{Cr$_7$NiF$_3$(Etglu)(O$_2$C^{t}Bu)$_{15}$}$_2$(pyCH(OH)CH(OH)py)] (**20**). The crystal structure of compound **20** is shown in Figure IV.25. The conformation of the two wheels in the dimer is atypical to the rest of the family. The two wheels are orientated at almost right angles to one another. The measured angle between the two mean planes of the eight metal centres in each wheel within the dimer is 72.48°: This is the largest angle in the series. The through bond Ni^{2+}-Ni^{2+} distance was also found to be the longest in the series, at 16.78 Å. However the Ni^{2+} to Ni^{2+} distance is very short at 10.84 Å.
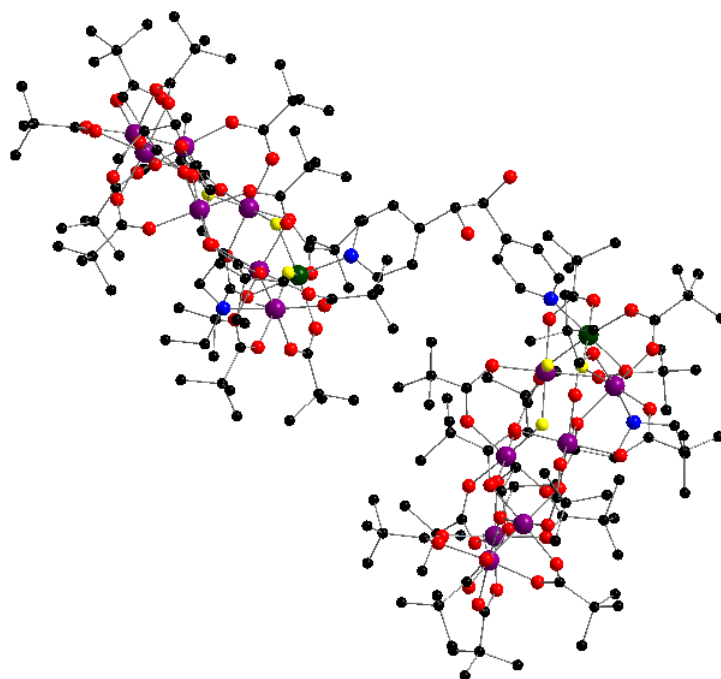
Figure IV.25: [{Cr$_7$NiF$_3$(Etglu)(O$_2$C^{t}Bu)$_{15}$}$_2$(pyCH(OH)CH(OH)py)] (**20**). Colours; Cr atoms: purple; Ni atom: green; C atoms: black; F atoms: yellow; N atoms: blue; O atoms: red. All H atoms have been removed for clarity.

The powder EPR spectra of compound **20** are shown below. Measurements were made at Q-, X- and S-band frequencies. (Figure IV.26, IV.27 and IV.28 respectively).
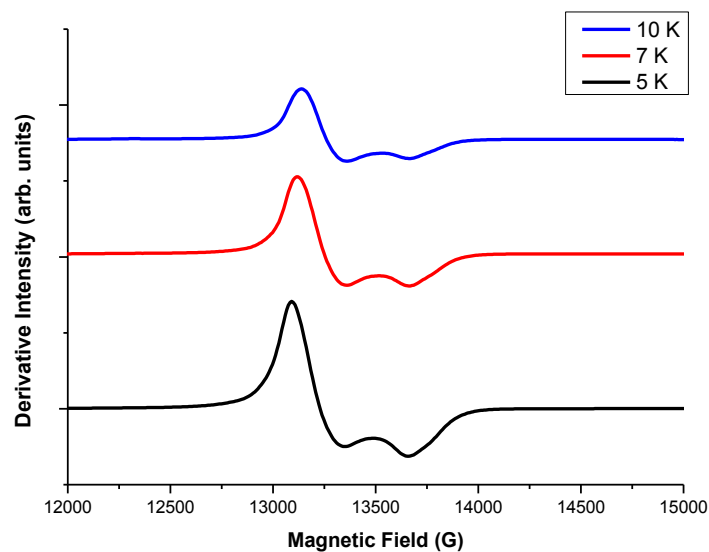
Figure IV.26: Variable temperature EPR spectra of a powdered sample of [{Cr$_7$NiF$_3$(Etglu)(O$_2$C^{t}Bu)$_{15}$}$_2$(pyCH(OH)CH(OH)py)] (**20**), at Q-band frequency.
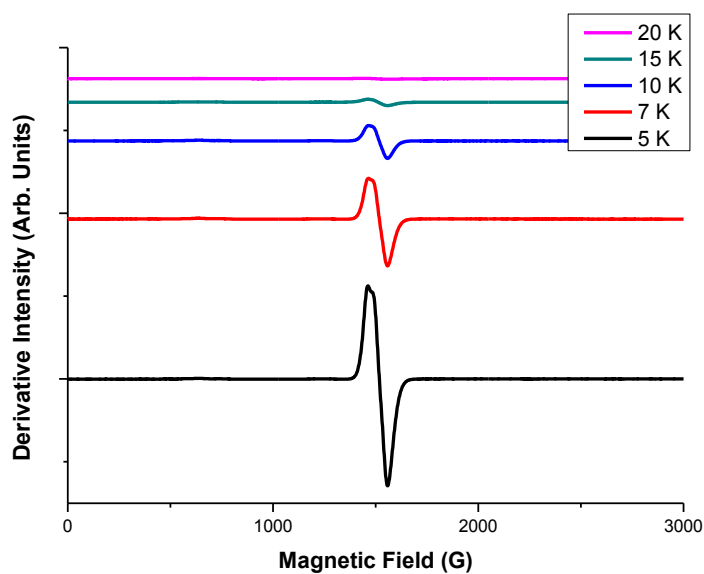
Figure IV.27: Variable temperature EPR spectra of a powdered sample of [{Cr$_7$NiF$_3$(Etglu)(O$_2$C^{t}Bu)$_{15}$}$_2$(pyCH(OH)CH(OH)py)] (**20**), at X-band frequency.
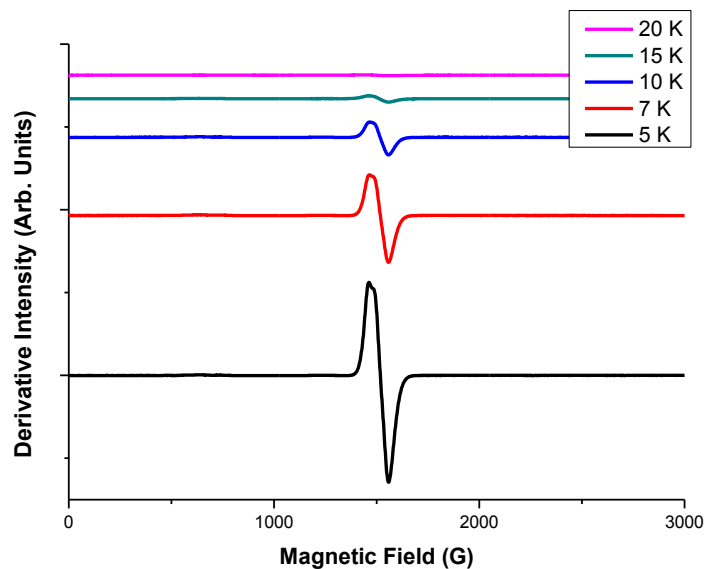
Figure IV.28: Variable temperature EPR spectra of a powdered sample of [{Cr$_7$NiF$_3$(Etglu)(O$_2$C^{t}Bu)$_{15}$}$_2$(pyCH(OH)CH(OH)py)] (**20**), at S-band frequency.

At all frequencies there are single broad resonances, which are broader than that of **2**. This indicates a weak interaction, therefore the spectra have been modelled as $S = 1$. The D value determined is the upper limit of the anisotropic exchange. The spectra can be modelled with: $D = + 0.004$ cm^{-1}, $g_{xy} = 1.84$ and $g_z = 1.77$. The Q- and S-band experimental spectra and simulations are shown in Figures IV.29 and IV.30.
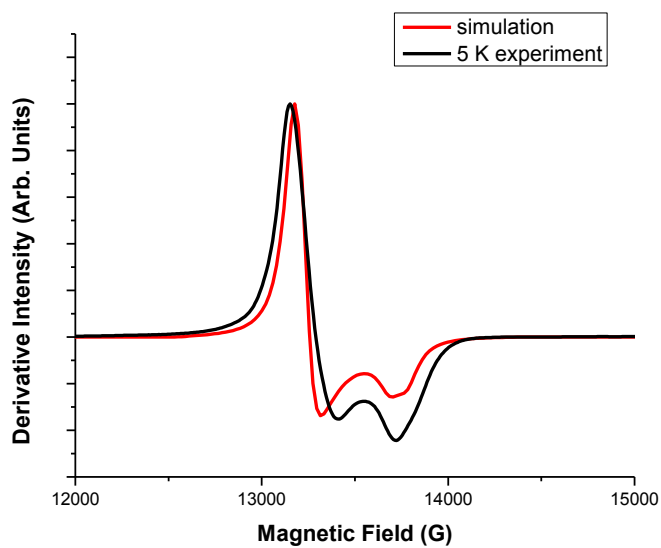
Figure IV.29: EPR spectrum (black line) and simulation of a powdered sample of [{Cr$_7$NiF$_3$(Etglu)(O$_2$C^{t}Bu)$_{15}$}$_2$(pyCH(OH)CH(OH)py)] (**20**) at Q-band frequency.
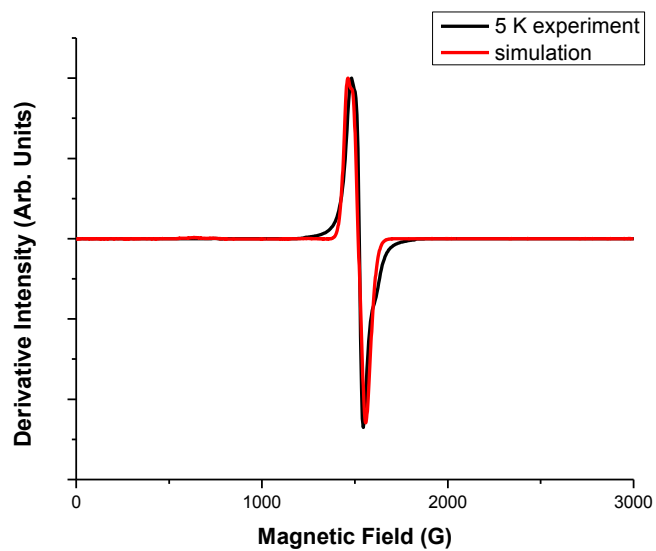
Figure IV.30: EPR spectrum (black line) and simulation of a powdered sample of [{Cr$_7$NiF$_3$(Etglu)(O$_2$C^{t}Bu)$_{15}$}$_2$(pyCH(OH)CH(OH)py)] (**20**) at S-band frequency.
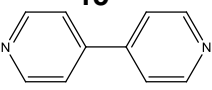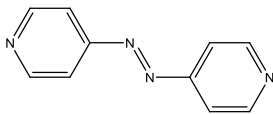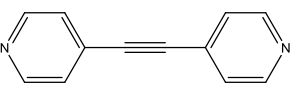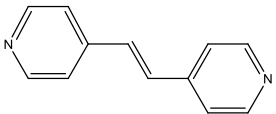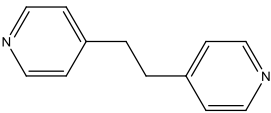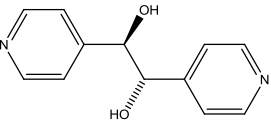
IV.5 Conclusions

Figure IV.31 shows Q-band frequency EPR spectra recorded at 5 K of compounds **15** to **20**. They are ordered by the magnitude of their D tensor. Black dashes have been used to highlight the decreasing value of D along the series, by marking equivalent transitions within the series. The table below summarizes the spin-Hamiltonian parameters of compounds **15** to **20**, along with measurements which were taken from the crystal structures.
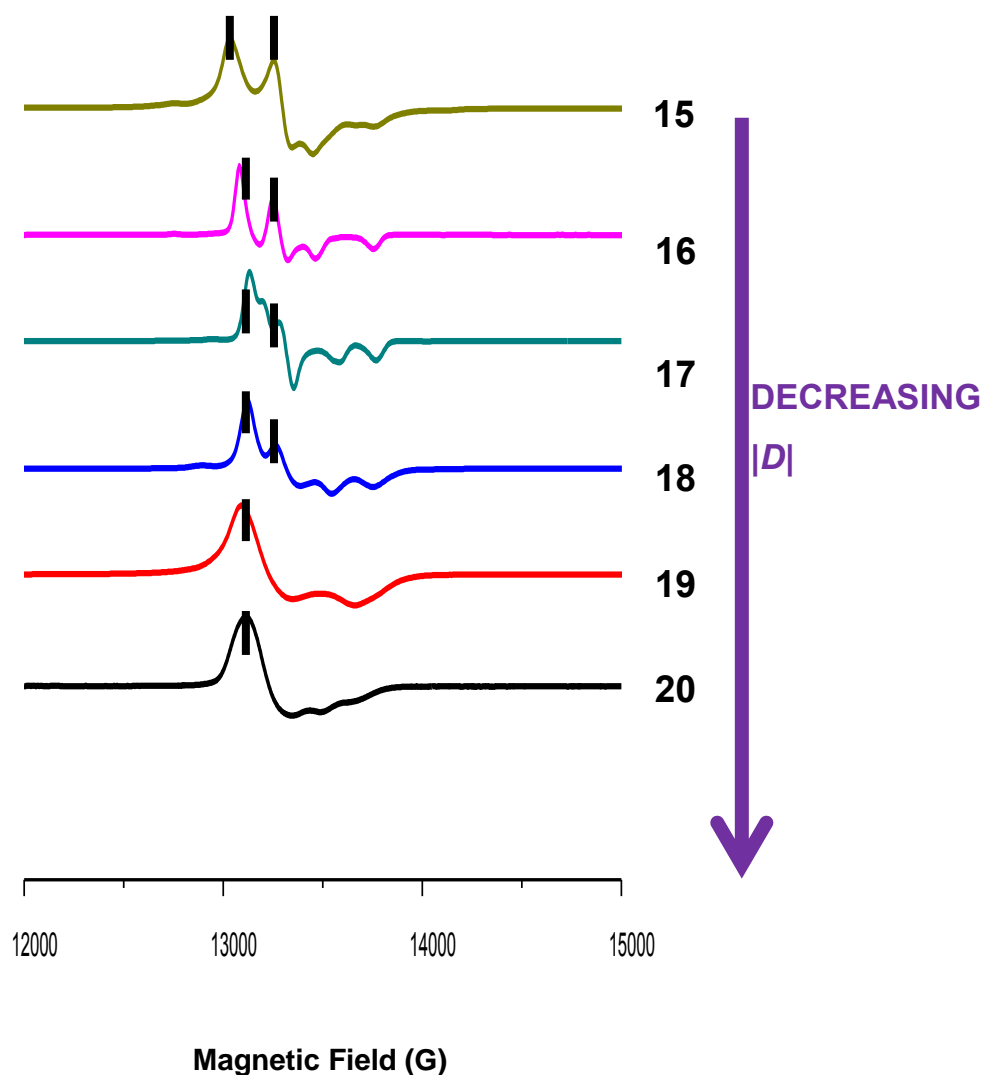
Figure IV.31: Q-band spectra of polycrystalline samples of compounds **15** to **20**. The

black dashes highlight the decreasing value of |D|.

Table IV.1: Summary of D tensor, through-bond and through space Ni^{2+} to Ni^{2+} distance, the angle between mean planes of the metal centres in each wheel in a dimer, and torsion angle through wheel-linker-wheel for compounds **15** to **20**.

Compound Number and Organic Linker	D (cm^{-1})	Through-Space Ni···Ni distance (Å)	Through-Bond Ni···Ni Distance (Å)	Angle Between Best Planes (°)	Cr···Ni··· Ni···Cr Torsion Angle (°)
15	+ 0.013	11.218	13.796	8.37	89.90
16	+ 0.011	13.115	16.331	21.37	130.74
17	+ 0.008	13.680	16.339	31.75	135.30
18	+ 0.009	13.430	16.591	33.06	133.59
19	+ 0.005	12.898	16.469	31.75	135.30
20	+ 0.004	10.824	16.784	72.48	113.36

- The single purple-(Cr_7M) wheels have been linked electronically as well as chemically.

  The individual purple-(Cr_7Ni) wheels in the dimers behave as effective $S = \frac{1}{2}$ spin clusters at sufficiently low temperatures. Hence a wheel dimer will produce a spin triplet and a singlet if there is communication between the two purple-(Cr_7Ni) wheels. For compounds **15** to **18** there is clearly a spin triplet EPR spectrum below 10 K. For compounds **19** and **20** the spectrum is not well resolved, however the EPR spectra of these compounds is distinctly broader than that of a single purple-(Cr_7Ni). Therefore they have been modelled as spin triplet spectra.

- A relationship between |D| and the organic linker has been established

  It is apparent is that there is a decrease in the magnitude of the D tensor for the unsaturated linkers from **15** to **18**. When rationalizing these results with molecular structure it is evident that there does not appear to be a direct correlation between the torsion angles or with the angle between the planes of the metal centres with the D tensor. However there does appear to be a trend between the through bond $Ni^{2+}\cdots Ni^{2+}$ distance and the D tensor. The shorter unsaturated linkers, when calculated through bond, exhibit a larger value of D. This is an intuitive result, as you would expect there to be more efficient electronic communication between the two wheels *via* a shorter organic linker. The magnitude of the D tensor is smaller when the wheels are linked by an saturated linker, such as compounds **19** and **20**. There is a clear difference between saturated and unsaturated linkers. There is more efficient magnetic superexchange through a fully conjugated π-system. Compounds **16** and **18** have isoelectronic organic linkers, however **16** has a larger value of D. This may be due to 4,4'-azopyridine being a shorter linker. An unexpected result is that **17** has a smaller D value than **18**. This result is anomalous and further investigation between D and the structure of the organic linker is required. 1,2-di(4-pyridyl)ethyne has a shorter through-bond $Ni^{2+}\cdots Ni^{2+}$ distance than *trans*-1,2-di(4-pyridyl)ethene. Perhaps the orientation of the wheels in **18** promotes more efficient magnetic superexchange between the two wheels.

142

- <u>Quantum computing demands certain pre-requisites; The (Cr$_7$Ni) family can fulfil at least some of them already.</u>

It has been demonstrated that the purple-{Cr$_7$Ni} wheels are robust enough to be linked together into larger supramolecular structures. This is important as it would be advantageous to use supramolecular chemistry to produce qubits as the synthetic techniques which are used are very simple, and they allow for the production of vast numbers of regular arrays of molecules. What is now desirable would be to introduce switch-ability of the interaction within a {Cr$_7$Ni}$_2$-L dimer, possibly by the use of redox- or photo-active linking molecules. This would be an essential feature to implement the design of a two-qubit gate, which was given by Loss in 2003.[13] A single crystal EPR spectroscopy experiment has been attempted on compound **15**, these initial rotations show considerable anisotropy (See *Appendix* VIII.3 for further details). Completion of this study will be able to relate the electronic structure with the molecular structure of the prototype two-qubit gate.

IV.6 References

1.   L. K. Grover, *Phys. Rev. Lett.*, 1997, **79**, 4709.

2.   P. W, Shor, Foundations of Computer Science, 1994, Proceedings 35th Ann. Symp. IEEE Computer Society.

3.   C. H. Bennett and D. P. DiVincenzo, *Nature*, 2000, **404**, 247-255.

4.   J. Lehmann, A. Gaita-Arino, E. Coronado and D. Loss, *J. Mater. Chem.*, 2009, **19**, 1672-1677.

5.   O. Voskoboynikov and C. M. J. Wijers, *J. Comput. Theor. Nanosci.*, 2010, **7**, 1723-1726.

6.   V. Privman, I. D. Vagner and G. Kventsel, *Phys. Lett. A*, 1998, **239**, 141-146.

7.   B. E. Kane, *Nature*, 1998, **393**, 133-137.

8.   J. Cirac, *Nature*, 2000, **404**, 579.

9.   A. Candini, G. Lorusso, F. Troiani, A. Ghirri, S. Carretta, P. Santini, G. Amoretti, C. Muryn, F. Tuna, G. Timco, E. J. L. McInnes, R. E. P. Winpenny, W. Wernsdorfer and M. Affronte, *Phys. Rev. Lett.*, **104**, 037203.

10.   G. A. Timco, E. J. L. McInnes, R. J. Pritchard, F. Tuna and R. E. P. Winpenny, *Angew. Chem. Int. Ed.*, 2008, **47**, 9681-9684.

11.   M. Le Bellac, *Quantum Information and Quantum Computation*, Cambridge University Press, Cambridge, 2006.

12.   M. A. Nielsen and I. L. Chuang, *Quantum Computation and Quantum Information*, Cambridge University Press, Cambridge, 2000.

13.   F. Meier, J. Levy and D. Loss, *Phys. Rev. B*, 2003, **68**, 134417.

14.   H. Miyasaka, K. Nakata, L. Lecren, C. Coulon, Y. Nakazawa, T. Fujisaki, K-I. Sugiura, M. Yamashita and R. Clérac, *J. Am. Chem. Soc.*, 2006, **128**, 3770-3783.

15.   H. Miyasaka, K. Takayama, A. Saitoh, S. Furukawa, M. Yamashita and R. Clérac, *Chem. Eur. J.*, **16**, 3656-3662.

16.   A. Wilson, S. Hill, R. S. Edwards, N. Aliaga-Alcalde and G. Christou, *AIP Conf. Proc.*, 2006, **850**, 1141-1142.

17.   F. Troiani, V. Bellini and M. Affronte, *Phys. Rev. B*, 2008., **77**, 054428.

V   Homometallic Cr^{3+} Horseshoes and Wheels

V.1 Introduction

Physical studies on a family of antiferromagnetically coupled homometallic clusters have been pursued. They consist of cyclic arrays of homometallic Cr^{3+} metal centres in either a wheel or horseshoe shaped formation. The structure of $[Cr_8F_8(O_2C^tBu)_{16}]$ (**1**) was first published in 1990.[1] Since then it has been the subject of numerous physical studies to investigate its magnetic properties. The metal centres within **1** are antiferromagnetically coupled to their nearest neighbours, resulting in an $S = 0$ ground state. High frequency (230 GHz) EPR measurements and cantilever torque magnetometry have been used to determine the axial zero field splitting of the first two excited states. This was found to be $D = 1.68$ cm^{-1} for the first $S = 1$ excited state and $D = 0.405$ cm^{-1} for the next adjacent $S = 2$ excited state, with an isotropic g-value of 1.98 for both spin states.[2] More recently a new type of Cr_8 wheel has been synthesised: $[Cr_8F_4(Etglu)(O_2C^tBu)_{15}]$ (**21**), essentially the homometallic analogue of the purple-Cr_7M discussed in Chapter III.[3] Magnetic susceptibility measurements have been performed on both **1** and **21** to determine the exchange interaction between Cr^{3+} centres. The following exchange Hamiltonian was used:

$$\widehat{H} = -2J_{(i,j)} \sum_{i \neq j}^{8} S_i\, S_j$$

Equation V.1

For **20**, an exchange interaction between neighbouring Cr^{3+} centres of $J = -5.9$ cm^{-1} has been determined.[2] For compound **21**, much larger J-values of ~ -11.5 cm^{-1} have been fitted to SQUID magnetometry and INS measurements.[4] The large difference in J-values has led to further investigation by EPR spectroscopy.

Molecular Cr^{3+} horseshoes are finite metal chains. There are very few examples of such species in the literature. Those that have been synthesised include systems which consist of long linear chains of metal ions which have been studied for possible applications as molecular wires. For example, metal centres are bridged by oligo-α-dipyridylamines are known for Ni^{2+},[5] Co^{2+} [6] and Cr^{2+}.[7] Strong exchange terms have been determined for these compounds. The Cr^{3+} horseshoe studied here exist as the general formula $[Cr_xF_{x+5}L_{2x-2}]_2{}^{3-}$ (where L = carboxylate and x = 6 or 7) and are formed from the reaction of pivalic acid, hydrated chromium fluoride and either diethyl amine or propylamine, at 140 $^\circ$C for 16h; for example, $[Et_2NH_2]_3[Cr_6F_{11}(O_2CCMe_3)_{10}]_2$ (**22**) is formed with the following stoichiometry:[8]

$12CrF_3 \cdot 4H_2O + 20HO_2C^tBu + 6HNEt_2 \rightarrow [Et_2NH_2]_3[Cr_6F_{11}(O_2C^tBu)_{10}]_2$

Figure V.1 shows the structure of **22**.
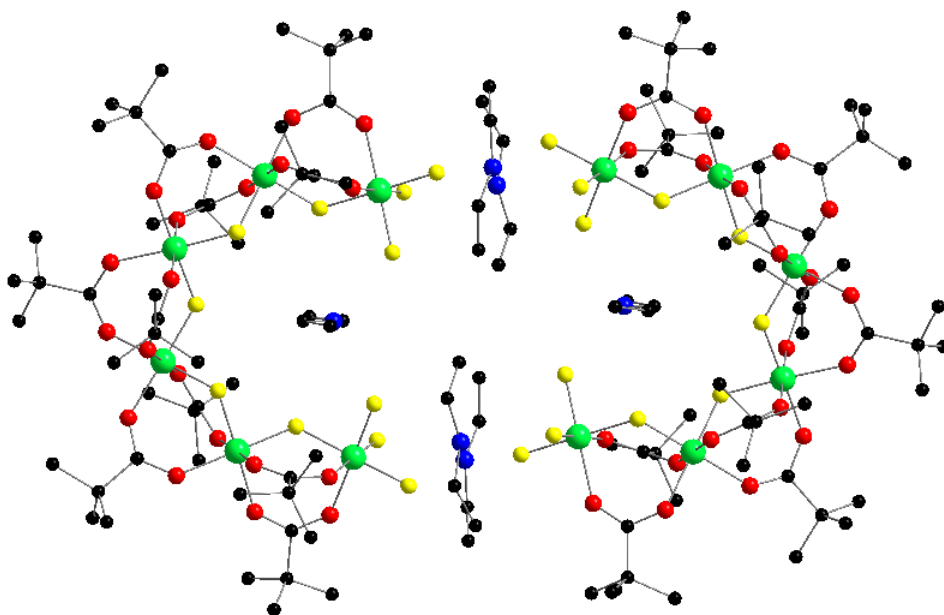
Figure V.1: The structure of $[Et_2NH_2]_3[Cr_6F_{11}(O_2C^tBu)_{10}]_2$ (**22**) in the crystal. Colours; Cr atoms: light green; C atoms: black; F atoms: yellow; N atoms: blue; O atoms: red. All H atoms have been removed for clarity.

Between adjacent Cr^{3+} centres, there is a bridging fluoride ion and two pivalate groups, as in the parent molecule compound **1**. The horseshoes share the same cyclic motif as **1**, with either one or two metal centres missing. The two terminal Cr^{3+} cations at the tips of the horseshoe each have three terminal fluoride anions completing the coordination sphere. These fluoride anions are involved in hydrogen bonding interactions with the secondary ammonium cations at the centre of the structure, thus forming a dimer. The terminal fluoride groups have been shown to be labile enough for substitution reactions. Thus, the *di*-horseshoe structures can be split apart into single horseshoes by a substitution reaction with a *β*-diketonates. The *β*-diketonate ligand chelates to the terminal chromium ions of each horseshoe, replacing two of the terminal fluorides and breaking the H-bonding interaction between the horseshoe and the dialkyl ammonium cation.

V.2 Results and Discussion

V.2.1 An EPR Study of $[Cr_8F_4(Etglu)(O_2C^tBu)_{15}]$

An EPR study of $[Cr_8F_4(Etglu)(O_2C^tBu)_{15}]$ (**21)** was performed. The wheel consists of eight Cr^{3+} centres in an octagon. A chiral glutamine molecule is penta-deprotonated and bound to the metal centres through all available metal donors. There are three bridging fluoride ions. There is one terminal fluoride ion at one of the metal centres. This is in an analogous position to the uncharged terminal ligand in purple-Cr_7M, thus maintaining charge balance. The compound is a deep purple colour and the chromium ions are depicted as purple in Figure V.2 to highlight the difference between the green homometallic wheel **1**.
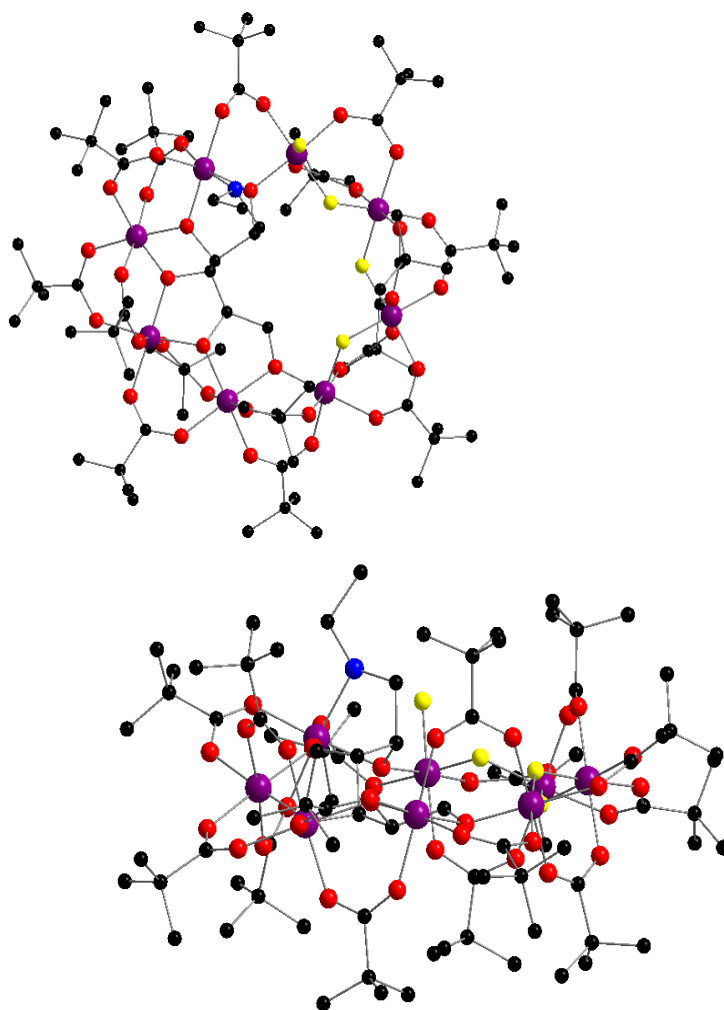
Figure V.2: Top and side views of $[Cr_8F_4(Etglu)(O_2C^tBu)_{15}]$ (**21**) in the crystal. Colours; Cr atoms: purple; C atoms: black; F atoms: yellow; N atoms: blue; O atoms: red. All H atoms have been removed for clarity.

Polycrystalline samples of **21** were measured at X-, Q- and W-band frequencies at VT. The first two excited states are observed by EPR. Figure V.3 shows the W-band 5 K EPR spectrum of **21** and simulation. This simulation was modelled within the SEL, using the spin Hamiltonian given in Equation II.1. The following spin-Hamiltonian parameters were used to model the $S = 1$ first excited state: $D = 1.215$ cm^{-1}, $E = 0.15$ cm^{-1}, $g_{xz} = 1.97$, $g_y = 2.01$; and for the $S = 2$ next excited state: $D = 0.17$ cm^{-1}, $E =$

0.003 cm^{-1}, B^4_0 = 0.002 cm^{-1}, g$_{iso}$ = 1.97. The B^4_0 term is required to account for the resonance at 34.780 cm^{-1}. Isotropic line widths of 200 G were used throughout.
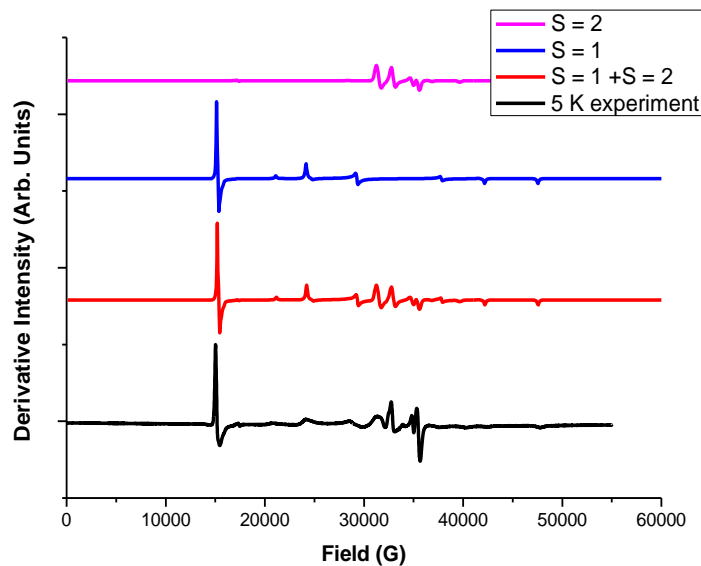
Figure V.3: 5 K W-band EPR spectrum of [Cr$_8$F$_4$(Etglu)(O$_2$C^{t}Bu)$_{15}$] (**21**) and simulation. $D_{S=1}$ = 1.215 cm^{-1}, E = 0.15 cm^{-1}, g$_{xz}$ = 1.97, g$_y$ = 2.01. $D_{S=2}$ = 0.17 cm^{-1}, E = 0.003 cm^{-1}, B^4_0 = 0.002 cm^{-1}, g$_{iso}$ = 1.97. Isotropic line widths of 200 G have been used throughout. At ν = 94.756 GHz.
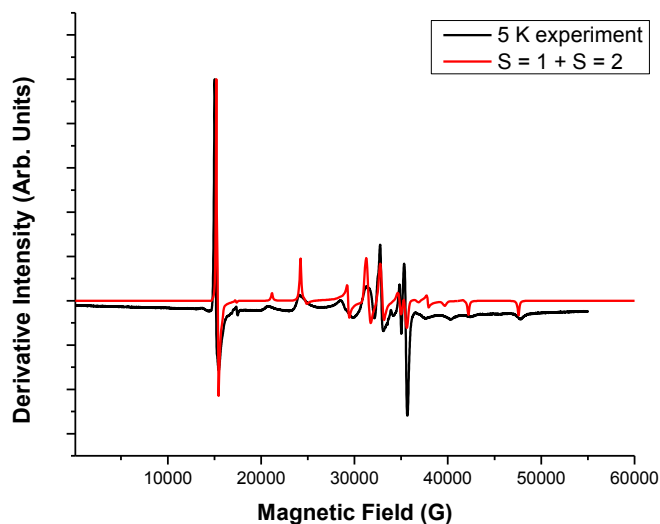
Figure V.4: 5 K W-band EPR spectrum of [Cr$_8$F$_4$(Etglu)(O$_2$C^{t}Bu)$_{15}$] (**21**) and S = 1 + S = 2 simulation.

150

The magnitude of D for the $S = 1$ first excited state is in good agreement with INS measurements that have been performed by Dr. M. L. Baker of Institute Laue-Langevin, Grenoble, France using IN5b (Figure V.5) There is zero field splitting of 0.15 meV (1.215 cm^{-1}) between $\left| S = 1, M = 0 \right\rangle$ and $\left| S = 1, M = \pm 1 \right\rangle$.[4]
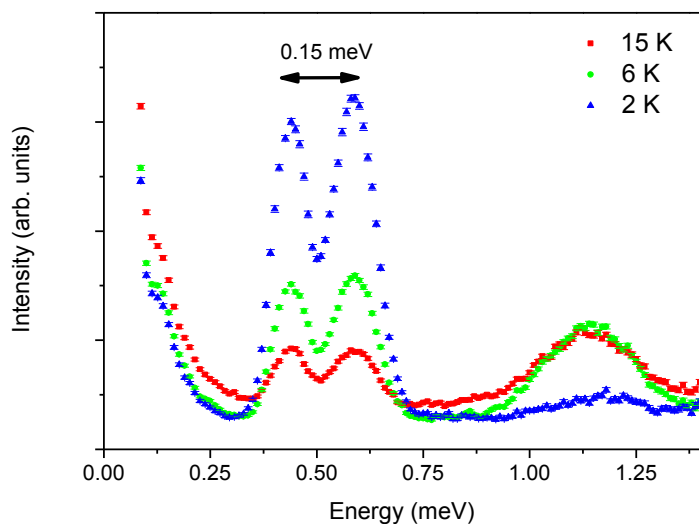
Figure V.5: Inelastic-neutron-scattering results for [Cr$_8$F$_4$(Etglu)(O$_2$C^{t}Bu)$_{15}$] (**21**) obtained with an incident wavelength of 6 Å at 2 K, 6 K and 15 K.

Figure V.6 compares the Q-band EPR of **1** and **21**. The spectra are distinctly different, proving that different spin-Hamiltonian parameters are required to model the EPR data of the two compounds.
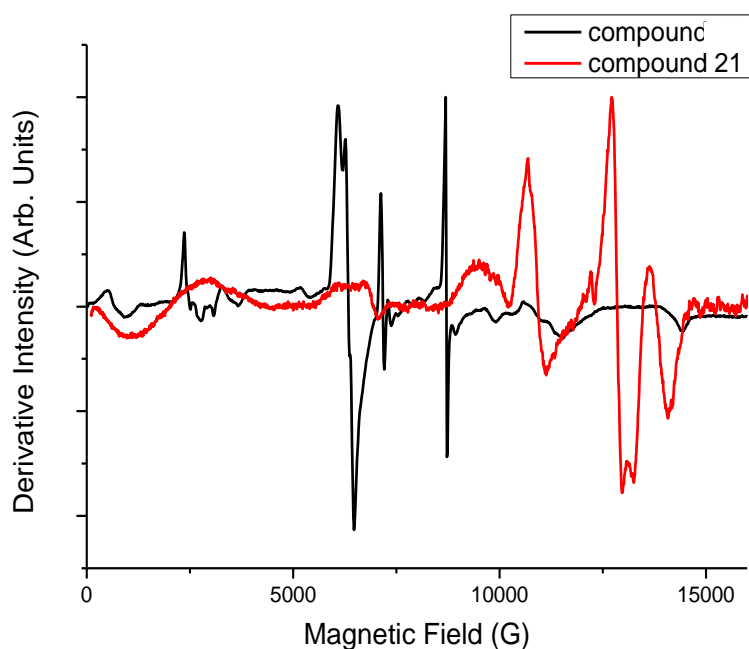
Figure V.6: Q-band 5 K EPR spectra of $[Cr_8F_8(O_2C^tBu)_{16}]$ (**1**) and $[Cr_8F_4(Etglu)(O_2C^tBu)_{15}]$ (**21**).

Compound **21** has a smaller value of D than **1** (for **21**, D = 1.68 cm^{-1} and for **1**, D = 1.215 cm^{-1}). The explanation for this is analogous to what was given for the magnitude of the spin-Hamiltonian parameters of the purple-Cr$_7$M wheels in Chapter III. The smaller D-value is possibly due to the replacement of fluoride ions with alkoxide donors. Oxygen donors are stronger field ligands than fluoride anions. This results in **21** having a larger value of Δ_{oct} and therefore less SOC, leading to a smaller D tensor. The percentage decrease in D-value of 20 and 21 is ~30 %. The percentage decrease in D of the purple-Cr$_7$M wheels in comparison to the green-Cr$_7$M (Chapter III) is also ~30 %. λ is larger for compound **21**, this can be simply explained by the increased number of different coordination environments in **21,** thus increasing the rhombicity of

the system. Larger λ values were also observed for the purple-Cr_7M wheels in comparison to the green-Cr_7M wheels.

V.2.2 Synthetic and Structural Studies of Hexanuclear Horseshoes

A family of hexanuclear Cr^{3+} horseshoes were studied. The dimeric horseshoe **22** is the parent molecule to two types of monomeric $\{Cr_6\}$ horseshoes $[Et_2NH_2][Cr_6F_7(O_2C^tBu)_{10}(acac)_2]$ (**23**, Figure V.7) and $[EtNH_2][Cr_6F_7(O_2C^tBu)_{10}(Hfa)_2]$ (**24**, Figure V.9). They are formed from **22** by substitution reactions with acetylacetone (acacH) and hexafluoroacetylacetone (hfaH) respectively. The formation of **23** proceeds with the following stoichiometry:

$[Et_2NH_2]_3[Cr_6F_{11}(O_2C^tBu)_{10}]_2$ + 4 Hacac $\rightarrow$

$[EtNH_2][Cr_6F_7(O_2C^tBu)_{10}(acac)_2]$ + 4 $[Et_2NH_2]F$ + 4 HF.
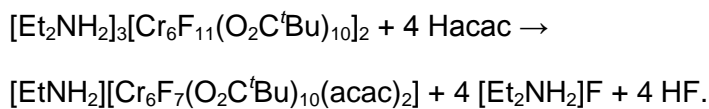
Compound 23 is a new compound, details of the synthetic preparation are given in section VI.1. It crystallizes in a triclinic $P\bar{1}$ space group. Crystallographic information of **23** is given in *Appendix* VIII.4. Figure V.8 is a crystal packing diagram of **23**, it shows that the horseshoes are not arranged in pairs. The $\{Cr_6\}$ polymeric horseshoe, $[Et_2NH_2]_3[Cr_6F_{11}(O_2C^tBu)_{10}]\cdot\{C_6H_4-1,4-(OH)_2\}_2$ (**25**) is formed from the crystallization of **22** with hydroquinone from $Et_2O/$ THF. The horseshoes are arranged in pairs and the dimers are connected in a polymeric structure through H-bonding interactions with hydroquinone. A packing diagram of **25** is shown in Figure V.8 to show the intermolecular arrangement of the horseshoes. There are 3 types of terminating groups in this family: $3F^-$, acac and Hfa.
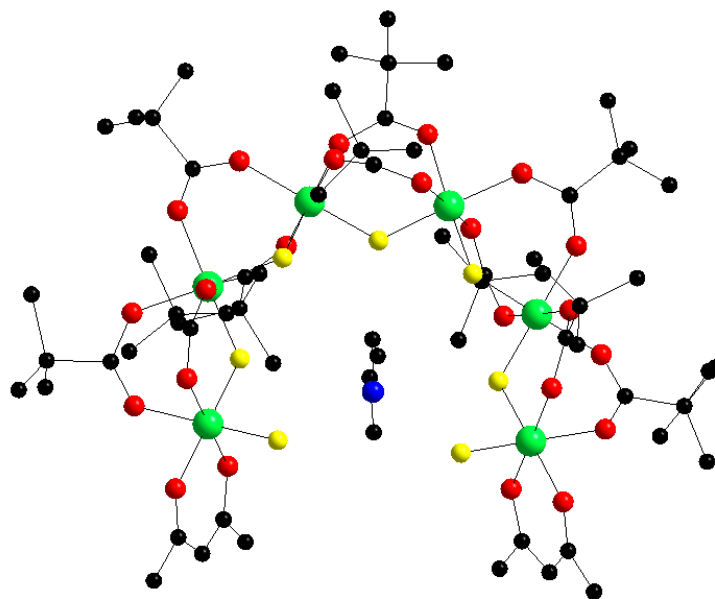
Figure V.7: The structure of [EtNH$_2$][Cr$_6$F$_7$(O$_2$C^{t}Bu)$_{10}$(acac)$_2$] (**23**) in the crystal. The colours are as before. All H atoms have been removed for clarity.
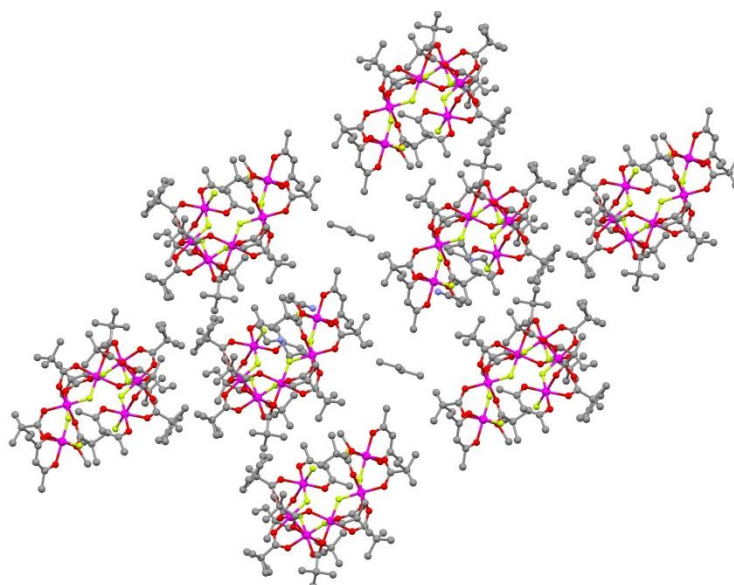
Figure V.8: Packing diagram of [EtNH$_2$][Cr$_6$F$_7$(O$_2$C^{t}Bu)$_{10}$(acac)$_2$] (**23**) in the crystal.
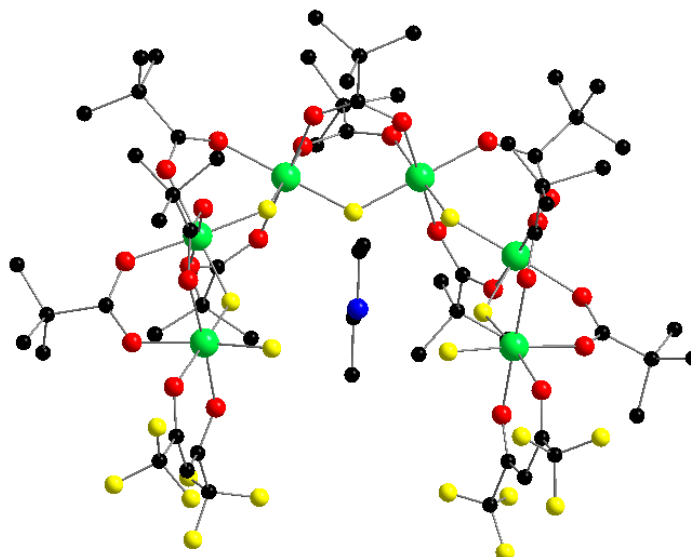
Figure V.9: The structure of [EtNH$_2$][Cr$_6$F$_7$(O$_2$C^{t}Bu)$_{10}$(Hfa)$_2$] (**24**) in the crystal. The colours are as before. All H atoms have been removed for clarity.
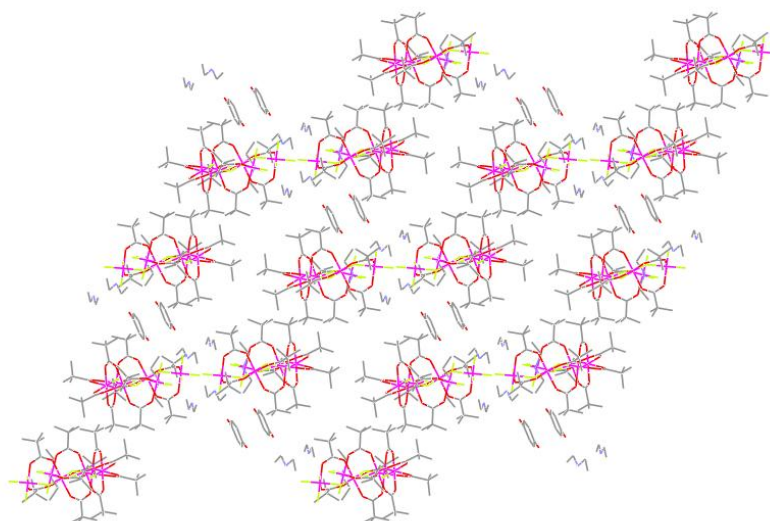
Figure V.10: Packing diagram of [Et$_2$NH$_2$]$_3$[Cr$_6$F$_{11}$(O$_2$C^{t}Bu)$_{10}$]·{C$_6$H$_4$-1,4-(OH)$_2$}$_2$ (**25**) in the crystal.

Table V.1 shows bond lengths and bond angles of compounds **22** to **25** (Average Esd = 0.006 Å and 0.2 °). There are small variations in bond lengths and bond angles between the four compounds. The Cr-O (diketonate) bond lengths are slightly longer in **24** in comparison to **23**. Also the Cr-F (terminal) bond lengths are slightly longer in **23**. The Cr-O (carboxylate) bond lengths are longer in **22** and **25**, than in the $\{Cr_6\}$ monomers. All of the horseshoes have very similar Cr···Cr distances.

Table V.1: The bond angles (^{o}) and bond lengths (Å) of compounds **22**, **23**, **24** and **25**. Average Esd = 0.006 Å and 0.2 °.

Compound	**22**	**23**	**24**	**25**
Cr-F (bridging)	1.891-1.943	1.893-1.945	1.902-1.934	1.883-1.950
Cr-O (carboxylate)	1.930-2.006	1.943-1.992	1.962-1.969	1.913-2.003
Cr-O (diketonate)	N/A	1.930-1.951	1.960-1.980	N/A
Cr-F (terminal)	1.852-1.879	1.873	1.842	1.847-1.909
O-Cr-O cis	87.04-91.00	87.5-92.9	85.8-97.2	87.66-92.91
O-Cr-O trans	177.8-179.1	176.3-178.8	176.2-179.6	178.0-179.6
O-Cr-F cis	90.27-93.28	86.5-93.8	87.8–93.0	88.57-92.77
O-Cr-F trans	177.4-79.5	177.3–179.7	174.3–179.8	176.84-79.66
F-Cr-F cis	87.85-89.10	87.4–89.8	87.6–90.6	88.5 – 91.14

V.2.3 EPR Studies of Cr^{3+} Hexanuclear Horseshoes

The Q-band 5 K EPR spectra of **22** to **25** are shown in Figure V.11. What is immediately apparent is that the EPR of **22** and **25** are very similar and that **23** and **24** are very similar. The half field resonance at ~3,800 G in **22** and **25** is due to a formally forbidden $\Delta M_s = \pm 2$ transition in the $S = 1$ spin state. At Q-band frequency this transition is not observed in **23** and **24**, but it is observed at W-band frequency. The other features in the spectra are mostly due to the spin quintet state.
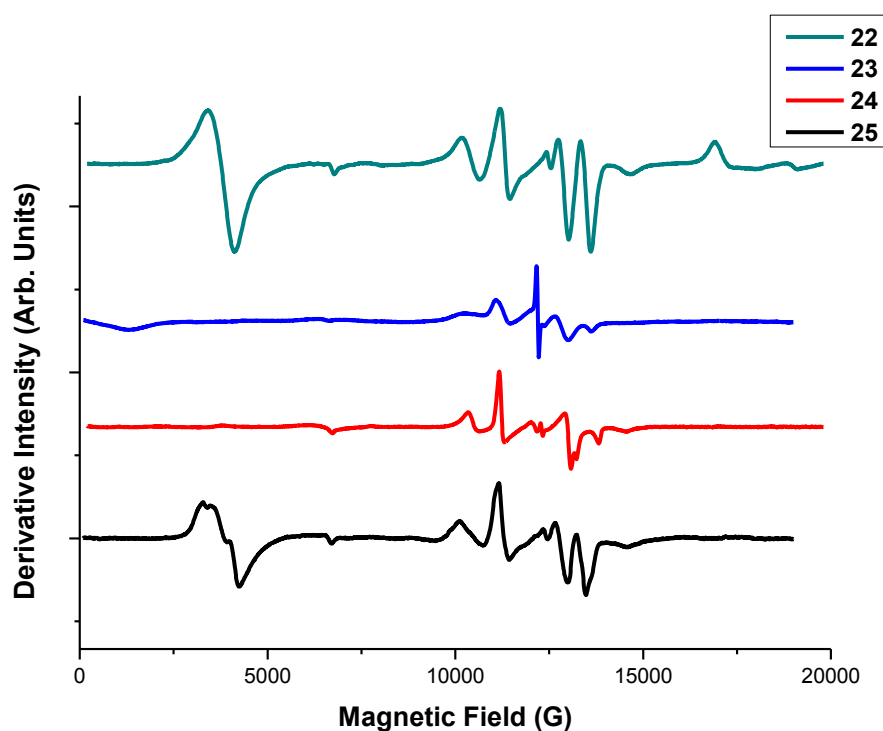
Figure V.11: Q-band EPR of polycrystalline samples of compounds **22** to **25**.

The EPR data of the four compounds were modelled with the SEL, using the Hamiltonian given in Equation II.2. In summary:

- The EPR of **22** can be modelled with the following spin Hamiltonian parameters for the $S = 1$ excited state: $D = $ -0.713 cm^{-1}, $E = 0.146$ cm^{-1}, $g_x = 1.995$, $g_y = 1.980$, $g_z = 1.970$. For the $S = 2$ excited state, $D = +0.1377$ cm^{-1}, $E = 5.67$ x

10-3 cm^{-1}, B_0^4 = 2.754 x 10^{-4} cm^{-1} g_{xy} = 1.976 and g_z = 1.972.[9] The B_0^4 term is required to model the intensity of the highest field feature of the S = 2 state.

- The EPR spectra of **23** can modelled with the following spin Hamiltonian parameters for the $S = 1$ excited state: D = -1.07 cm^{-1}, E = 0.15 cm^{-1}, g_{iso} = 1.97. The $S = 2$ excited state: D = -0.19 cm^{-1}, E =0.006 cm^{-1}, g_{iso} = 1.97 and isotropic Gaussian line widths of 200 G. The simulation is shown in Figures V.12 and V.13.
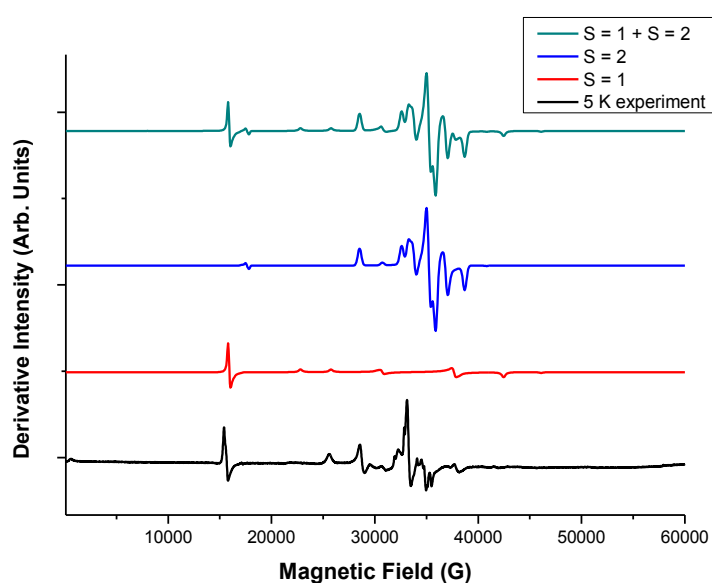
Figure V.12: 5 K W-band EPR spectrum of [Et$_2$NH$_2$][Cr$_6$F$_7$(O$_2$C^{t}Bu)$_{10}$(acac)$_2$] (**23**) and simulation. S = 1: D = -1.07 cm^{-1}, E = 0.15 cm^{-1}, g_{iso} = 1.97. S = 2: D = -0.19 cm^{-1}, E =0.006 cm^{-1}, g_{iso} = 1.97 and isotropic Gaussian line widths of 200 G. At frequency, ν = 95.119 GHz.
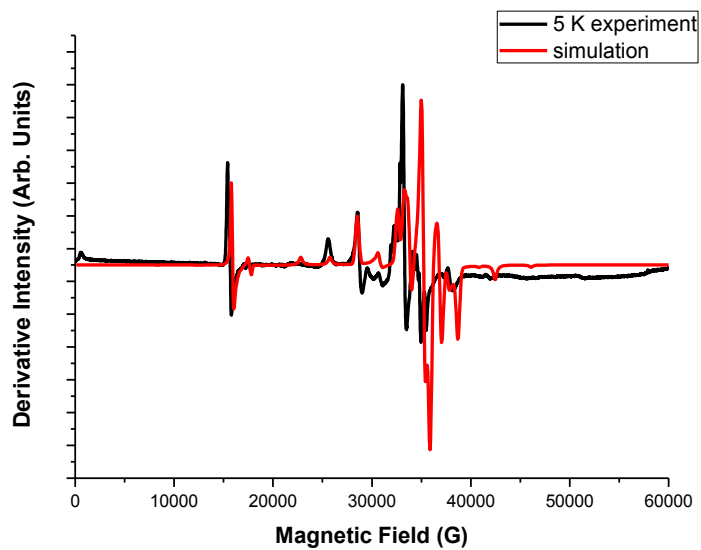
Figure V.13: 5 K W-band EPR spectrum of $[Et_2NH_2][Cr_6F_7(O_2C^tBu)_{10}(acac)_2]$ (**23**) and
$S = 1 + S = 2$ simulation.

- Compound **24** can be modelled with the following spin Hamiltonian parameters:
  $D = -1.07$ cm^{-1}, $E = 0.15$ cm^{-1}, $g_{iso} = 1.97$. The $S = 2$ spin state can be modelled
  with $D = 0.135$ cm^{-1}, $E = 0.003$ cm^{-1}, $g_{xz} = 1.97$ and $g_y = 1.94$.[10]

- Compound **25** can be modelled with the same spin-Hamiltonian parameters as
  22 (Figure V.14 and V.15).
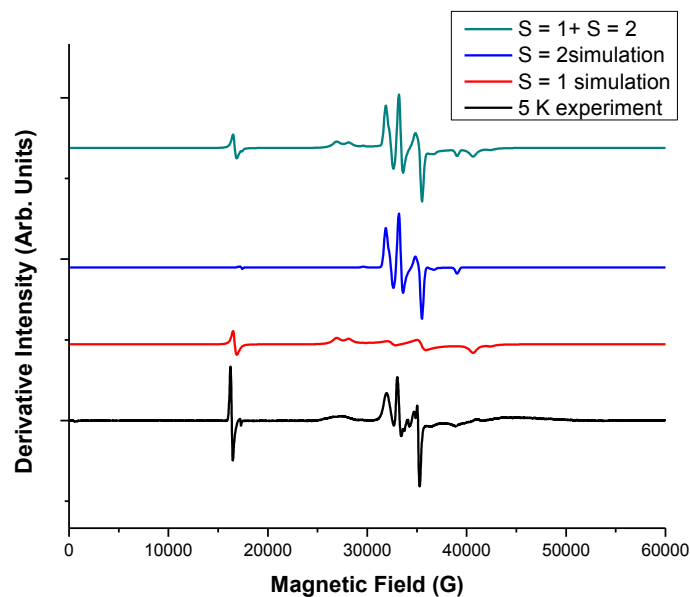
Figure V.14: 5 K W-band spectrum of $[Et_2NH_2]_3[Cr_6F_{11}(O_2C^tBu)_{10}]\cdot\{C_6H_4\text{-}1,4\text{-}(OH)_2\}_2$ (**25**) and simulation. $S = 1$: D = -0.713 cm^{-1}, E = 0.146 cm^{-1}, g_x = 1.995, g_y =1.980, g_z = 1.970. $S = 2$: D = +0.1377 cm^{-1}, E = 5.67 x 10-3 cm^{-1}, B_0^4 = 2.754 x 10^{-4} cm^{-1} g_{xy} = 1.976, g_z = 1.972 and isotropic Gaussian line widths of 200 G.

At frequency, ν = 98.199 GHz.
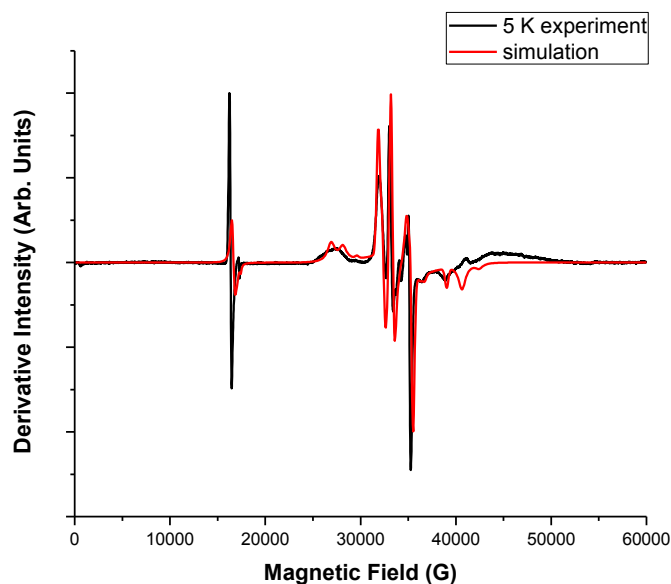
Figure V.15: 5 K W-band Experiment and $S = 1 + S = 2$ simulation of $[Et_2NH_2]_3[Cr_6F_{11}(O_2C^tBu)_{10}]\cdot\{C_6H_4\text{-}1,4\text{-}(OH)_2\}_2$ (**25**).

160

V.2.4 Inelastic Neutron Scattering Measurements on [Et$_2$NH$_2$][Cr$_6$F$_7$(O$_2$C^{t}Bu)$_{10}$(acac)$_2$]

INS measurements were performed on **23**. Figure V.6 shows 6 Å incident neutron wavelength measurements on a polycrystalline non-deuterated sample of **23**. The broad peak at ~-0.2 meV to ~+0.2 meV has a non-magnetic origin and is due to the large incoherent scattering cross section of hydrogen. The sharp doublet at ~0.4 meV can be assigned to magnetic excitations, this feature is labeled in Figure V.16. These are cold transitions, the intensity of these transitions increases with decreasing temperature. They are most intense at 1.8 K, therefore they originate from the $S = 0$ ground state to a transition to the zero field split S = 1 excited state.
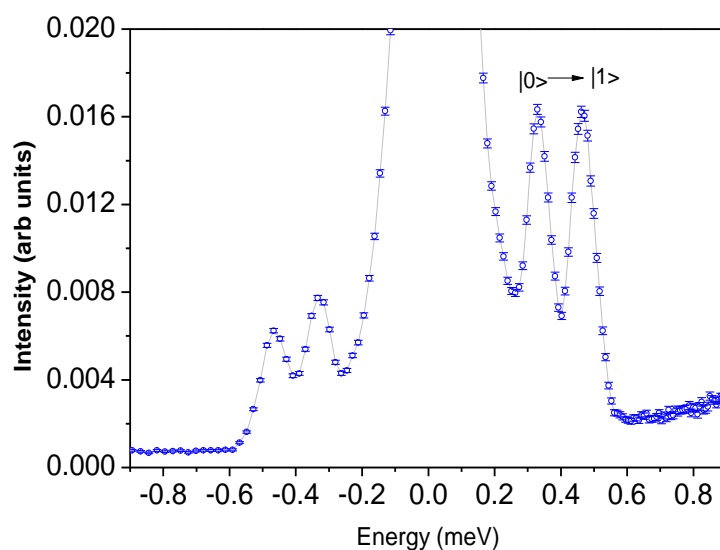
Figure V.16: INS spectrum of [Et$_2$NH$_2$][Cr$_6$F$_7$(O$_2$C^{t}Bu)$_{10}$(acac)$_2$] (**23**). Obtained with an incident wavelength of 6 Å at 6 K.

Figure V.17 shows INS which was measured at 15 K using an incident wavelength of 6.5 Å. These measurements also show a transition from the S = 0 ground state to the S = 1 excited state of **23**.
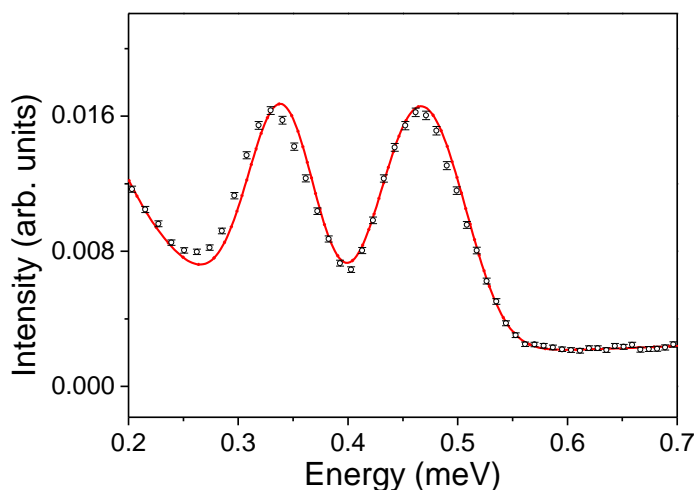
Figure V.17: .S = 1 INS doublet of $[Et_2NH_2][Cr_6F_7(O_2C^tBu)_{10}(acac)_2]$ (**23**). Obtained with an incident wavelength of 6.5 Å at 15 K.

The S = 1 transition is split into a doublet by zero field splitting. As the INS experiment has been done at zero magnetic field. The zero field splitting of the S = 1 spin state can be directly read from the INS spectrum. There is a gap of 1.07 cm^{-1} between the peaks of the doublet. The broadening of the higher energy resonance is due to a rhombic splitting of the m_s states and confirms a negative D value. This is in agreement with the EPR measurements. The following microscopic Hamiltonian has been used to fit the INS data:

$$\hat{H} = -J_a(\hat{S}_1\hat{S}_2 + \hat{S}_5\hat{S}_6) - J_b(\hat{S}_2\hat{S}_3 + \hat{S}_3\hat{S}_4 + \hat{S}_4\hat{S}_5)$$

$$+D_{Cr}\sum_i\left(S_{i,z}^2 - \frac{1}{3}S_i(S_i+1)\right) + E_{Cr}\sum_i(S_{i,x}^2 - S_{i,y}^2)$$

Equation V.2

The first two terms describe the isotropic exchange between nearest neighbouring Cr^{3+} atoms, where J_a and J_b are exchange coupling constants. The definition of J_a and J_b is given in Figure V.18 Different exchange interactions are needed for the terminal Cr^{3+} atoms and their nearest neighbour. The third term is the axial ZFS of each Cr^{3+} ion, where D_{Cr} is the single ion axial ZFS parameters. The fourth term describes the rhombic ZFS anisotropy, where E_{Cr} is the single ion rhombic ZFS parameter.
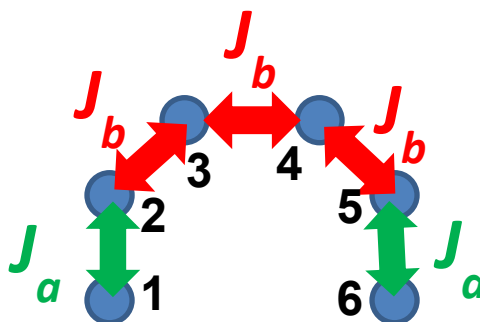
Figure V.18: Coupling Scheme used to model the INS data of **23**.

Figure V.19 shows experimental data recorded with an incident wavelength of 3.2 Å at 2 K (blue) and 15 K (red) and simulation (solid lines). The energy level diagram in Figure V.20 shows the origin of the transitions in the INS. The energy level diagram is colour coded and the transition in the INS spectrum are asterisked
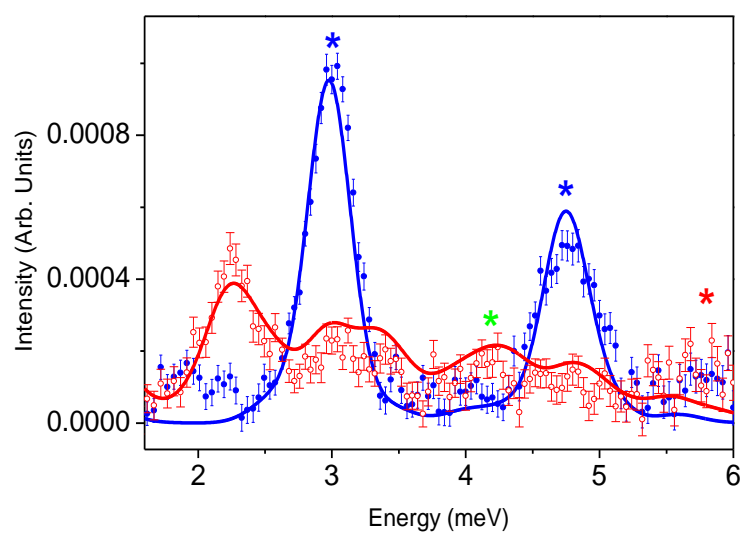
Figure V.19: INS experimental data and simulation of $[Et_2NH_2][Cr_6F_7(O_2C^tBu)_{10}(acac)_2]$ (**24**).
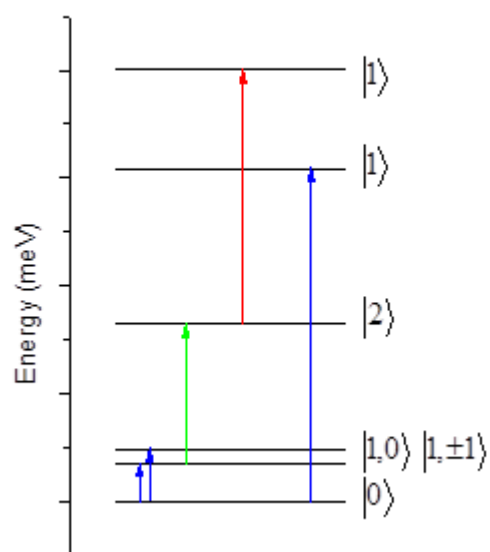
Figure. V.20: Energy level diagram of **24**, the energy levels are obtained by observing the temperature dependence and energy of the INS transitions.

The following parameters have been used in the simulation: J_a = - 11.4 cm^{-1}, J_b = 11.8 cm^{-1}, D_{Cr} = -0.045 cm^{-1} and E_{Cr} = 0.007 cm^{-1}. A good fit of the experimental data has been achieved.

V.2.5   Comparison of [Et$_2$NH$_2$][Cr$_6$F$_7$(O$_2$C^{t}Bu)$_{10}$(acac)$_2$] to Other Wheels and Horseshoes.

Table V.2 compares J-values and single ion ZFS tensors of selected homometallic Cr^{3+} clusters. The same D_{Cr} and E_{Cr} have been used to fit the INS data of **24** and **25**. The J_b exchange term is for the neighboring Cr^{3+} atoms in the body of the horseshoe. J_a relates to the exchange between terminal Cr^{3+} atoms and the adjacent Cr^{3+} atom. J_b is the same for all horseshoes and **1**. Different J_a-values are required for **22**, **23** and **24**. The nature of the β-diketonate capping ligand has an effect on the exchange coupling between the terminal Cr^{3+} and its neighbouring Cr^{3+} atom.

Table V.2: Single ion ZFS tensors and J-values (cm^{-1}) of selected homometallic Cr^{3+} clusters. The spin Hamiltonian parameters for **22** come from reference[9], for **23** and **24** from reference[11] and **1** from reference[12]

	J_a-value	J_b-value	D_{Cr}	E_{Cr}
{Cr$_6$}$_2$ (**22**)	-8.8 cm^{-1}	-11.8 cm^{-1}	-0.23 cm^{-1}	0.041 cm^{-1}
{Cr$_6$}Hfa (**24**)	-12.0 cm^{-1}	-11.8 cm^{-1}	-0.36 cm^{-1}	0.057 cm^{-1}
{Cr$_6$}acac (**23**)	- 11.34 cm^{-1}	-11.8 cm^{-1}	-0.36 cm^{-1}	0.057 cm^{-1}
{Cr$_8$} ring (**20**)	-11.8 cm^{-1}	-11.8 cm^{-1}	-0.31 cm^{-1}	0.032 cm^{-1}

From the *J*-values which have been determined, a zero field energy level diagram can be calculated. An isotropic model has been used for simplicity. The 12 lowest lying spin state of compounds **1**, **22**, **23** and **24** are shown in Figure V.21.
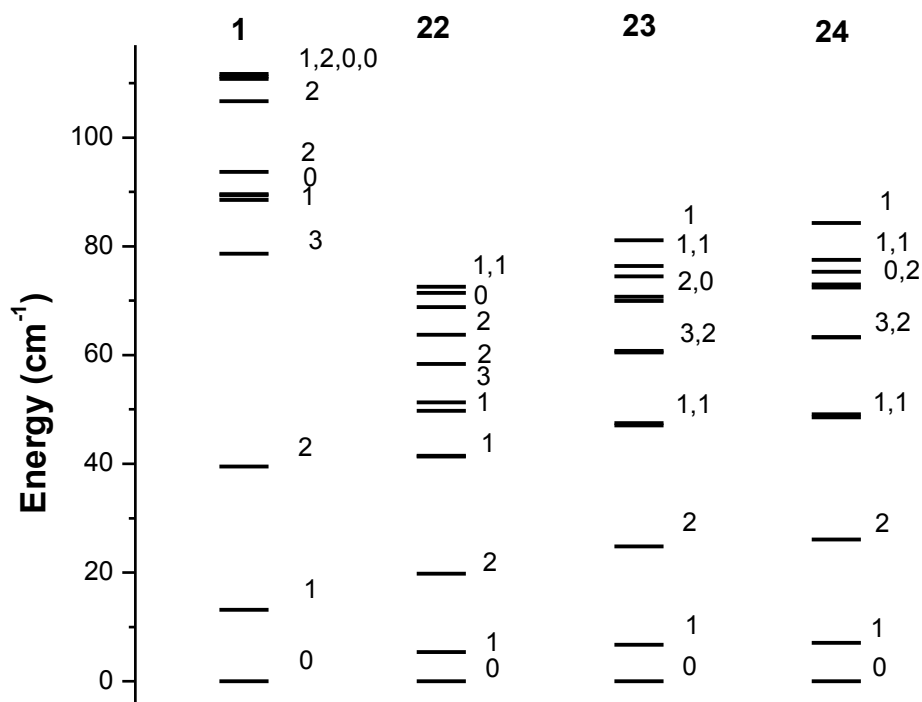
Figure V.21: An zero field energy level diagram of the 12 lowest lying total spin states of compounds **1**,**22**, **23** and **24**. The parameters used to calculate the energy levels are given in *Table* V.2 This energy level diagram was calculated using "MAGPACK".

From this energy level diagram we can see there are significant differences in electronic structure across the series. For compound **23** there is a gap of 6.7 cm^{-1} between the ground state and the first excited state. This is smaller than the ground state-excited state gap of **24**, which is 7.06 cm^{-1}. Hence, having a acac capping ligand instead of a Hfa has reduced the gap between the ground state and the first excited

state. The gap is smaller still for **22**, at 5.3 cm^{-1}. Therefore when the horseshoes are arranged in dimers, there is a smaller gap between the ground state and the first excited state. The capping ligand in both cases has increased the gap between the ground state and the first excited state. Compound **1** has the largest gap in the series between the ground state and the first excited state, at 13.2 cm^{-1}. Therefore, a wheel formation has the effect of increasing the gap between the ground state and the first excited state.

V.3 Conclusions

- Alkoxide bridging ligands in **21** provide a better pathway for magnetic superexchange, this is reflected in the ~49 % increase in J-values of **21** in comparison to **1**.

- Compound **21** has a smaller D tensor than **1,** D = 1.215 cm^{-1} for **21** and D = 1.68 cm^{-1} for **1**. This is due to crystal field effects, which have been explained in the discussion. A similar trend has been determined in the purple-Cr$_7$M wheels discussed in Chapter III.

- The ZFS tensor of **21** is more rhombic than **1**. This is due to a greater number of different coordination environments in **21**. This has also been observed in purple-Cr$_7$M wheels.

- The first two excited states (S = 1 and S = 2) of **25** and **22** can be modelled with identical spin Hamiltonian parameters. The polymeric nature of **25** does not affect its electronic structure.

- The J_a-value of the single horseshoe is different when different β-diketonate ligands are used. The choice of capping ligand has been found to affect the electronic structure of the single horseshoes.

- The J_a-value of the horseshoe dimer **22** is smaller than the analogues term in the single horseshoes **24** and **25**. The J-values have been used to calculate an zero field energy

level diagram; a dimeric horseshoe has been found to have a larger ground state to excited state gap than the two single horseshoes

- The electronic structure of **1** is different to both the single horseshoes and the horseshoes dimer. There is a much larger gap between the ground state and the first excited state.

- The D value of the $S = 1$ excited state of **21** and **23**, has been determined by both INS and EPR. INS is a useful technique to determine the zero field splitting of a spin state.

V.4 Reference

1. N. V. Gerbeleu, Y. T. Struchkov, G. A. Timko, A. S. Batsanov, K. M. Indrichan and G. A. Popovich, *Doklady Akademii Nauk SSSR*, 1990, **313**, 1459-1462.

2. J. van Slageren, R. Sessoli, D. Gatteschi, A. A. Smith, M. Helliwell, R. E. P. Winpenny, A. Cornia, A.-L. Barra, A. G. M. Jansen, E. Rentschler and G. A. Timco, *Chem. Eur. J.*, 2002, **8**, 277-285.

3. G. A. Timco, *unpublished results.*

4. M. L. Baker, *unpublished results.*

5. S.-M. Peng, C.-C. Wang, Y.-L. Jang, Y.-H. Chen, F.-Y. Li, C.-Y. Mou and M.-K. Leung, *J. Magn. Magn. Mater.*, 2000, **209**, 80-83.

6. W.-Z. Wang, R. H. Ismayilov, G.-H. Lee, I. P.-C. Liu, C.-Y. Yeh and S.-M. Peng, *Dalton Trans*, 2007, 830-839.

7. R. H. Ismayilov, W.-Z. Wang, R.-R. Wang, C.-Y. Yeh, G.-H. Lee and S.-M. Peng, *Chem. Commun.*, 2007, 1121-1123.

8. F. K. Larsen, J. Overgaard, S. Parsons, E. Rentschler, A. A. Smith, G. A. Timco and R. E. P. Winpenny, *Angew. Chem. Int. Ed.*, 2003, **42**, 5978-5981.

9. S. T. Ochsenbein, F. Tuna, M. Rancan, R. S. G. Davies, C. A. Muryn, O. Waldmann, R. Bircher, A. Sieber, G. Carver, H. Mutka, F. Fernandez-Alonso, A. Podlesnyak, L. A. Engelhardt, G. A. Timco, H. Güdel and R. E. P. Winpenny, *Chem. Eur. J.*, 2008, **14**, 5144-5158.

10. F. Tuna, *unpublished results.*

11. M. L. Baker, A. Bianchi, S. Carretta, D. Collison, R. J. Docherty, E. J. L. McInnes, A. McRobbie, C. A. Muryn, H. Mutka, S. Piligkos, M. Rancan, P. Santini, G. A. Timco, P. L. W. Tregenna-Piggott, F. Tuna, H. U. Guedel and R. E. P. Winpenny, *Dalton Trans.*, **40**, 2725-2734.

12. S. Carretta, J. van Slageren, T. Guidi, E. Liviotti, C. Mondelli, D. Rovai, A. Cornia, A. L. Dearden, F. Carsughi, M. Affronte, C. D. Frost, R. E. P. Winpenny, D. Gatteschi, G. Amoretti and R. Caciuffo, *Phys. Rev. B.*, 2003, **67**, 094405.

VI Experimental Methods

VI.1 Synthesis

Compounds **2-4** were synthesized by Dr. G. A. Timco of The University of Manchester and were published in reference[1]. The rotaxane templated wheels (**5-7**) which were discussed in Chapter II were also synthesized by Dr. G. A. Timco and were published in reference[2] The linked purple-Cr_7Ni dimers (**15-20**) which were discussed in chapter IV were synthesized by Mr. T. B. Faust of The University of Manchester.[3] Compound **25** was synthesized by Dr. G. A. Timco,[4] **24** was synthesized by Dr. Marzio Rancan of The Univeristy of Manchester and is published in reference[5] and **23** was synthesized by the author, was published in reference[6]. The author is very grateful for these contributions. The synthetic details are given below.

All reagents were purchased from Aldrich and were used as received.

Synthesis of Compounds **15**, **16**, **18** and **19**

11 (650 mg, 0.293 mmol) was refluxed in a 1:2.5 molar ratio with the appropriate ligand in acetone (50 mL) for 1 h. The reaction mixture was left to cool to RT and a crystalline product was formed. The solution was then left for 12 h, after which time the product was filtered off and was washed in acetone, until the washing were colourless. **15** (460 mg, 0.100 mmol, 89.3%), microanalysis for ($C_{176}H_{306}N_6O_{70}F_6Cr_{14}Ni_2$), calcd: C, 46.09; H, 6.73; N, 1.83; Cr, 15.87; Ni, 2.56%, found: C, 45.74; H, 6.47; N, 1.78; Cr, 15.94; Ni, 2.52%. A crystallographic data file (cif) can be found on the CD provided with this thesis it is labeled 15.cif. **16** (320 mg, 0.070 mmol, 62.5%), microanalysis for ($C_{178}H_{306}N_4O_{70}F_6Cr_{14}Ni_2$) calcd: C, 46.66; H, 6.73; N, 1.22; Cr, 15.89; Ni, 2.56%, found: C, 46.40; H, 7.02; N, 1.13; Cr, 15.90; Ni, 2.47%. A cif file can be found on the CD provided with this thesis it is labeled 16.cif. **18** (490 mg, 0.107 mmol, 95.5%),

microanalysis for ($C_{178}H_{310}N_4O_{70}F_6Cr_{14}Ni_2$), calcd: C, 46.62; H, 6.81; N, 1.22; Cr, 15.87; Ni, 2.55%, found: C, 46.43; H, 7.05; N, 1.08; Cr, 15.69; Ni, 2.46%. A cif file can be found on the CD provided with this thesis it is labeled 18.cif. **19** (334 mg, 0.072 mmol, 64.6%), microanalysis for ($C_{178}H_{310}N_4O_{72}F_6Cr_{14}Ni_2$), calcd: C, 46.30; H, 6.77; N, 1.21; Cr, 15.76; Ni, 2.54%, found: C, 45.72; H, 6.91; N, 1.18; Cr, 15.83; Ni, 2.45%. A cif file can be found on the CD provided with this thesis it is labeled 19.cif.

Synthesis of Compound **23**

Synthesis of **23**: 3.00 g (0.85 mmol) of **22** and 3.4 g (3.4 mmol) of Hacac were dissolved in toluene (200 ml) producing a deep green solution. This solution was stirred and refluxed for 24 h at 130 ^{o}C. After this time the solution was left to cool to RT. The solvent was removed and the product was purified by column chromomatography using THF/*n*-hexane (1:2) (with increasing proportions of THF). The product was the third fraction. The product was crystallized from acetone/acetonitrile, affording X-ray quality crystals; yield 1.1g (37.4 %). Elemental analysis: (calculated (%) for $C_{64}H_{116}Cr_6F_7N_1O_{24}$) : Cr 18.20. C 44.47, H 6.76, N 0.81; found Cr 17.90, C 44.63, H 6.95, N 0.85. ES MS (sample dissolved in THF/MeOH, run in MeOH): m/z: - 1654 [M – (Et_2NH_2)]⁻, 1802 [M + (Et_2NH_2)]⁺

Synthesis of Compound **25**

To a solution of [(Et_2NH_2)$_3Cr_6F_{11}(O_2C^tBu)_{10}$]$_2$ (1.2 g, 0.342 mmol) dissolved in Et_2O (55 mL) and THF (25 mL), hydroquinone (300 mg, 2.725 mmol) was added and stirred for

15 min at RT. A green microcrystalline product started to form during this time, which was collected by filtration 24 h later. The product was washed with Et2O, and then extracted with THF (100 mL). The product was then filtered off and dissolved in MeCN (10 mL). Slow evaporation of the solution yielded a crystalline product. Yield 1.15 g. A cif file can be found on the CD provided with this thesis, it is labeled 25.cif

VI.2 X-ray Crystallography

All crystal structures have been published previously in the same references which provide the synthetic details, crystallographic information files (cif files) have been provided on the CD which accompanies this Ph.D. thesis

VI.3 Magnetic Measurements

The super conducting quantum interference device (SQUID) magnetometry measurements were performed on a Quantum Design MPMS-XL SQUID magnetometer, which was equipped with a 7 Tesla magnet. The samples were polycrystalline and were fixed in eicosaine to prevent the sample from orientating in the field. The diamagnetic susceptibility of the molecule was estimated using Pascal's constants and was subtracted from the experimental data. The diamagnetism of the sample holder and of the eicosaine was also subtracted from the experimental data.

The SQUID magnetometry calculations were performed using the isotropic version of Magnetic Properties Analysis Package for Spin Clusters (MAGPACK).[7]

VI.4 EPR Measurements

The Q- and K-band EPR spectra were recorded on a Bruker Elexsys Spectrometer, which uses a 2 T Bruker electro magnet and a Oxford Instruments helium cryostat. The S- and X-band spectra were recorded on a Bruker EMX system, which uses a 1.5 T Varian electro magnet and an Oxford Instruments helium cryostat. The W-band EPR spectra were recorded on a Bruker Elexys Spectrometer which was equipped with a helium cryostat and a 6 T superconducting magnet. Baseline corrections were applied to the spectra when necessary and were done in a manner not to distort the spectral features. Polycrystalline samples were measured. The samples were lightly powdered. When required the samples were immobilized in eicosaine, this was to prevent the sample orientating in the strong magnetic fields which were applied to the sample. This is not required at lower frequencies such as S-band. In order to record accurate g-values, the magnetic field was field corrected using a radical for which the g-value is accurately known. The organic radical 2,2-diphenyl-1-picrylhydrazyl (g = 2.0037 ± 0.0002) was used.[8] A unknown g-value can be obtained with *Equation* VI.1.

$$g_x - g_{Std} = \frac{H_x - H_{Std}}{H_{Std}} g_{Std}$$

Equation VI.1

The EPR spectra were modelled using Weihe's EPRSIM program.[9] The program works by generating an energy matrix for each orientation of the molecule relative to the magnetic field. The resonance of each transition is determined by successive

diagonalizations and iterations. The relative intensity is calculated from the eigenvectors. The transitions are summated over the whole space, and each transition is represented by a Gaussian curve produces the simulated spectra.

The simulated spectra are compared by eye to the experimental spectra, the spin-Hamiltonian parameters are then varied until a good fit of the experimental spectrum is achieved.

VI.5 Inelastic Neutron Scattering Measurements

Inelastic neutron scattering measurements discussed in chapter V were performed in IN5b time of flight inelastic spectrometer[10] at Institute Laue-Langevin, Grenoble, France. These measurements were performed in collaboration with Dr. M. L. Baker. A non deuterated, polycrystalline sample of **23** was put in a hollow aluminium cylinder and was measured.

VI.6 Reference

1.   G. A. Timco, E. J. L. McInnes, R. J. Pritchard, F. Tuna and R. E. P. Winpenny, *Angew. Chem. Int. Ed.*, 2008, **47**, 9681-9684.

2.   B. Ballesteros, T. B. Faust, C.-F. Lee, D. A. Leigh, C. A. Muryn, R. G. Pritchard, D. Schultz, S. J. Teat, G. A. Timco and R. E. P. Winpenny, *J. Am. Chem. Soc.*, **132**, 15435-15444.

3.   T. B. Faust, V. Bellini, A. Candini, S. Carretta, L. Carthy, B. J. Coe, D. Collison, R. J. Docherty, J. Kenyon, L. Giulia, J. Machin, E. J. L. McInnes, C. Muryn, R. J. Pritchard, S. J. Teat, G. A. Timco, F. Tuna, G. F. Whitehead, W. Wernsdorfer, M. Affronte and R. E. P. Winpenny, *Chem. Eur. J.*, 2011, **Submitted**.

4.   G. A. Timco, unpublished result.

5.   M. Rancan, G. N. Newton, C. A. Muryn, R. G. Pritchard, G. A. Timco, L. Cronin and R. E. P. Winpenny, *Chem. Commun.*, 2008, 1560-1562.

6.   M. L. Baker, A. Bianchi, S. Carretta, D. Collison, R. J. Docherty, E. J. L. McInnes, A. McRobbie, C. A. Muryn, H. Mutka, S. Piligkos, M. Rancan, P. Santini, G. A. Timco, P. L. W. Tregenna-Piggott, F. Tuna, H. U. Guedel and R. E. P. Winpenny, *Dalton Trans*, 2011, **40**, 2725-2734.

7.   J. J. Borrás-Almenar, J. M. Clemente-Juan, E. Coronado and B. S. Tsukerblat, *J. Comput. Chem.*, 2001, **22**, 985-991.

8.   J. A. Weil, J. R. Bolton and W. J. E., *Electron Paramagnetic Resonance: Elementary Theory and Practical Applications*, John Wiley & Sons, Inc, New York, 1994.

9.   J. Glerup and H. Weihe, *Acta Chem. Scand.*, 1991, **45**, 444-448.

10.   J. Ollivier, M. Plazanet, H. Schober and J. C. Cook, *Physica B*, 2004, **350**, 173-177.

VII Concluding Remarks and Future Work

A spectroscopic study has been carried out on two types of green-Cr_7M wheels; rotaxane-Cr_7M wheels and caesium-templated Cr_7M wheels.

- It has been found that when the wheels are templated with a long dialkylammonium group, the spectroscopic properties of the wheel are the same as the dimethylammonium templated wheels. Both of these families have very similar MPLN values, therefore the wheels have very similar geometries and we should not expect any significant change in electronic structure.

- It has been found that the caesium templated wheel are spectroscopically different There is a ~20 % decrease in the ground state D values of **9** and **10** in comparison to the dialkylammonium templated wheels. The ground state g-values of **8** are more isotropic than the g-values of the Cr_7Ni dialkylammonium templated wheels. The differences in spectroscopic parameters, originate from the differences in MPLN values.

- Magnetic measurements could be carried out in the future to determine if the caesium templated wheels have different J_{CrCr}-values in comparison to dialkylammonium-templated wheels.

- Future work could include templating the formation of a Cr_7M wheel around a rubidium ion and conducting an EPR study to see if the spectroscopic properties are altered in the same manner as the caesium templated wheels.

The spin-Hamiltonian parameters of a family of purple-Cr_7M wheels have been determined.

- Magnetic measurements and EPR have confirmed that the purple-Cr_7M wheels have the same ground spin state as the green wheels. Hence equivalent coupling schemes can be used for both families. The reduced

symmetry of a purple-Cr_7M has not disrupted the exchange coupling between neighbouring metal ions.

- Magnetic measurements have confirmed that the purple-Cr_7M wheels have 35 % larger J_{CrCr}-values (from 5.90 cm^{-1} to 8.00 cm^{-1}) than the green-Cr_7M wheels. This must mean that there is a better exchange pathway *via* bridging alkoxide groups compared to bridging fluoride ions. The purple-Cr_7M wheels have a larger ground state to excited state gap than Cr_7M wheels which are templated around a dialkylammonium group.

- The purple-Cr_7M wheels have smaller *D*-values than the green wheel family; this is due to crystal field effects. The ground state of the purple wheel family also has larger λ values; this is due to the purple wheels being less symmetrical.

- The purple wheel family has narrower EPR line widths than the green wheel family; this is partly due to the larger ground state- to excited state energy gap. The narrower line widths can also be attributed to a reduction in the number of bridging $^{19}F^-$ ions, which may be a source of unresolved hyperfine interactions. It is likely that the purple-Cr_7M family will have longer spin decoherence times. Pulsed EPR studies are currently being carried out to determine if this is correct.

EPR spectroscopy has been used to study the interaction between linked dimers of purple-Cr_7Ni wheels.

- Single purple-Cr_7M wheels have been linked chemically as well as electronically. For compounds **15** to **18** there is clearly a spin triplet EPR spectrum below 10 K. For compounds **19** and **20** the spectrum is not well resolved, however the EPR spectra of these compounds is distinctly broader

than that of a single purple-(Cr_7Ni). This confirms that there is electronic communication between the wheels.

- A relationship between D and the organic linker has been established. D is smaller for the saturated linkers. There is more efficient communication through an unsaturated linker. This means that there is more efficient magnetic superexchange through a fully conjugated π-system.

- The shorter unsaturated linkers (when calculated through bond) exhibit a larger value of D. This is an intuitive result, as you would expect there to be more efficient electronic communication between the two wheels *via* a shorter organic linker.

- Future work will include introducing switch-ability of the interaction within a purple-Cr_7Ni dimer. This could possibly be done by the use of redox or photo-active linking molecules. This would be an essential feature to implement the design of a two-qubit gate.

A family of homometallic Cr^{3+} cluster have been studied.

- The alkoxide bridging ligands of **21**, provide a better pathway for magnetic superexchange, there is a 49 % increase in J-values of **21** in comparison to **1**. **21** also has a smaller D-value and larger λ than **1**. This is what has also been determined for the purple-Cr_7M wheels in Chapter III, the same explanation can be used.

- The choice of β-diketonate capping ligand can be used to alter the electronic structure of a single horseshoe. **24** has a larger gap between the ground state and the excited state than **23**. Having an acac capping ligand instead of Hfa reduces the gap between the ground state and excited state and has the effect

of reducing the exchange interaction between the terminal Cr^{3+} ion and its nearest neighbour.

- Future work could include investigating the effect of other β-diketonate capping ligands on spectroscopic properties of hexanuclear Cr^{3+} horseshoes.

VIII Appendix

VIII.1   Appendix: Definition of the single ion projection coefficient (c_i) of the hyperfine splitting tensor for an exchanged coupled dinuclear system AB

Adapted from reference[1]

For a dinuclear systems the total spin is defined as:

$$\hat{S} = \hat{S}_A + \hat{S}_B$$

There are the following relationships between the Hyperfine splitting tensors, g tensors and ZFS tensors of the coupled pair and the individual metal centres:

$$A_s^k = c_1 A_1^K + c_2 A_2^k$$

$$g_s = c_1 g_1 + c_2 g_2$$

$$D_S = d_1 D_1 + d_2 D_2 + d_{12} D_{12}$$

Where

$$c_1 = \frac{(1+c)}{2}, \quad c_2 = \frac{(1-c)}{2}$$

$$d_1 = \frac{(c_+ + c_-)}{2}, \quad d_2 = \frac{(c_+ - c_-)}{2}$$

and

$$c = \frac{S_A(S_A+1) - S_B(S_B+1)}{S(S+1)}$$

$$c_+ = \frac{3\left[S_1(S_1+1) - S_2(S_2+1)\right]^2 + S(S+1)\left[3S(S+1) - 3 - 2S_1(S_1+1) - 2S_2(S_2+1)\right]}{(2S+3)(2S-1)S(S+1)}$$

$$c_- = \frac{4S(S+1)\left[S_1(S_1+1) - S_2(S_2+1)\right] - 3\left[S_1(S_1+1) - S_2(S_2+1)\right]}{(2S+3)(2S-1)S(S+1)}$$

1. A. Bencini and D. Gatteschi, *EPR of Exchanged Coupled System*, Springer-Verlag, Berlin, 1989.

VIII.2 Appendix: Results of Single Crystal Study of [{Cr$_7$NiF$_3$(Etglu)(O$_2$C^{t}Bu)$_{15}$}$_2$(4,4'-bpy)] (15)

Road map of the resonances of **15** at Q-band Frequency 5 K, *bc* plane of a monoclinic crystal and molecular orientation with respect to applied magnetic field:
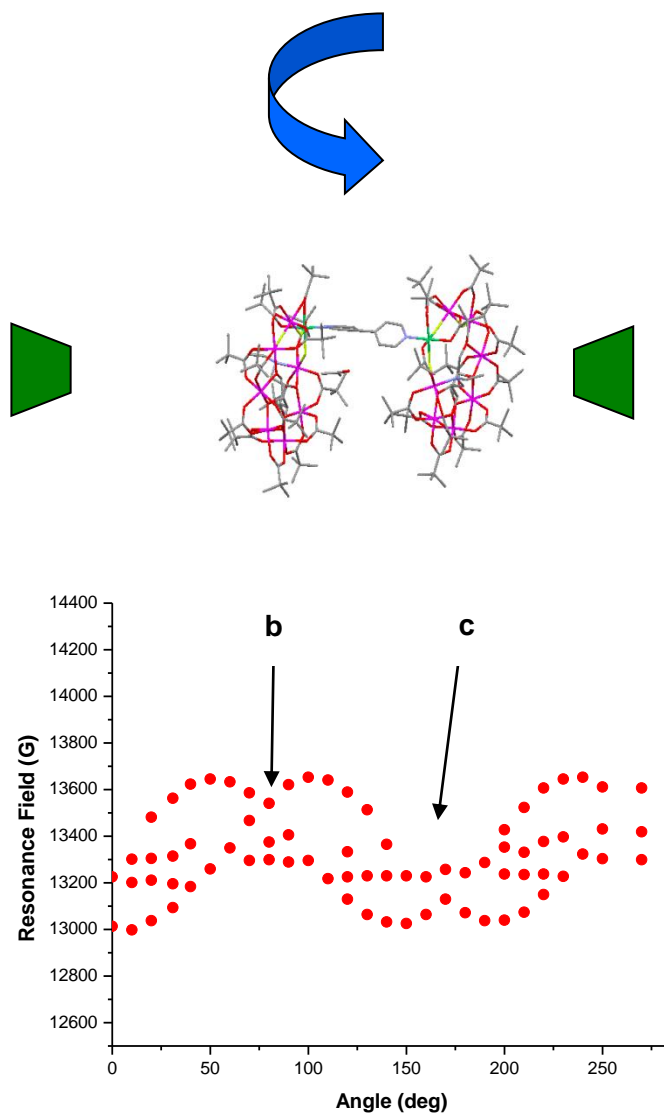
Road map of resonances of **15** at Q-band frequency, 5 K, *ac** plane of a monoclinic crystal and molecular orientation with respect to field:
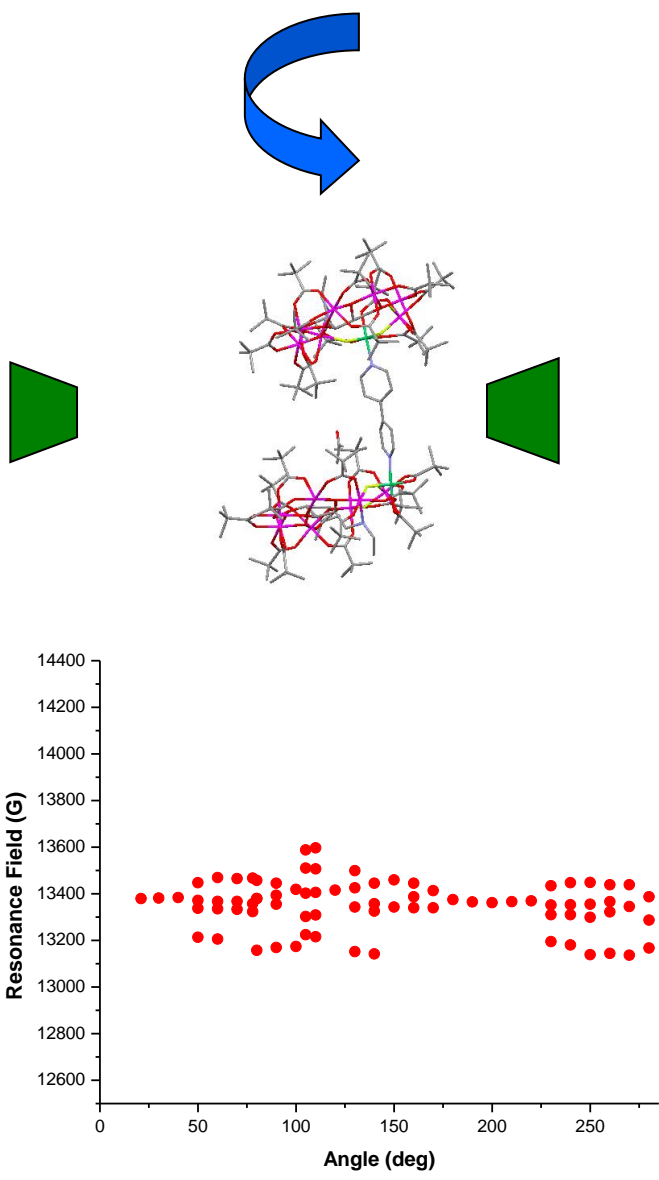
VIII.3   Appendix: Crystallographic Data of 23

Analysis after data collection showed that the crystal of **23** was twinned. The twins were reduced individually and were then combined to make a HKLF5 file.

Table VIII.4.1: Crystallographic data of 23

Empirical formula	$C_{66}H_{119}Cr_6F_7N_2O_{24}$
Formula weight	1769.63
Temperature	100(2) K
Crystal system	Triclinic
Space group	P -1
Unit cell dimensions	a = 11.8455(5) Å, α = 100.750(4)°
	b = 17.3967(9) Å, β = 98.088(4)
	c = 24.6928(11) Å, χ = 108.911(4)
Volume	4617.3(4) Å^3
Z	2
Density	1.226 g cm^{-1}
Shape and colour	green plate
Crystal size	0.8 x 0.4 x 0.1
μ	0.757 cm^{-1}
Unique data	32120
Absorption correction	Multi-scan
Transmission max/min	0.9281, 0.5825
Unique data (F$_0$>4σ.F$_0$)	23612
Parameter/retraints	1042/1919
R1, wR2[a]	0.0982, 0.2775
Weighting scheme[b](w^{-1})	$\sigma^2(F^2_0) + (0.0898 \, P)^2 + 84.9472P$
Goodness of fit	1.102
Largest residuals	+1.256 Å^{-3}, -1.239 Å^{-3}